University of Cincinnati

Date: 7/1/2015

I, Niranjala D Wickremasinghe , hereby submit this original work as part of the requirements for the degree of Doctor of Philosophy in Physics.

It is entitled:

Optical properties of organic films, multilayers and plasmonic metal-organic waveguides fabricated by organic molecular beam deposition

Student's name: **Niranjala D Wickremasinghe**

This work and its defense approved by:

Committee chair: Hans Peter Wagner, Ph.D.

Committee member: Young Kim, Ph.D.

Committee member: Brian Meadows, Ph.D.

Committee member: Rostislav Serota, Ph.D.

16257

Optical properties of organic films, multilayers and plasmonic metal-organic waveguides fabricated by organic molecular beam deposition

A dissertation submitted to the

Graduate School of the University of Cincinnati

in partial fulfilment of the

requirements for the degree of

Doctor of Philosophy

in the Department of Physics

of the Collage of Arts and Science

2015

by

Niranjala D. Wickremasinghe

B. Sc., University of Peradeniya, Sri Lanka, 2003

M.Sc., University of Cincinnati, 2011

Committee Chair: Professor Hans-Peter Wagner

Abstract

In this thesis, the optical properties of tris (8-hydroxyquinoline) aluminum (Alq_3) and 3,5,9,10-perylentetracarboxylic dianhydride (PTCDA) organic films, PTCDA/ Alq_3 multilayers and plasmonic Alq_3-metal waveguides are investigated. The organic films and heterostructures used for this work were fabricated by organic molecular beam deposition (OMBD).

We investigated the quenching of the light emission in Alq_3 films grown on a Si substrate as a function of cw laser excitation intensity at varying temperatures from 15 to 300 K. The saturation of the singlet-singlet annihilation coefficient was measured with spectrally-integrated (SI) photoluminescence (PL) using a photodiode. The bimolecular quenching coefficient was further studied with time-resolved (TR) PL as a function of 100 fs pulse fluences. The PL quenching is attributed to the annihilation of trapped excitons at Alq_3 nanocrystal grain boundaries. The saturation is explained by the limited density of available trapping states at the grain boundaries. Our interpretation is supported by structural investigations of ultrathin Alq_3 films with atomic force microscopy (AFM), scanning electron microscopy (SEM) and by comparing the experimental data with calculations using a coupled rate equation model.

The wavelength dispersion of the refractive indices of PTCDA and Alq_3 layers and of PTCDA/Alq_3 multilayer waveguides grown on Pyrex substrates was investigated. The *m*-line technique, an evanescent prism coupling technique, was used to determine the layers' thickness and the in-plane (TE modes) and normal (TM modes) refractive indices. The

potential for controlling the refractive index dispersion and anisotropy by tailored organic multilayer waveguides is discussed.

In addition, the mode properties of planar dielectric Alq_3 multilayer waveguides comprising one single or three embedded nanometer-thin Alq_3-$Mg_{0.9}$:$Ag_{0.1}$ composite metal-island layers were investigated. The TE and TM modes were selectively excited at the wavelength of 633 nm using the *m*-line method. Selective excitation of plasmonic TM modes and or dielectric TM modes as well as the possibility of suppressing guided TE modes using strategically placed metal layers is presented. The prospect to design mode selective waveguides and TM-TE mode couplers is discussed.

Finally, the two-photon absorption and nonlinear refraction in PTCDA and in Alq_3 films were investigated using z-scans with tightly focused (with a 10x or a 20x microscope objective lens) 100 fs laser pulses at reduced repetition rates at the wavelength of 820 nm. To study the influence of sample heating, the pulse repetition time was varied between 0.75 and 20 μs with an acousto-optic pulse selector. The thermal effect was diminished for pulse repetition times longer than 5 and 0.75 μs in PTCDA film using a 10x or 20x microscope lens, respectively, resulting in a TPA coefficient of 6 cm/GW and a nonlinear refractive index of 1.2×10^{-13} cm^2/W. In the Alq_3 film, even at shorter repetition times (1.25 - 5.0 μs) no noticeable heat accumulation with the 10x lens has been observed. TPA coefficient of 0.11 cm/GW and nonlinear refractive index of 2.1×10^{-14} cm^2/W were determined in the Alq_3 film.

Acknowledgements

I would like to express my deepest appreciation and thanks to my advisor Prof. Hans-Peter Wagner for his wonderful mentoring throughout the course of this dissertation research. His professionalism, active supervision, kind assistance and carefulness have greatly influenced my achievements during many challenges and for the successful completion of all four research projects which resulted in several peer reviewed publications. His advice and timely comments on research as well as on scientific writing were invaluable. I greatly acknowledge his patience with my mistakes in both the research and writing. I would like to thank him for giving me the opportunity join Micro & Nano Photonics group and work on organic semiconductor films which allowed me to get experience in diverse experimental skills and techniques. I am grateful to Professor Wagner for everything he provided me on my way to this successful completion.

I would also like to thank my committee members Professor Rostislav Serota, Professor Brian Meadows and Professor Young Kim for serving as my committee members and for your comments and suggestions during the course of thesis. I am sincerely grateful to Professor Heidrun Schmitzer at Xavier University, Cincinnati, for her assistance in profilometer measurements, for valuable discussions, comments and the assistance in analysis of multilayer and plasmonic waveguide data. I would like to extend my gratitude to Professor

Warren Huff at the Department of Geology for performing X-ray diffraction measurements and to Dr. Melodie Fickenscher at ERC for performing scanning electron microscopy (SEM) measurements and training me on atomic force microscopy (AFM).

I express my warm thanks to Dr. Xiaosheng Wang, from whom I learnt all the experimental skills and techniques as a fresh graduate student while you were a post-doctoral scholar in Professor Wagner's research group. As a junior member, his expertise in the field and his friendly attitudes inspired me to hang around and work with him when he was doing measurements. His willingness to transfer all his experience and expertise to me and my desire to absorb laid a concrete basis for me to become an expert in organic molecular beam deposition (OMBD), m-line technique, z-scan technique and in time resolved photoluminescence (TR PL) measurements within a short time period. This allowed me to involve in my own research projects confidently and comfortably in a short period of time. I greatly appreciate his productive friendly discussions and sharing his experience and expertise with me.

I would like to express my special thanks to John Markus, for sharing his expertise on instrumentation, and for his invaluable support on maintaining, troubleshooting instruments which were important assets for the successful completion of my thesis. I would like to thank all faculty and staff members of the Department of Physics who helped me in numerous ways. My gratitude also goes to senior lab colleagues Dr. Amit Dongol, Dr. Milhan Ajward and juniors Jonathan Thompson, Fateme Mohammadi and specially to Masoud Kaveh, for their kind help in my experiments and spending their time and sharing expertise with me. I am also thankful to my friends in Cincinnati, who helped me a lot in many ways.

Last but not least, I want to thank my parent for their continuous support in achieving my goals. I cannot express in words how grateful I am to my mother and father for all the sacrifices and commitments that they have made for me. The support they given us during thier short stay with us in Cincinnati was priceless. I am indebted for them forever for all what they have done for me. I am grateful to my sister for giving me an emotional support during my thesis work. Our lovely Tharusha and Minuka, your love, your cute smiles have always been emotional blessings for me and I love you so much. My deepest appreciation for my beloved husband Athula for all his incomparable support, love, encouragement and commitments he has done for me. Your dreams, your hopes, your wishes reflected on me and kept me going this much far. My heartfelt thank to you Athula!

Contents

List of Figures

List of Tables

Chapter 1 Introduction

Organic materials can be fabricated as high quality heterostructures without lattice matching[1,2], which is a crucial factor for high performance devices. In addition, organic materials can be deposited on a variety of substrates including low-cost and flexible substrates and also on any other organic [3,4], inorganic or on metal layers [5,6]. Many organic semiconductors have shown reasonable charge carrier transport properties as well as high luminescence efficiency. Hence, in the past decade, there has been a significant interest to use organic semiconductors for organic light emitting diodes (OLEDs) [7–9], as white OLEDs (WOLEDs) [10–12], in photovoltaics [13,14], as photodetectors[15] and recently also for organic spin valve systems [16–18]. Such OLEDs are now commercially available in light-weight colour flat panel displays [19,20] in TV screens, mobile phones, laptops as well as in several other modern electronic devices. OLEDs provide brighter displays while consuming low power compared to light emitting diodes (LEDs) and liquid crystal displays (LCDs), which are currently in use.

The metal chelate tris (8-hydroxy) quinoline aluminum (aluminum quinoline, Alq_3) is a commonly used electron transport and photon emitting layer in OLEDs. Various types of device structures and carrier transport films were introduced [21–24] in need of enhancing the light out-coupling of organic light emitting diodes. Recently, Alq_3/ZnO hybrid composite films were used in Alq_3 based OLEDs in order to enhance the environmental stability and emission yield of

OLEDs [25]. Despite the vast investigations on Alq_3 based electronic devices the influence of ordered molecular aggregations [26,27] or nano-crystalline structures in quasi-amorphous Alq_3 films and their influence on the light emission is not yet fully understood. The quenching behaviour as a function of excitation intensity as well as of temperature was investigated using spectrally integrated and time integrated (TI) photoluminescence (PL) with a photodiode. The saturation of the bimolecular quenching coefficient was separately investigated using time-resolved (TR) PL as a function of excitation pulse fluence. The observed quenching behaviour is explained using a coupled rate equation model for steady state excitation. In this thesis we also structurally examined the morphology of ultra-thin (nominally 5-15 nm thick) Alq_3 films with atomic force microscopy (AFM) and scanning electron microscopy (SEM) and revealed the existence of ordered (nanocrystalline) areas on a several 10 nm length scale which further support our interpretation

The dielectric properties of organic multilayers made from different materials can be designed because the multilayer structure acts as an effective medium. An effective medium multilayer waveguide acts like a homogeneous and anisotropic dielectric slab which offers new opportunities to tailor waveguides and heterostructures with certain optical anisotropy and nonlinearity[28,29]. Aluminum quinoline has isotropic optical properties. 3,4,9,10-perylentetracarboxyl–dianhydride also known as PTCDA has strong anisotropic optical and electrical properties [3,4]. The combination of PTCDA and Alq_3 in multi-layered films can potentially be used to tune the birefringence and the refractive index dispersion of waveguide structures.

Increasing the integration density of optical elements in future photonic integrated circuits is problematic since the diffraction of light limits further miniaturization. Hybrid organic/metal nanostructures enable light compression through nanometer thick metal films by plasmon oscillations of a free-electron. Long-range guiding of surface plasmon-polaritons (SPPs) below the diffraction limit [30–32] with bending of light [33] or beam splitting using T or Y shaped junctions [34,35] are potential applications of the hybrid organic/metal plasmonic structures. In metal-air or metal-dielectric bilayers [31,36], dielectric-metal-dielectric (DMD) waveguides [30,37–39], metal-dielectric-metal (MDM) structures [40–44] as well as in dual slab waveguide structures [32,45], the guiding of modes and their properties have been investigated mainly theoretically. In this thesis the properties of guided modes (transverse magnetic (TM) and electric (TE) modes) in planar dielectric Alq_3 waveguides with single or three embedded few nanometer thin metallic films are both experimentally and theoretically investigated. Plasmonic Alq_3 multilayer waveguides were fabricated by organic molecular beam deposition (OMBD) and an alloy of Mg:Ag was used as the embedded metal layers.

Many of the organic materials possess high nonlinearities [46–49] and are promising materials for nonlinear optical applications including optical power limiting [49–52] and two-photon 3D data storage [53,54]. In particular, various perylene derivatives have shown high two photon absorption (TPA) cross sections [48,49]. Organic materials have an enormous potential to enhance the nonlinear response of photonic structures [55,56] owing to their large nonlinearities and the ability to use in composite and hybrid nanostructures. The z-scan technique, which is a very sensitive optical method that allows measuring both the TPA coefficient and the nonlinear refractive index [57,58] is commonly used to study the nonlinear optical properties of semiconductors [59,60], nanoparticles [61,62], hybrid structures [55,63,64] and organic materials [46–49,65].

Generally, the nonlinear signal is often modified by accumulated thermal effects [64,66–69] due to the high pulse repetition rate. In order to manage accumulated heating [66–68,70], different approaches have been reported which are not suitable for soft materials and materials with fast thermal build-up time [66–70]. In my thesis, a "tightly focus modified z-scan technique" is proposed which can be used with low fluence 100 fs laser pulses at reduced repetition rates to eliminate heat accumulation in thin solid films. Here, an acousto-optic modulator (AOM) was used as the pulse selector to reduce the repetition rate and the pulses are tightly focused to accelerate the thermal diffusion from the focus area to the unexcited film area. Using this modified z-scan technique the two photon absorption (TPA) coefficient, nonlinear refractive index and third order susceptibility of PTCDA and of Alq_3 thin films were determined at the excitation wavelength 820 nm with high repetition, femtosecond laser pulses.

1.1 Outline of the thesis

In my thesis, **Chapter 2** contains few important details of Alq_3 and PTCDA molecules, the OMBD technique and the deposition of organic and metal layers. In addition, the morphological characterization of OMBD grown thin films is illustrated.

In **Chapter 3**, quenching of the light emission in an aluminum quinoline (Alq_3) film as a function of excitation intensity at temperatures ranging from 15 to 300 K is investigated by time-resolved (TR) photoluminescence (PL) with a 100 fs pulse excitation and by spectrally and time integrated PL using a photodiode as a detector with cw laser excitation. The results are explained by efficient bimolecular quenching of excitons which are trapped at energy minima at the grain

boundaries in the polycrystalline Alq_3 film. Our interpretation is supported by calculations using a coupled rate equation model.

In the **Chapter 4** of my thesis, the wavelength dispersion of the refractive indices of PTCDA and Alq_3 layers as well as of PTCDA/Alq_3 organic multilayer waveguides is investigated. The waveguides were grown on Pyrex® substrates by OMBD. The *m*-line technique [71–73], a well-known evanescent prism coupling technique (described in Section 4.2), was used to determine the effective refractive indices of all observable modes in these waveguides. The *m*-line method allows determining the bulk in-plane (TE modes) and normal (TM modes) refractive index values of the waveguide material and the thickness of the waveguide.

The investigation of the mode properties of planar dielectric aluminum-quinoline (Alq_3) multilayer waveguides consist of one single or three equally spaced embedded nanometer-thin Alq_3-$Mg_{0.9}$:$Ag_{0.1}$ composite metal-island layers are presented in the **Chapter 5**. The *m*-line technique was used to selectively excited Transverse magnetic (TM) and transverse electric (TE) guided modes and to study the properties of guided modes. Experimentally observed guided modes were compared and explained by a multilayer model calculation and by simulated filed distributions in the plasmonic dielectric waveguide.

In the **Chapter 6**, accumulated thermal effect in the focus area and the influence of thermal effect on two photon absorption process was investigated systematically using the open aperture z-scan technique with high repetition rate femtosecond laser pulses on thin PTCDA and on Alq_3 films. A “modified tightly focused z-scan technique” is introduced which can be used to diminish the accumulated thermal effect at the focus area. The z-scan measured third order

nonlinear optical constants of PTCDA and of Alq_3 thin films at the excitation wavelength 820 nm with high repetition, ultrafast laser pulses are presented.

Finally, **Chapter 7** summarizes the results and achievements of this thesis.

Chapter 2 Organic materials, fabrication of thin films and morphological study of thin films

2.1 Introduction

Conjugated organic molecules are interesting materials due to their optical, electrical, structural and chemical properties. These π-conjugated small molecular organic materials have relatively weak van der Waals interactions between adjacent molecules. Due to the weak intermolecular aan der Waals interaction, these organic materials are more flexible and can be deposited on any substrates even on flexible substrates without lattice matching. Perylene derivatives and metal chelates are two groups of organic molecules which are rigorously investigated due to their broad range of potential applications. Many reported perylene derivatives show high optical nonlinearity and strong birefringence. Aluminum quinoline (Alq_3) is a renowned material in modern organic devices as OLEDs. Hence, tris (8-hydroxyquinoline) aluminum (Alq_3) and 3,4,9,10-perylentetracarboxylic dianhydride (PTCDA) are of great interest to investigate. In this thesis a range of linear and nonlinear optical properties of tris (8-hydroxyquinoline) aluminum (Alq_3) and of 3,4,9,10-perylentetracarboxylic dianhydride (PTCDA) is presented.

The Organic Molecular Beam Deposition (OMBD), which is very similar to the Molecular Beam Epitaxy (MBE), is an ideal technique to fabricate organic molecular thin films,

organic heterostructures and organic optoelectronic devices for fundamental research purposes. High purity and high quality organic heterostructures can be fabricated at a base pressures ranging from 10^{-8}- 10^{-11} mbar. OMBD has the advantage of depositing nanometer controlled layer thicknesses. This is important in fabricating organic multilayered nanostructures. In addition, it offers the possibility to deposit organic layers on any surface such as organic, inorganic or metals without breaking the high vacuum.

With the improvement of fabrication techniques, nanostructured materials have drawn significant attention in wave propagating[74,75]. Metal-island films are good candidates for fabricating nano-structured materials since they have shown novel optical properties[76–78]. The random-island metal films expands its potential in surface enhanced optical effects which can be utilized in molecule or particle detection for biological sensor application [77,79,80]. The geometrical orientation of metal-island films can be varied or rearranged with thermal annealing and modifications of deposition conditions[81–83] to optimize its functionality. Randomly oriented metal-island films can be easily obtained at the early stage of OMBD process of few nanometer thick films. An alloy of 90% Mg and 10% Ag ($Mg_{0.9}$:$Ag_{0.1}$) was used for the metal layers in this study.

OMBD was used in fabricating organic molecular thin films, organic multilayers and hybrid organic-metal hybrid structures in this thesis. In this chapter, few important details of Alq_3 and PTCDA molecules are presented in Section 2.2. The OMBD technique and the fabrication of organic and metal layers are introduced in Section 2.3. In addition, the morphological characterization of OMBD grown thin films is presented in Section 2.4.

2.2 Organic molecules

2.2.1 Tris (8-hydroxy) quinoline aluminum (Alq_3)

Tris (8-hydroxy quinoline) aluminum which is known as aluminum quinoline (Alq_3) is a commonly used electron transport and photon emitting layer in organic light emitting diodes (OLEDs) [11,84–87]. Alq_3 based OLED structures are now commercially available in light-weight colour flat screen displays of mobile phones, TV screens and laptops. Therefore Alq_3 is one of the rigorously investigated organic materials in the development of OLEDs. Recently, Alq_3 has attracted attention in the development of white organic solid state light sources (WOLEDs) [10–12].

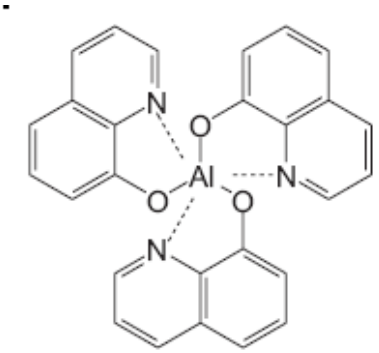

Figure 2.1: Chemical structure [89] of Alq_3

Alq_3 has a chemical formula [88–91] of $(C_9H_6NO)_3$-Al, which compose of three hydroxyquinoline ligands. Bulk Alq_3[89], shown in Figure 2.1, crystallizes in different polymorphic phases (α, β, γ, δ and ε) which can occur in meridional (*mer*) and facial (*fac*) stereoisomers [89,90,92–94]. Alq_3 forms quasi-amorphous or polycrystalline island growth [95] with few nanometer sized Alq_3 crystal grains with nearly isotropic optical properties. Polymorphous structure of the Alq_3 films

and the evidence for the existence of nanocrystals will be presented in Section 2.4.1. The influence of nano-crystalline structure in quasi-amorphous Alq_3 film on the light emission will be discussed in Chapter 3.

2.2.2 3,4,9,10 perylene tetracarboxylic anhydride

3,4,9,10 perylene tetracarboxylic dianhydride which is also known as PTCDA is one of the most intensively studied organic material in the aspects of structural, optical and electrical properties. PTCDA single molecule has a planer rectangular geometry with a chemical formula of ($C_{24}O_6H_8$) [96] as shown in Figure 2.2. PTCDA is a thermally stable red dye pigment. PTCDA molecules form polycrystalline films in the monoclinic space group $P2_1/c$ with two different modifications (the α- and β-phase [96]), both possessing two nearly coplanar molecules within the unit cell [28]. In both modifications the planar molecules form stacks along the *a*-direction that is slightly tilted with respect to the (102) growth direction [28]. The uniform orientation of molecules

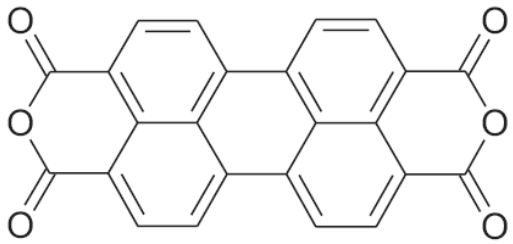

Figure 2.2: Chemical structure of PTCDA [96].

within all stacks results in a layered structure where the molecules are parallel to the (102) lattice plane which itself is parallel to the substrate surface. The distance between next neighbour (102) planes is shorter (0.332 nm) resulting in a large overlap of molecular π-orbitals [3,4,97]. Due to the difference in stacking of PTCDA molecules within the molecular plane or along the molecular

stacking direction [96] (which is nearly normal to the molecular plane), PTCDA nanocrystals and films show a strong optical anisotropy [98].

2.3 Fabrication of organic thin films and waveguide structures

2.3.1 Organic molecular beam deposition (OMBD) technique

The OMBD system has a base pressure ranging from 3.0×10^{-8} to 8.0×10^{-8} mbar. A photograph of the OMBD system is shown in Figure 2.3. The OMBD system mainly consists of a growth chamber and a load-lock. The system has two sets of turbo-molecular pumps with oil free

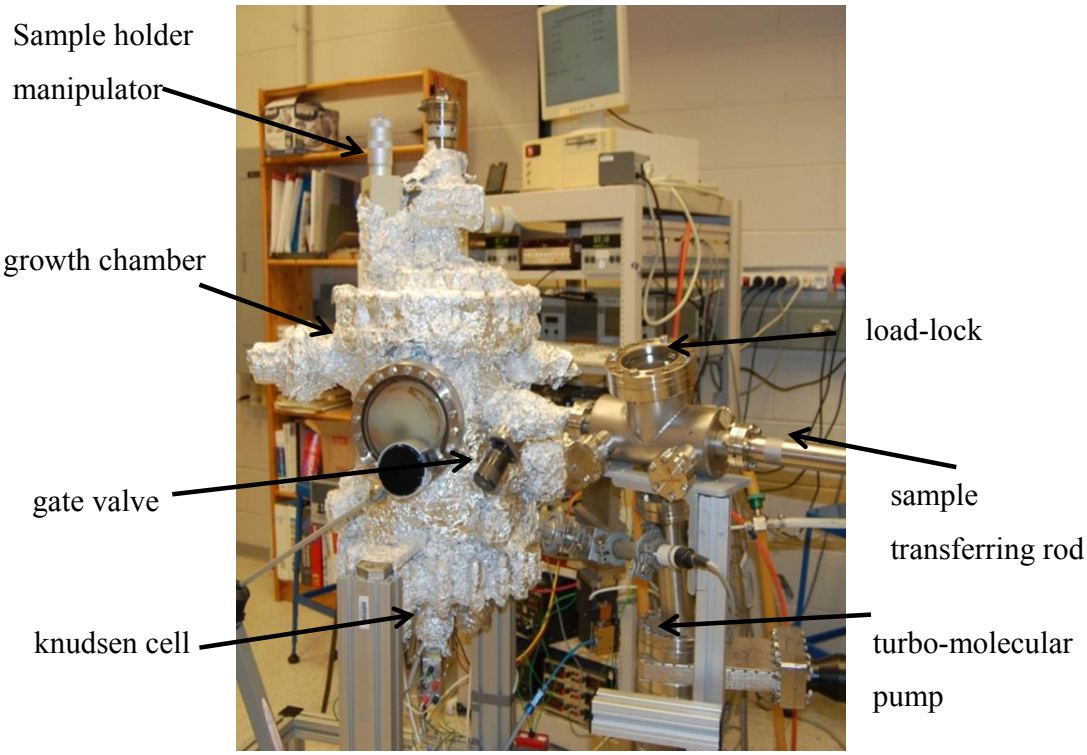

Figure 2.3: A photograph of the OMBD system

mechanical pump to maintain the high vacuum in the growth chamber and in the load-lock. The chamber and the load-lock are connected by a gate valve (see Fig. 2.3) which can be opened when transferring the sample holder from chamber to the load lock or vice versa using the transferring rod without breaking the high vacuum in the growth chamber. The chamber consists of five Knudsen cells which are equipped with computer controlled mechanical shutters. Three cells are filled with organic materials, PTCDA, Alq_3 and TPD. Other two cells are filled with metals: Mg-Ag alloy and gold. Each cell is equipped with a heating coil, which is connected to a power supply. Also each cell has a thermocouple which has been connected to a controller. Normally, the temperature of the cells is maintained at 110 $^{\circ}$C to out gas the materials. The substrate holder is attached to a manipulator which is located about 15 cm away from the Knudsen cells. Using the manipulator, the substrate holder can be moved in X, Y and Z direction and can be rotated around the Z axis as needed. Recently, the manipulator was equipped with a stepping motor to rotate the substrate holder during the sample growth at a certain frequency in order to deposit layers with uniform thickness. The growth chamber is also equipped with a quartz crystal thickness monitor, which can be moved in near the substrate holder to measure the growth rate and the film thickness.

2.3.2 Sample preparation and growth

Organic and metal thin films and waveguide structures are deposited on an area of ~1x1 cm^2 amorphous Pyrex® substrates of 0.5 mm thickness or on a 0.5 mm thick chemically clean n-type (001) oriented Si wafer at room temperature. The substrates were cleaned in an ultrasonic bath

with acetone, methanol and ultrapure water and dried with dry nitrogen gas. Then the substrate was quickly transferred into the high vacuum OMBD chamber.

The deposition rate was measured using the quartz crystal thickness monitor which has been calibrated by film thickness measurements using profilometer. Typical deposition rates from the effusion cells are 0.1 Å/s at a temperature of 330°C for PTCDA, 0.1 Å/s at a temperature of 236 °C for Alq_3. $Mg_{0.9}$:$Ag_{0.1}$ was degassed for 5-10 minutes at the evaporation temperature (395 °C) before the layer deposition. After the out gassing the substrate or the substrate with organic layer/s was placed in the growth chamber. The deposition rate of 0.5 Å/s at a temperature of 395 °C was used to deposit $Mg_{0.9}$:$Ag_{0.1}$ layers.

2.4 Morphological characterization of OMBD grown thin films

2.4.1 Nano-crystalline structure in quasi-amorphous Alq_3 film

In order to investigate the layer morphology during the initial growth period, ultrathin Alq_3 films with nominal thicknesses of 5, 10 and 15 nm were deposited on Si substrates by OMBD. The ultrathin films were investigated by atomic force microscopy (AFM) and scanning electron microscopy (SEM). A NanoScope Analysis image processing software was used to process the AFM images. The resulting AFM images for different layer thicknesses are displayed in Figs. (b) to (d). The AFM image of the Si substrate is illustrated in Fig. (a) as a reference. The Si substrate shows a slight texture with a minimum to maximum height variation of less than ±1 nm. The

Alq_3 film starts depositing as an irregularly shaped island structure with form irregularly shaped

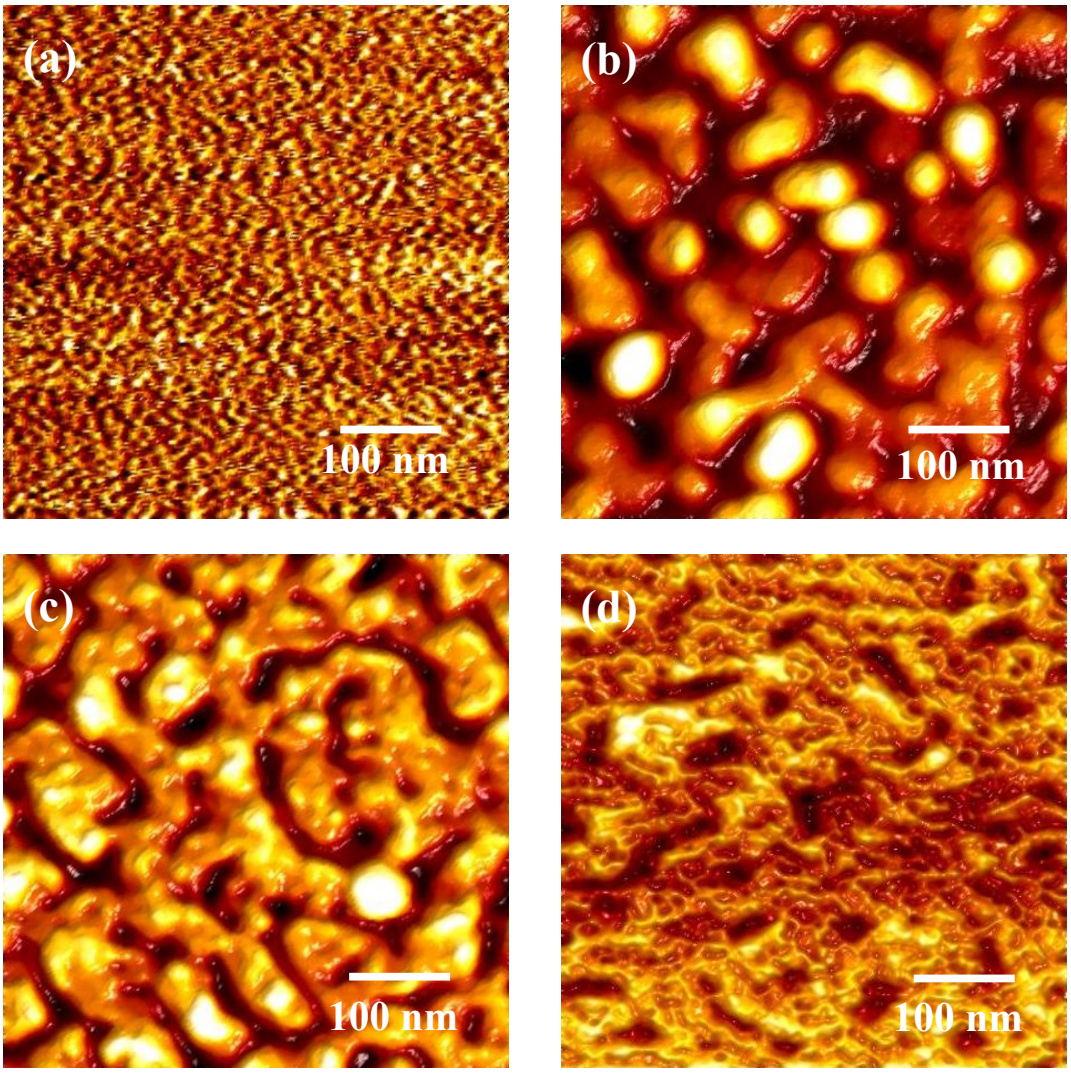

Figure 2.4: Atomic force microscope (AFM) images of (a) a Si substrate for reference and Alq_3 layers with nominal layer thicknesses of (b) 5 nm (c) 10 nm and (d) 15 nm deposited on Si substrate. The AFM images show that the Alq_3 film is composed of irregularly shaped ~30 to 70 nm sized nanoparticles.

"nanoworm" structures revealing additional new islands on top (see Figs. (c) and (d)).The observed structure is consistent with a quasi-amorphous or polycrystalline Alq_3 film growth. The

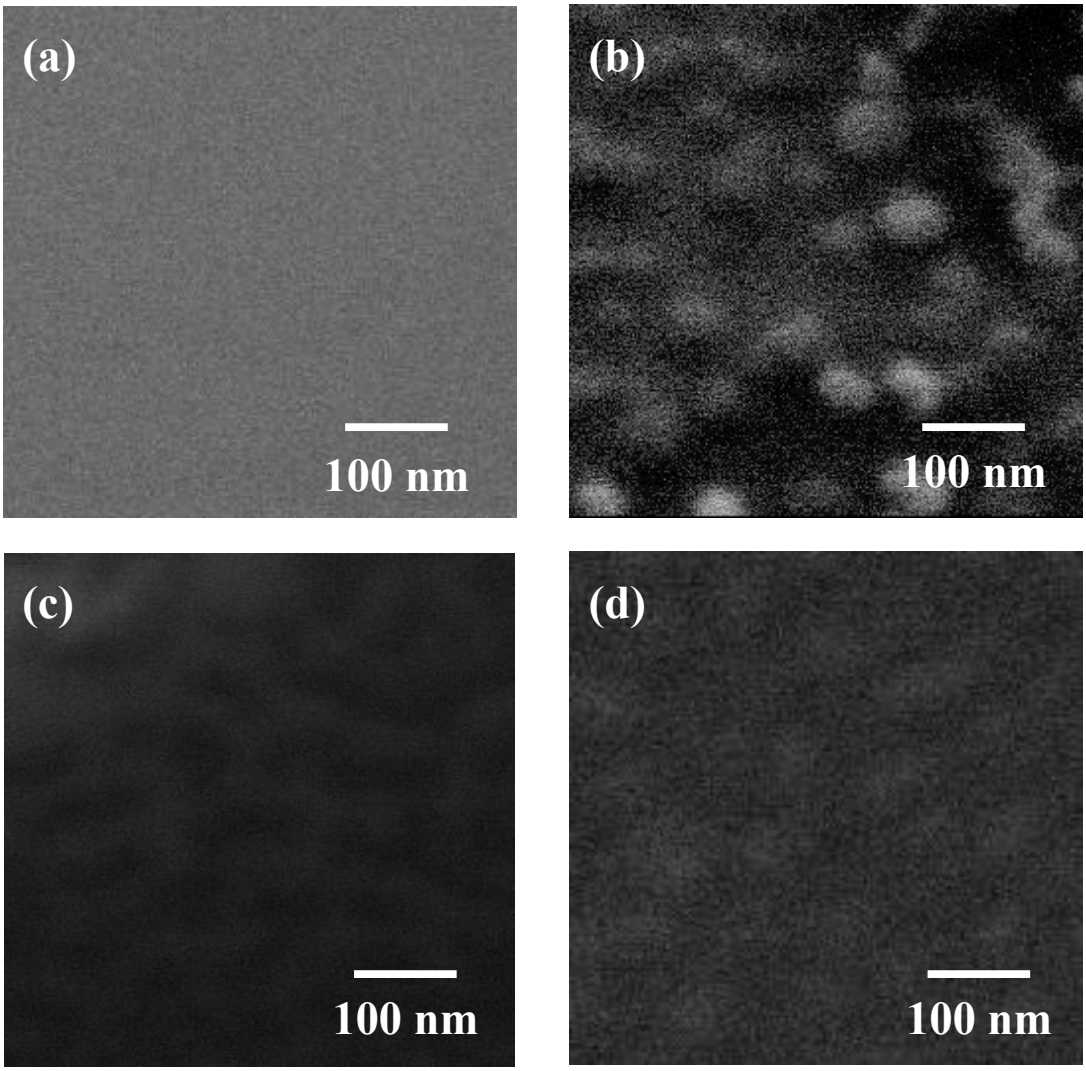

Figure 2.5: Scanning electron microscopy (SEM) images of (a) a Si substrate for reference and Alq_3 layers with nominal layer thicknesses of (b) 5 nm (c) 10 nm and (d) 15 nm which were deposited on Si substrate.

SEM images from the same Alq_3 layers are shown in Figure 2.5 (b) to (d) confirming the experimental findings obtained from the AFM investigations. Figure 2.5 (a) shows the SEM image of the uncoated Si subsrate as a reference for comparison. The SEM images were obtained at a low electron energy of 5 keV to avoid electrostatic charge build up at the dielctric Alq_3 layer surface which causes blurry images with a reduced image resolution. AFM and SEM studies of

ultrathin (5 – 15 nm) Alq_3 films provide clear evidence for the existence of nanocrystals or polycrystalline growth with grain sizes in the order of 50 nm.

2.4.2 OMBD grown metal islandic films

The continuousness of our OMBD grown Mg:Ag films was studied by atomic force microscopy

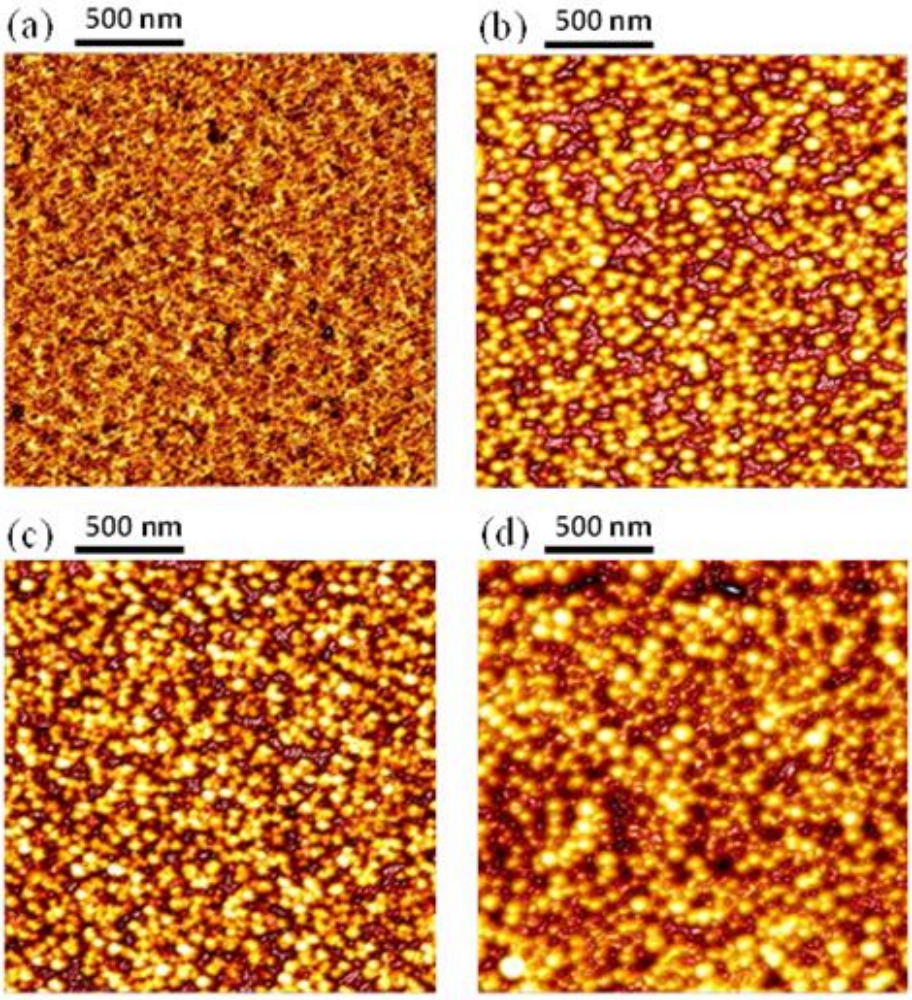

Figure 2.6: Atomic force microscope images of (a) a 50 nm thick Alq_3 layer for reference and of Mg:Ag layers with nominal layer thicknesses of (b) 5 nm (c) 10 nm and (d) 15 nm which were deposited on top of a 50 nm thick Alq_3 layer.

(AFM) on very thin Mg:Ag layers with nominal thicknesses of 5, 10 and 15 nm which were deposited on a 50 nm layer of Alq_3. The AFM image of the 50 nm thick Alq_3 is shown in Figure 2.6 (a) as a reference. The surface of the Alq_3 film reveals a slight texture with a minimum to maximum height variation of -2 to +2 nm. As illustrated in Figure 2.6 (b) – (d) the Mg:Ag film deposits as an island structure with island diameters ranging from 40 to 90 nm. The average height of the metal-islands in the three deposited films are found to be be 4.8, 9.7 and 13.8 nm and comprise a filling factor of 69±4%, 81±2%, 90±3%, respectively.

Chapter 3 Intensity and temperature dependent bimolecular quenching of light emission in Alq_3 films

3.1 Introduction

Tris (8-hydroxy) quinoline aluminum (aluminum quinoline, Alq_3) is a commonly used electron transport and photon emitting layer in organic light emitting diodes (OLEDs) which are now commercially available in flat panel displays for TV screens, mobile phones and laptops. Alq_3 is of interest in the development of white organic solid state light sources (WOLEDs) [10–12]. To enhance the light out-coupling of organic light emitting diodes different carrier transport film and device layouts were proposed [21–24] including the use of nanomesh electrodes and micro-lens arrays [99]. Recently, to enhance the environmental stability and emission yield of Alq_3 containing OLEDs [25], the properties of hybrid Alq_3/ZnO composite films were investigated. Since the main focus is in the investigations on Alq_3 based electronic devices and improving its functionality, the influence of ordered molecular aggregations [26,27] or nano-crystalline structure in quasi-amorphous Alq_3 film and its influence on the light emission is not fully understood yet. Charge carrier hopping within a positional random and disordered system of localized states is an appropriate model to describe exciton quenching in doped and undoped non-crystalline organic semiconductors [100–102]. So far charge carrier hopping was used to describe bimolecular

quenching in Alq_3 films at room temperature at high excitation levels [103–105] without considering the granularity [106] or ordered molecular aggregation in quasi-amorphous Alq_3 films. The interaction between excitons which are trapped in local minima at the grain boundaries between ordered (molecular aggregate or nanocrystalline) several 10 nm sized Alq_3 regions was only recently proposed and experimentally investigated [95]. A more detailed understanding of the directed migration of excitons to the energy minima at grain boundaries in and subsequent bimolecular quenching at these traps has technological relevance to better control the recombination process in Alq_3 based OLEDs.

Bulk Alq_3 crystallizes in different polymorphic phases (α, β, γ, δ and ε) which can occur in meridional and facial stereoisomers [89,90,92–94] showing a distinct vibronic progression in their emission spectra. No vibronic progression is observed in the photoluminescence (PL) spectrum of thin quasi-amorphously grown Alq_3 films [89,90,92,95]. This is explained by the polymorphous structure of the films that contain all possible crystalline modifications on a small, several 10 nm nanometer length scale which causes significant inhomogeneous broadening of the vibronic sub-bands. In addition, the polymorphism causes both extended and isolated potential minima below the mobile Frenkel exciton energies at the grain boundaries of the nanocrystals [84,86,95]. Optically excited mobile Frenkel excitons which are generated in ordered regions relax via directed motion into these energy traps. The aggregation of excitons at these energy minima leads to a high local (microscopic) exciton density resulting in small distances between excited molecules and hence efficient bimolecular quenching.

In an earlier investigations [107] of optically excited Alq_3 films it was demonstrated that the resulting high *local* exciton densities in such traps lead to bimolecular quenching even at

moderate excitation pulse fluences. In Section 2.4.1, the morphology of nominally 5-15 nm thick ultra-thin Alq_3 films was investigated with atomic force microscopy (AFM) and scanning electron microscopy (SEM) to support the existence of molecularly ordered (nanocrystalline) areas on a several 10 nm length scale. In addition, and newly, we investigate the saturation of singlet-singlet annihilation coefficient as a function of the excitation density. Experimental details are given in Section 3.2. The saturation behavior is studied using time-resolved (TR) and time-integrated (TI) detection methods. To investigate the intensity *and* temperature dependence of the quenching coefficient a photodiode was used as a detector. The simplified set-up provides a higher measurement accuracy as in pulsed excitation[95] and also allows the detection of light emission at very low excitation densities. The obtained experimental PL yield is compared with a coupled rate equation model for steady state excitation. Our experimental findings using time-resolved (TR) and time-integrated (TI) detection methods will be discussed and compared in Section 3.3.

3.2 Experimental Details

3.2.1 Time resolved photoluminescence measurements

An OMBD grown Alq_3 film with a thickness of 120 nm on a Si (001) substrate was used for this investigation. To analyse the dynamics of the exciton emission the Alq_3 film was excited by a frequency doubled Ti: Sapphire laser providing infrared 100 fs laser pulses (at λ = 814 nm) at a repetition rate of 80 MHz. Since the lifetime of trapped excitons in Alq_3 films is in the range of 20 ns in earlier measurements [95] the pulse repetition rate was reduced from 80 MHz to 4 MHz (or

~250 ns repetition time) by an acousto-optic pulse selector. The pulse repetition time of 250 ns gives the excited molecules sufficient time to relax back to their highest occupied molecular orbital (HOMO). The laser pulses were subsequently frequency doubled by a Bariumborate (BBO) crystal to generate pulses with an excitation wavelength of λ = 407 nm (~3.04 eV). The contrast ratio of the first-order diffracted pulses compared to the blocked zero-order pulses frequency doubled pulses was higher than 10000. The average power of the light pulses has been varied between 1 and 152 μW. For the time resolved PL measurements a lens with a focal length of 125 mm was used to collimate the 3.0 mm diameter wide pulsed laser beam onto the sample resulting in an excitation area of 3.8 x 10^{-6} cm^2 on the film. The time-integrated PL was spectrally resolved in a spectrometer and measured with a GaAs photomultiplier as detector. Time-resolved decay traces were recorded at the spectral position of the maximum Alq_3 emission (at approximately 520 nm) using the technique of time-correlated single photon counting (TCSPC) with a response time of less than 1.5 ns. A closed-cycle He cryostat was used for variable temperature measurements between 10 and 300 K.

3.2.2 Spectrally and time-integrated photoluminescence measurements using a photodiode

For spectrally and time-integrated photoluminescence (PL) measurements the Alq_3 films were excited by a continuous wave (cw) GaN based laser diode at ~3.04 eV (λ = 407 nm). The excitation power was varied between ~1 μW and 1.3 mW. As for the pulsed excitation a lens with a focal length of 125 mm was used to collimate the 3.0 mm diameter wide laser beam onto the sample. The Alq_3 emission was analyzed using a calibrated photodiode (Hamamatsu fast Si

photodiode S3071) which was connected to a high-speed Agilent digital multi-meter. A GG 425 filter was used on the photodiode to block the incident laser emission. In addition a KG 5 filter was used to block any luminescence from the Si substrate in the infrared spectral region. The sample was exposed to different laser light intensities for 2 seconds during which the spectrally integrated signal was recorded by the digital multi-meter. The light intensity was changed from low to high values at each temperature to minimize possible film degradation at highest excitation density. After the measurement at highest intensity the measurement at lowest intensity was repeated. In case there was a discrepancy in the signal response, the sample was moved to an adjacent spot which showed a similar count as in the first lowest intensity measurement before starting a new measurement series at the next higher temperature. The measured background was subtracted from each recorded signal.

3.3 Experimental Results

3.3.1 Spectrally resolved TI photoluminescence at different temperatures

Figure 3.1 shows the PL spectra of a 120 nm thick Alq_3 film at the temperatures of 15, 170 and 300 K at a light pulse energy of 3.04 eV and an energy fluence of 8.5 $\mu J/cm^2$. The PL spectra show a broad emission band which is attributed to the polymorphous growth of an Alq_3 film containing all possible crystalline modifications [89,90,92,108,109] within short-range ordered (nano-crystalline) areas. As reported earlier [95] the PL peak intensity increases at such high fluence with increasing temperature. At ~170 K the PL peak intensity is enhanced by a factor of more than 2

and the emission maximum shifts by approximately 25 meV to lower energies. Above 300 K the PL intensity decreases to about 2/3 of the intensity at 170 K and the band maximum further shifts to lower energies. This result is similar to the temperature dependence that has been observed in a 90 nm thick Alq_3 film observed by a different group [110] who attributed the observed PL enhancement between 15 and 190 K to an increasing number of thermally activated intermolecular delocalized Frenkel excitons with high emission rate. In contrast to their

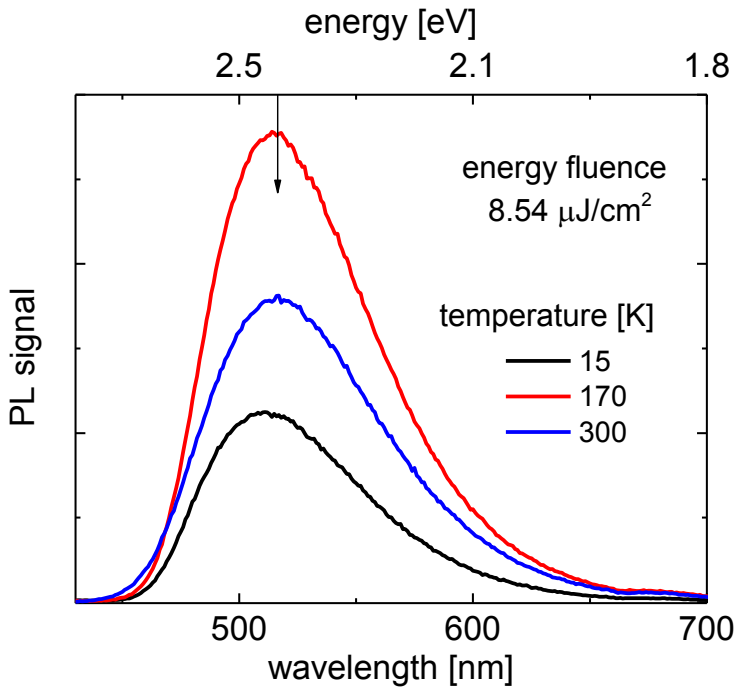

Figure 3.1: PL spectra at a light pulse energy of 3.04 eV (λ= 407 nm) and an energy fluence of 8.5 μJ/cm^2 at different temperatures as labelled. The arrow indicates PL maximum at ~2.384 eV (λ = 520 nm) which was used as detection energy for the time-resolved PL

interpretation our intensity dependent PL measurements demonstrated [107] that the PL signal reduction at low temperature (15 K) is due to the bimolecular quenching of trapped excitons which are localized in the potential minima at the grain boundaries between the several 10 nm

small Alq_3 nanocrystals. While no structural evidence for the existence of such nanocrystals was given in the previous study [107], the AFM and SEM images of ultrathin films are shown in Figure 2.4 and Figure 2.5 in Section 2.4 clearly support that the Alq_3 film is composed of differently shaped and ~50 nm sized nanoparticles in the Aq_3 films. The reduction of the PL quenching and the observed red-shift of the emission maximum with increasing temperature is attributed to a thermally activation of trapped excitons into non-quenchable radiative states with higher localization energy. These states are located within or in close vicinity of the extended trapping sites which are for instance caused by fluctuations in the molecular environment. Thermally activated charge-transfer (CT) or excimer-like states where the wavefunction of the exciton is partially delocalized between two adjacent molecules could also contribute to the reduction of bimolecular quenching. Further increase of the temperature reduces the PL efficiency due to de-trapping and subsequent migration of excitons into non-radiative traps.

3.3.2 Time resolved photoluminescence measurements at different pulse fluences

The singlet-singlet annihilation of excitons which are trapped in extended potential minima at 15 K becomes clearly visible in pulse fluence dependent PL time traces which were acquired in TCSPC experiments. Figure 3.2 shows the time traces of a 120 nm thick Alq_3 film at excitation energy fluxes ranging from 0.1 to 10 $\mu J/cm^2$ at a detection energy of 2.384 eV (λ = 520 nm) which is close to the PL maximum indicated as an arrow in Figure 3.2. For comparison the TR PL signals at different excitation intensities were normalized. At high excitation densities the PL traces show a pronounced non-exponential decay. At highest excitation density (10 $\mu J/cm^2$

fluence per pulse) the time-integrated normalized PL intensity is reduced by a factor of ~2 compared to the value obtained at lowest fluence of 0.1 μJ/cm^2 (not shown here). The increasing decay and reduced time-integrated PL yield indicate the presence of singlet-singlet annihilation processes at high excitation densities.

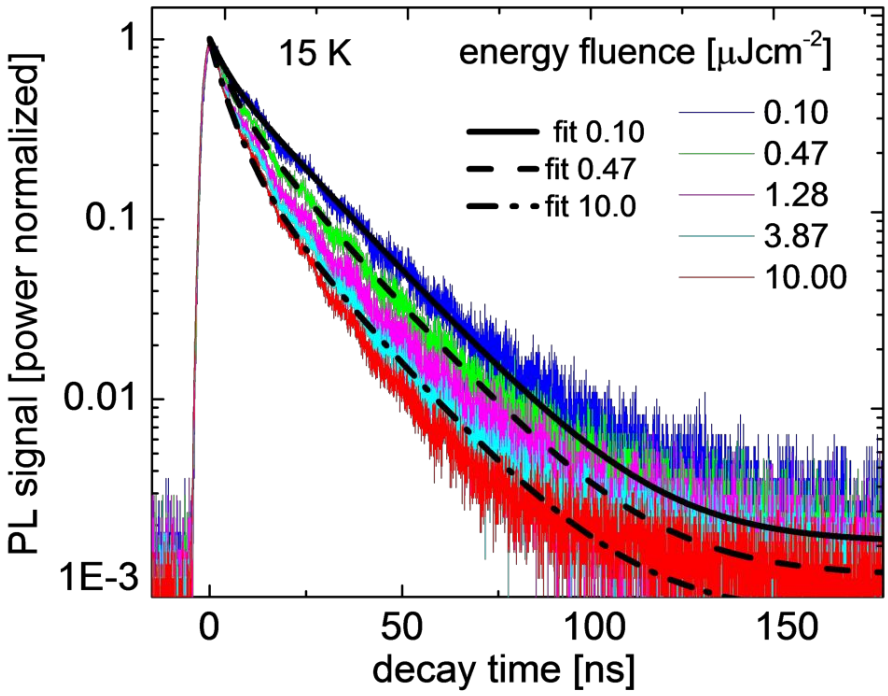

Figure 3.2: Normalized time resolved PL signal obtained from a 120 nm Alq_3 film at 15 K as a function of the incident energy fluence as labelled. Thick full, dashed and dash dotted black lines are numerical fits as described in the text.

To explain the observed bimolecular quenching at 15 K and the temperature dependence at higher temperatures we consider that the optically excited Frenkel excitons in the Alq_3 nanocrystals relax quickly (on a picosecond timescale) into their HOMO n =0 vibronic state. These relaxed "quasi-free" Fenkel excitons migrate within the weakly disordered nanocrystal via

intersite transport until they get trapped in the potential minima at the grain boundaries between different Alq_3 nanocrystals. This results in a significant local (microscopic) exciton density

Table 3.1: Fitting parameters of TRPL measurements shown in Figure 3.2 at 15 K and for the temperature dependent model shown in Figure 3.5. The incident photon densitiy n_{photon} per pulse and initial exciton densities $n_{Frenkel}$, $n_1(0)$, $n_2(0)$ are given at a fluence of 1 $\mu J/cm^2$.

A_1	0.34
τ_1	4.2 ns
A_2	0.72
τ_2	19.0 ns
γ_1	2.4×10^8 s^{-1}
γ_2	5.2×10^7 s^{-1}
γ_f	5.0×10^9 s^{-1}
γ_{fr}	5.2×10^7 s^{-1}
γ_{1r}	5.2×10^7 s^{-1}
γ_{2r}	5.2×10^7 s^{-1}
γ_{3r}	5.2×10^7 s^{-1}
γ_{1nr}	1.85×10^8 s^{-1}
γ_{23}	6.5×10^8 s^{-1}
n_{photon}	2.05×10^{13} cm^{-2}
$n_{Frenkel}(0)$	6.50×10^{16} cm^{-3}
$n_1(0)$	9.80×10^{15} cm^{-3}
$n_2(0)$	2.05×10^{16} cm^{-3}
Δ_1	90 meV
Δ_2	100 meV
Δ_3	145 meV
Δ_b	20 meV
Δ_l	45 meV

enhancement at the grain boundaries which leads to an efficient PL quenching even at moderate fluences. The PL efficiency quenching is weak at lowest fluence.

A bi-exponential fit (see full black line) that neglects weak radiation from longer living states and weak bimolecular quenching at lowest incident fluence of 0.1 $\mu J/cm^2$ reveals a short lifetime of T_1 = 4.2 ns and a long lifetime of T_2 = 19.0 ns with amplitudes A_1 = 0.34 and A_2 = 0.72 which are attributed to two different and locally separated trapping sites with exciton densities $n_1(t)$ and $n_2(t)$. The excitons with density $n_1(t)$ are attributed to excitons which are localized in disordered or defective areas containing radiative as well as non-radiative molecules. Trapped excitons with density $n_2(t)$ are localized in more ordered trapping sites which possess significantly less defective areas. We therefore neglect non-radiative processes for n_2 excitons and approximate the measured lifetime of 19.0 ns to be essentially equal to the radiative lifetime "quasi-free" excitons. For excitons n_1 in more defective traps we assume the same radiative lifetime and estimate a non-radiative decay rate of $\gamma_{nrad} = 1.85 \times 10^8\ s^{-1}$ or a non-radiative lifetime 5.4 ns. From the measured amplitude ratio A_1:A_2 = 0.476 of the fitted PL trace we find a density ratio of $n_1(0)$:$n_2(0) \approx 1$:2. The obtained low-intensity values are summarized in Table 3.1.

Subsequently, we analysed the PL traces at higher energy fluences (0.47 to - 10 $\mu J/cm^2$ per pulse) which show singlet-singlet annihilation. Since excitons in defective traps have a lower density $n_1(t)$ and a reduced exciton diffusion as compared to excitons in ordered traps with density $n_2(t)$ we neglect bimolecular quenching between excitons with density n_1. The initial densities $n_1(0)$ and $n_2(0)$ at a specific pulse fluences were determined as described in Ref. [95] considering an absorption coefficient of with α being ~4 x 10^4 cm^{-1} [105,111,112]. The ratio of the TI

PL traces at lowest energy fluence at 15 and 300 K efficiency results in a PL efficiency in this Alq_3 film of approximately ~35 % at 15 K (compared to 25% at room temperature [111,113,114]). The difference in the efficiency value at 15 K as well as the slightly different radiative and non-radiative lifetimes of the trapped excitons compared to the Alq_3 film investigated in Ref. [95] is attributed to variations of the growth temperature or to different long exposure to ambient atmosphere [115]. Resulting values of initial trapped exciton densities $n_1(0)$ and $n_2(0)$ per 1 $\mu J/cm^2$

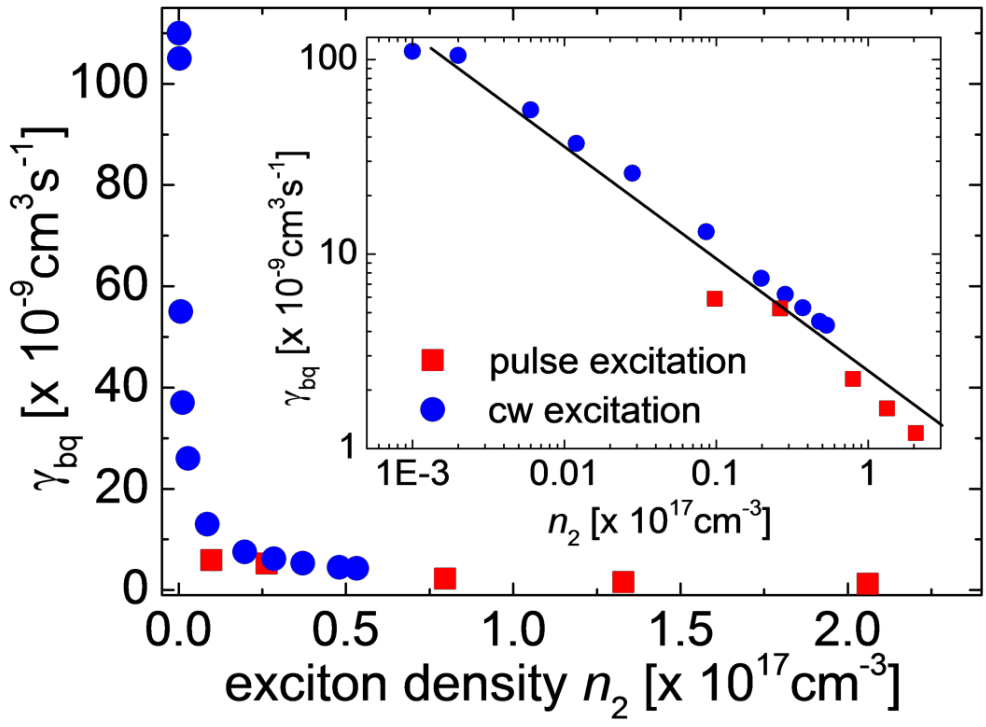

Figure 3.3: Extracted bimolecular quenching coefficients γ_{bq} as a function of the initially generated trapped exciton density $n_2(0)$ with pulsed excitation (red squares) and steady state exciton density n_2 at cw excitation (blue dots) at an incident light energy of 3.04 eV (λ=407 nm). The inset shows a double logarithmic plot of γ_{bq} versus density n_2 revealing that the quenching coefficient follows a monomial expression (black line) given by Eq. (3.7).

incident fluence are given in Table 3.1. Fitted curves including bimolecular quenching are exemplarily shown for fluences of 0.47 and 10 $\mu J/cm^2$ with are shown as dashed and dashed-dotted full black lines, respectively in Figure 3.2. Figure 3.3 shows the bimolecular quenching coefficients γ_{bq} as a function of initially generated excitons $n_2(0)$. The bimolecular quenching coefficients γ_{bq} were obtained from fitting the PL traces at all incident pulse fluences. With increasing pulse fluence we observe a reduction and saturation of γ_{bq} which is consistent with the finite density of quenchable trapping sites in the Alq_3 film. Excitons exceeding the density of the deepest trapping sites at the grain boundaries have to reside in the vicinity of the occupied traps or at more extended trapping sites with higher energy. This increases the *average* excited molecule distance and thus reduces the value of the bimolecular quenching coefficient at a distinct exciton density n_2. After the annihilation of excitons residing in the deepest traps higher energy excitons may subsequently relax into these traps. This retarded refilling of the deepest traps extends the total interaction time of annihilation processes and might explain the slightly poorer fitting of the time traces in Figure 3.2 at high excitation densities.

3.3.3 Spectrally integrated photoluminescence yield at different incident light intensity and temperatures

In order to investigate the intensity *and* temperature dependence of the bimolecular quenching effect we performed time-integrated PL measurements on the *same* Alq_3 film at temperatures ranging from 15 to 300 K. Different to earlier temperature dependent investigations [95] the emitted light from the Alq_3 film was measured as spectrally integrated signal with a photodiode. The excitation intensity of the cw light provided from a GaN based laser diode at ~3.04 eV (λ =

407 nm) was varied between ~0.32 and 342 W/cm^2. The PL efficiency measured as a function of the temperature for different incident light intensities is shown in Figure 3.4. Like in the TR PL measurements the PL yield was assumed to be 25% at 300 K at lowest intensity according to literature values [111,113,114]. In agreement with the TR PL measurements the PL efficiency significantly decreases by more than a factor of 2 with increasing light intensity at 15 K. The bimolecular quenching effect also reveals a clearly visible saturation at highest excitation

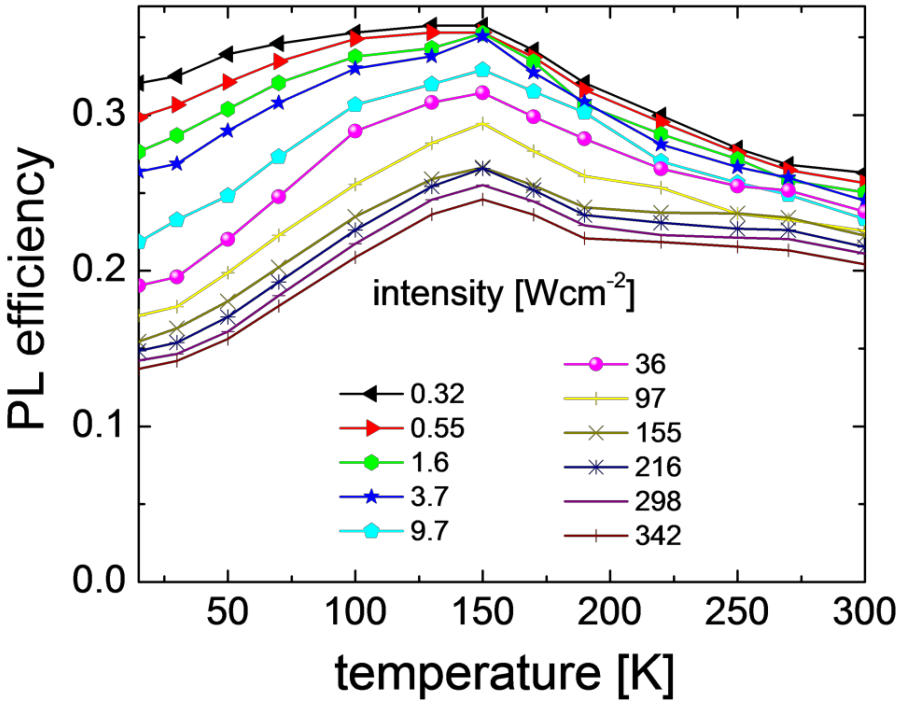

Figure 3.4: Measured time-integrated PL efficiency as a function of the temperature for different incident light intensities as labelled using a cw light excitation from a GaN based laser diode at ~3.04 eV (λ = 407). The emitted light was spectrally integrated using a photodiode.

densities which is consistent with the observation using pulsed excitation presented in Section 3.3.2. With increasing temperature the quenching effect decreases showing a PL yield maximum

at around ~150 K. The maximum of the PL yield is somewhat higher at low intensities as compared to high excitation intensities. As mentioned earlier the observed reduction of bimolecular quenching between trapped excitons with density n_2 as a function of temperature is attributed to a thermally activated occupation of non-quenchable states. Above 150 K the PL efficiency decreases due to the de-trapping of excitons and filling of non-radiative traps reaching a PL efficiency of ~25% at medium excitation levels. At highest intensity the PL efficiency is further reduced to 20% suggesting that bimolecular quenching between trapped n_2 excitons is weak but active even at room temperature. In order to support our interpretation and to determine the *average* bimolecular quenching coefficient at a distinct excitation intensity we modified the coupled rate equation model presented in Ref. [95] to the stationary case for cw excitation. The resulting equations are given by:

$$\phi_{photon} = \frac{P}{\hbar\omega\pi a^2} \tag{3.1}$$

$$0 = \phi_{photon}\alpha - n_f\gamma_{fr} - n_f\gamma_f + n_1\gamma_f \exp(-\frac{\Delta_1}{k_BT}) + n_2\gamma_f \exp(-\frac{\Delta_2}{k_BT}) + n_3\gamma_f \exp(-\frac{\Delta_3}{k_BT}) \tag{3.2}$$

$$0 = -n_1\gamma_{1r} - n_1\gamma_{1nr} + n_f\gamma_f C_1 - n_1\gamma_f \exp(-\frac{\Delta_1}{k_BT}) \tag{3.3}$$

$$0 = n_f\gamma_f C_2 - n_2\gamma_{2r} - \frac{1}{2}{n_2}^2\gamma_{bq} - n_2\Gamma_3(T) - n_2\gamma_f \exp(-\frac{\Delta_2}{k_BT}) + n_3\Gamma_3(T)\exp(-\frac{\Delta_l}{k_BT}) \tag{3.4}$$

$$0 = n_2\Gamma_3(T) - n_3\gamma_{3r} - n_3\gamma_f \exp(-\frac{\Delta_3}{k_BT}) - n_3\Gamma_3(T)\exp(-\frac{\Delta_l}{k_BT}) \tag{3.5}$$

In Eq. (3.1) the incident photon flux ϕ_{photon} is calculated from the power P of incident cw light power with energy $\hbar\omega$ = 3.04 eV using a focus radius of $a = 11\times10^{-4}$cm. An absorption

coefficient α = ~4 x 10^4 cm^{-1} was used to generate Frenkel excitons. In the coupled equations (3.2) to (3.5) n_f, n_1, n_2 and n_3 are the *macroscopic* densities of "quasi-free" excitons and of trapped excitons. $\Gamma_3(T) = \gamma_{23} \exp(-\frac{\Delta_b}{k_B T})$ is the thermally activated occupation rate of non-quenchable excitons n_3 with activation energy Δ_b. k_B is the Boltzmann constant. Constants $C_1 = n_1^0 / n_{tot}$ and $C_2 = n_2^0 / n_{tot}$ give the ratios of n_1, and n_2 state densities which are inside or in the vicinity of potential minima with more or less defective molecules, respectively, relative to the density of total available exciton states $n_{tot} = n_{NR}^0 + n_1^0 + n_2^0$ which also include the density of non-radiative centers. As described earlier in the TR PL experiments in Section 3.3.2 the density ratio of n_1^0 / n_2^0 is ~1/2 which was assumed to be a representative ratio for the spectrally integrated detection as well. From the time-integrated PL efficiency of ~35% at 15 K at low excitation intensities the densities of radiative excitons n_1^0 in more and n_2^0 in less defective traps and of non-radiative excitons (*NR*) amount to $n_1^0 = 0.16 \times n_{Frenkel}$, $n_2^0 = 0.32 \times n_{Frenkel}$ and $n_{NR} = 0.52 \times n_{Frenkel}$, respectively. Δ_1, Δ_2 and Δ_3 are localization energies with respect to the mobile ("free") exciton energy. These energies (together with activation energy Δ_b) determine the temperature at which the maximum PL yield occurs. γ_{fr} and γ_f are the radiative decay and capture rate of "free" excitons. γ_{1r}, γ_{2r} and γ_{3r} are the radiative and γ_{1nr} the (background) nonradiative rate of trapped excitons n_1, n_2 and n_3. The radiative rate γ_{3r} was determined from the low intensity time trace recorded at 170 K to be 5.2 x10^7 s^{-1}. γ_{bq} is the bimolecular

annihilation coefficient. In contrast to previous investigations [107] under pulsed excitation were the coefficient γ_{bq} was assumed to be intensity independent within the applied excitation fluence range the quenching coefficient is considered to be intensity dependent in this study. Its value was adjusted until optimum agreement between the experimentally measured efficiency and the calculated value at 15 K was reached. The parameter values that were used for the calculations are summarized in Table 3.1. They are close to parameters which were used in earlier temperature dependent calculations with pulsed excitation on a different Alq_3 sample also demonstrating the reproducibility of the bimolecular quenching effect in OMBD grown Alq_3 films. A more comprehensive explanation of the parameters and their derivation is given in Ref. [95].

Figure 3.5 shows the calculated density of emitted photons $n_{phe}(T)$ from trapped excitons n_1, n_2 and n_3 and free Frenkel excitons n_f for different incident light intensities as labelled according to

$$n_{phe}(T) = \gamma_{1r}\, n_1(T) + \gamma_{2r}\, n_2(T) + \gamma_{3r}\, n_3(T) + \gamma_{fr}\, n_f(T) \tag{3.6}$$

Also the individual contributions from trapped excitons n_1, n_2 and n_3 and free Frenkel excitons n_f to the light emission are shown at the highest intensity of 342 Wcm^{-2} per pulse. The calculated curves show good agreement with the experimentally observed temperature dependent PL yield up to 150 K when the bimolecular quenching coefficients γ_{bq} were adjusted to the PL value at 15 K. The calculated curves show a lower reduction of the PL yield for temperatures above 150 K which might be explained by thermal activation into intermediate non-radiative trap before

remobilizing excitons which is not considered in the present model. However, the overall trend of the temperature dependence is described correctly with the proposed model.

The deduced intensity dependent bimolecular quenching coefficient γ_{bq} for trapped states as a function of the calculated density n_2 at 15 K are shown in Figure 3.3 as blue squares. The quenching coefficient values γ_{bq} are similar to the values obtained from the pulsed experiments (red full circles) at corresponding exciton densities n_2. As for the TR PL measurements the

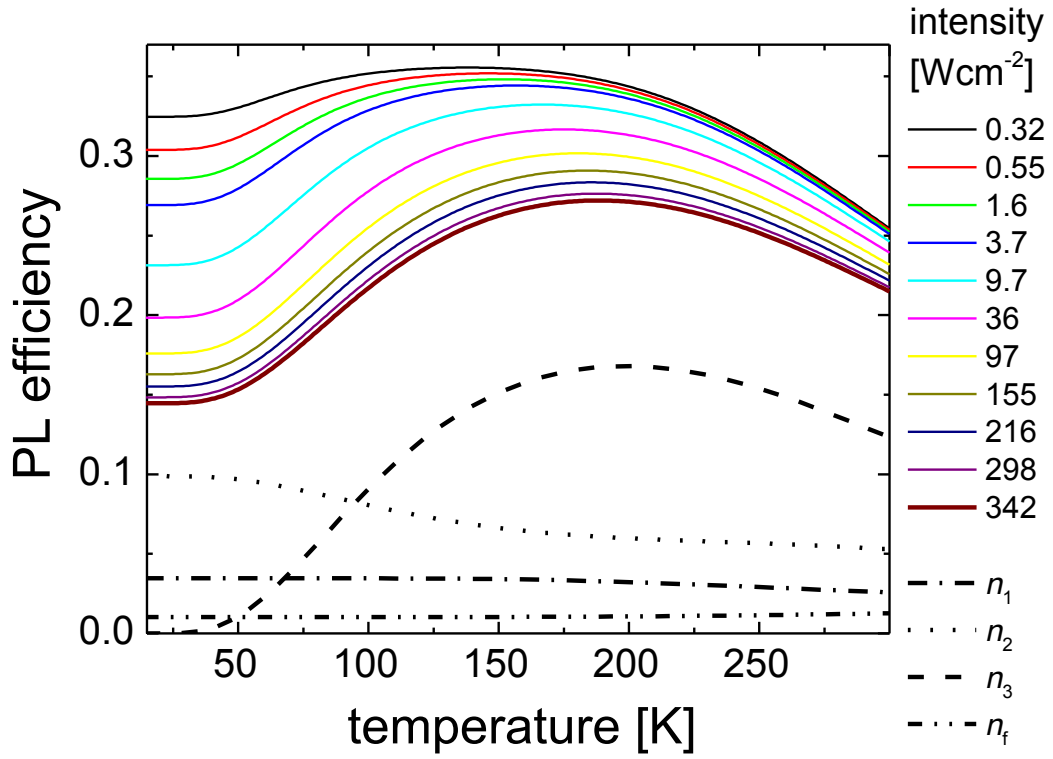

Figure 3.5: Calculated density of emitted photons $n_{phe}(T)$ from trapped excitons n_1, n_2, and n_3 and quasi-free Frenkel excitons n_f using Eq.(3.6) for different incident light intensities as labelled. Corresponding bimolecular quenching coefficients γ_{bq} are plotted in Figure 3.3.

quenching coefficient γ_{bq} shows the expected saturation with increasing excitation intensity. However, the maximum quenching coefficient γ_{bq} at lowest intensity amounts to ~110 x 10^{-9} cm^3s^{-1} thus about a factor 50 times higher as earlier reported values from pulsed experiments [95]. The results show that the saturation of quenching starts already at very low intensities. A double logarithmic plot (see inset in Figure 3.3) of γ_{bq} versus density n_2 reveals that the quenching coefficient approximately follows a monomial expression

$$\gamma_{bq}(n_2) = a\, n_2^{\,k} \tag{3.7}$$

with a constant a = 0.283 cm^3s^{-1} and an exponent of k = - 0.46. The behavior for γ_{bq} for pulsed excitation (red squares in Figure 3.3) slightly deviates from this behavior which is attributed to our assumption that bimolecular quenching can be neglected at lowest fluence. In particular the value deduced at the second highest fluence is affected by this approximation. The exponent k depends on the distribution of trapping sites with different sizes and localization energies which can accommodate a certain maximum number of excitons. The individual density of states of these trapping sites times the exciton occupation probability which is a function of the trapping energy and the successive filling of deepest traps determines the *average* microscopic distance between excited molecules. The resulting intermolecular distance is responsible for the measured average bimolecular quenching coefficient at certain excitation intensity. The nearly same quenching coefficient value deduced from the lowest and second lowest cw laser intensity indicates that the deepest traps are not yet filled by the generated n_2 therefore no saturation is observed at excitation intensities below 0.55 Wcm^{-2}.

Chapter 4 Refractive index dispersion and waveguiding in single and multi-layer organic films

4.1 Introduction

Organic semiconductor films have potential applications in opto-electronic devices such as organic light emitting diodes (OLEDs) [7–9], waveguide fabrication[116], photovoltaic devices[117] and photodetectors[15]. Organic materials can be easily deposited on a variety of substrates including low-cost and flexible substrates and also on any other organic materials[3,4] or on metal layers [5,6]. Effective medium multilayer waveguides made from different organic materials act as a homogeneous and anisotropic dielectric slabs which show natural birefringence. The dielectric properties of such organic effective medium multilayer structures open up unique opportunities to tailor waveguides with desired optical anisotropy and nonlinearity[28,29] . High quality organic heterostructures can be fabricated without lattice matching[1,2], which is an essential factor for the performance of many devices. Accordingly, organic multilayer structures are good candidates for applications in advanced opto-electronic devices such as multiple quantum well structures (MQWs) [1,118,119], organic light emitting diodes[118] and devices where polarization control is required[29,120].

In this chapter, 3,4,9,10-perylentetracarboxyl–anhydride (PTCDA) and aluminum quinoline (Alq3) were used to fabricate and study the dielectric properties of pure and multilayer waveguides. Both the organic films and multilayer, which is composed of alternating nanometer thick PTCDA and Alq_3 films, were deposited on Pyrex using OMBD. As described in Section 2.2.2, the different molecular stacking of PTCDA in the molecular plane (102) and along the stacking direction (*a* direction) which is nearly perpendicular to the (102) plane, PTCDA results in strong anisotropic optical and electrical properties [3,4]. In contrast to PTCDA, the propeller shaped Alq_3 molecules form in general quasi-amorphous films [95,121,122] with nearly isotropic optical properties. Therefore the combination of both materials in multilayer films is expected to be ideal to tune the birefringence and the refractive index dispersion of waveguide structures within a wide range.

The dispersion of the refractive indices of thin PTCDA[98,123,124] and Alq_3[112,115,125] films has so far mainly been measured with ellipsometry. The results for both materials scatter widely which is often explained by the different structural quality of investigated samples. Instead of using values from literature to design the PTCDA/Alq_3 multilayer I measured the in-plane and normal refractive indices of our OMBD grown PTCDA, Alq_3 films and PTCDA/Alq_3 multilayer at various wavelengths with the *m*-line technique[72,73]. Similar measurements have already been carried out on PTCDA films in earlier work [107,126], however, discrepancies to results obtained from ellipsometric spectroscopy motivated me to repeat *m*-line experiments on two new PTCDA layers with different film thickness.

The *m*-line technique (described in Section 4.3) is based on the coupling between light reflected in a high refractive index prism and propagating modes in a waveguide and requires

less involved modelling than ellipsometric investigations. It is also an ideal technique to experimentally determine the refractive index of effective medium Alq_3/PTCDA multilayer waveguides. Controlling of anisotropy and the dispersion of the refractive index by tailored multilayer waveguide is described in Section 4.6.

4.2 Waveguide Structures

Two PTCDA films of nominally 1.0±0.1 µm (labelled as waveguide P_1) and 0.5±0.05 µm (labelled as waveguide P_2) thickness and one Alq_3 film with 2.2±0.1 µm nominal thickness (labelled as waveguide A_1) were grown on Pyrex® substrate to determine the dispersion of the refractive index of the bulk materials. In addition, an alternating PTCDA/Alq_3 multilayer structure (labelled as M_1) was grown by OMBD. The multilayer structure comprises 33 PTCDA layers and 32 Alq_3 layers with PTCDA as the first and last layer. The nominal individual layer

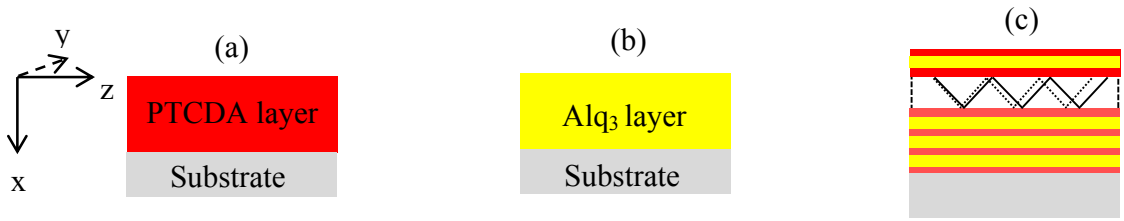

Figure 4.1: Schematic sketch of (a) a pure PTCDA waveguide (b) a pure Alq_3 waveguide and (c) the PTCDA/Alq_3 multilayer waveguide.

thicknesses of PTCDA and Alq_3 layers were 15 ± 2 nm and 20 ± 2 nm, respectively, resulting in a nominal total thickness of waveguide M_1 of 1.135 ± 0.13 µm. A schematic sketch of the pure as well as the multi-layered waveguides is shown in Fig. 4.1. Deviations from the nominal total growth thicknesses of the deposited pure and the multilayer films were determined using a profilometer prior to the optical investigation. Thickness variations of ~±20% due to oblique

growth across the sample area were determined for the PTCDA waveguides while no noticeable thickness variation was measured for the Alq_3 film. The thickness variations in the PTCDA film were considered in the numerical analysis.

4.3 *m*- line technique

A schematic sketch of the experimental set up for the *m*-line technique is shown in Figure 4.2. The *m*-line measurements on pure and multilayer waveguides were performed at excitation wavelengths ranging from the visible region (633, 638, 662 and 693 nm) using a He-Ne and

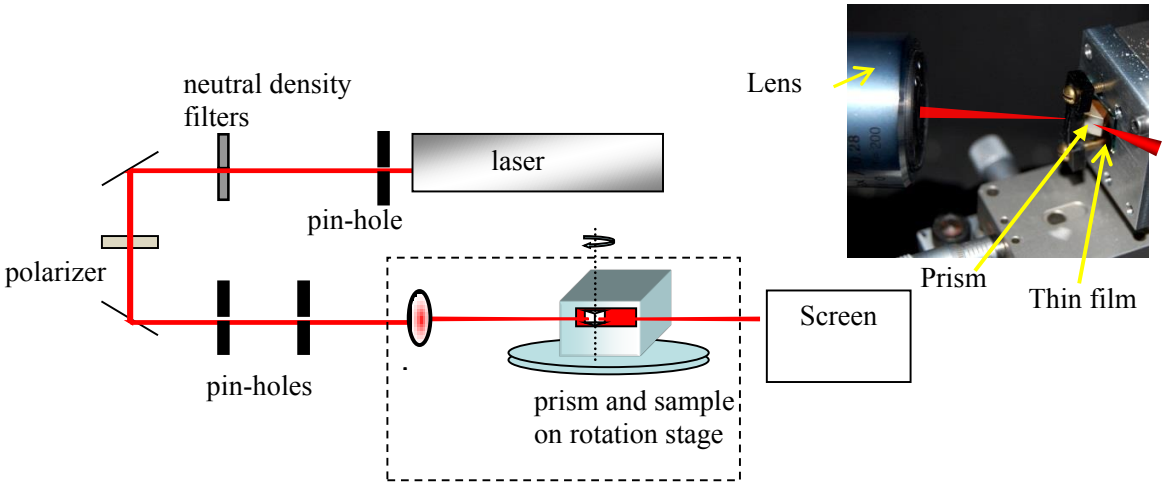

Figure 4.2: Schematic sketch of the experimental setup of the *m*-line technique

various GaAs based solid state continuous wave (cw) lasers to the infrared region (794, 814, 844, 894 and 914 nm) using a Ti:Sapphire laser in the cw mode. With neutral density filters the incident light power was kept below 1 mW to avoid light induced damage of the waveguides. The un-polarized He-Ne laser and semiconductor lasers were polarized with a sheet polarizer, the polarized Ti:Sapphire laser beam was rotated using a $\lambda/2$ retardation plate for TE or TM mode excitation. A 10 x microscope objective lens with a long working distance focused the polarized

laser beam onto the base of a 45°-90°-45° birefringent Rutile prism. The optical axis (*c*-axis) in the Rutile is oriented perpendicular to the unpolished triangles of the Rutile prism (parallel to the y-axis as denoted as $\otimes$ in Fig. 4.3). The film and glass substrate were clamped between the Rutile prism and a sample holder with a cylindrically shaped pressure area. A sketch of the side-view of the prism, the film on the substrate and sample holder is illustrated in Figure 4.3. The prism and the attached waveguide were mounted on a rotatable stage which allows changing the incidence angle θ_i with respect to the normal of the front face of the prism. The incident light couples to the waveguide modes when the z-axis component of the phase velocity of the light wave in the prism equals that of the propagating mode in the waveguide. The necessary phase matching can be achieved by adjusting the angle θ_i between the beam and the prism base with the rotatable stage. As shown in index ellipsoid of Rutile in Fig. 4.3, TE modes in the waveguide are excited when the electric field oscillation is parallel to the *c*-axis (parallel to the y-axis denoted as $\otimes$ in Fig. 4.3), while TM modes are excited when the electric field oscillation is perpendicular to the *c*-axis of the prism (within the x-z plane denoted as $\updownarrow$ in Fig. 4.3).When the coupling condition is met, a dark line (*m*-line) is observed in the reflected beam spot on a detector screen as seen in the photograph in Fig. 4.3. Each of these *m*-lines represents a different guided mode and appears at a different incident angle θ_i which is known as the synchronous angle. The incident angles θ_i, were measured for both the TE and the TM polarized light with an accuracy of 30 arc second (~0.01^0). To minimize the error these measurements were repeated three times at the incident angle θ_i on the same spot.

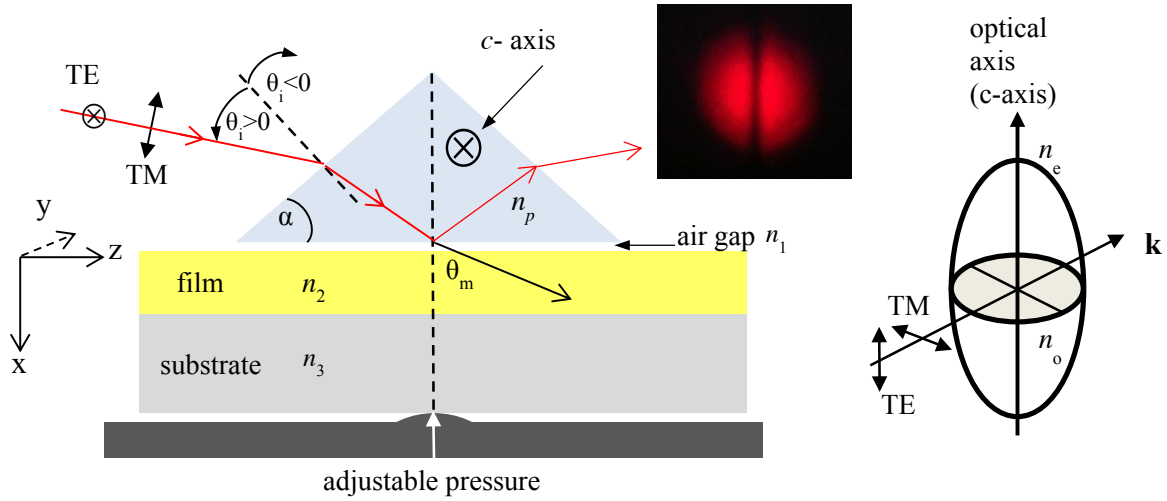

Figure 4.3: (a) Schematic sketch of the *m*-line technique showing the side-view of the prism, the film on the substrate and the sample holder. The photograph shows a dark *m*-line within the reflected laser spot which appears on a detector screen when prism coupling occurs. (b) Refractive index ellipsoid of Rutile.

4.4 X-ray characterization of organic films

In order to determine the crystalline modification the morphologies of the Alq_3, the PTCDA and the PTCDA/Alq_3 multilayer films were investigated by x-Ray diffraction (XRD). Due to the quasi-amorphous structure of Alq_3 no visible x-ray diffraction was observed in the Alq_3 films. The measured XRD curve of a 40 nm thick PTCDA films is shown in Figure 4.4 (a), which reveals a maximum at $2\theta = 27.75^{o}$ indicating that it is composed of PTCDA in α-phase. The obtained full width at half maximum (FWHM) 0.33 of the rocking curve of 0.01 degrees is comparable to previous investigations of thin PTCDA films on Si substrate [3,127] demonstrating the high structural quality of the PTCDA sample. The XRD curve measured on the PTCDA/Alq_3

multilayer shows a maximum at 2 θ = 27.65^{o} (Figure 4.4 (b)) and a broader α-PTCDA reflex with 0.44 ^{o} FWHM. The broadening of α-PTCDA reflex indicate inhomogeneous strain inside PTCDA crystallites and a small tilt of the PTCDA molecular planes with respect to normal of the substrate surface in agreement to previous investigations on PTCDA/Alq_3 multilayers [3,4]. The influence of the tilt of the molecular planes on the refractive index in the effective medium theory (EMT) multilayer will be discussed in section 4.6.3.

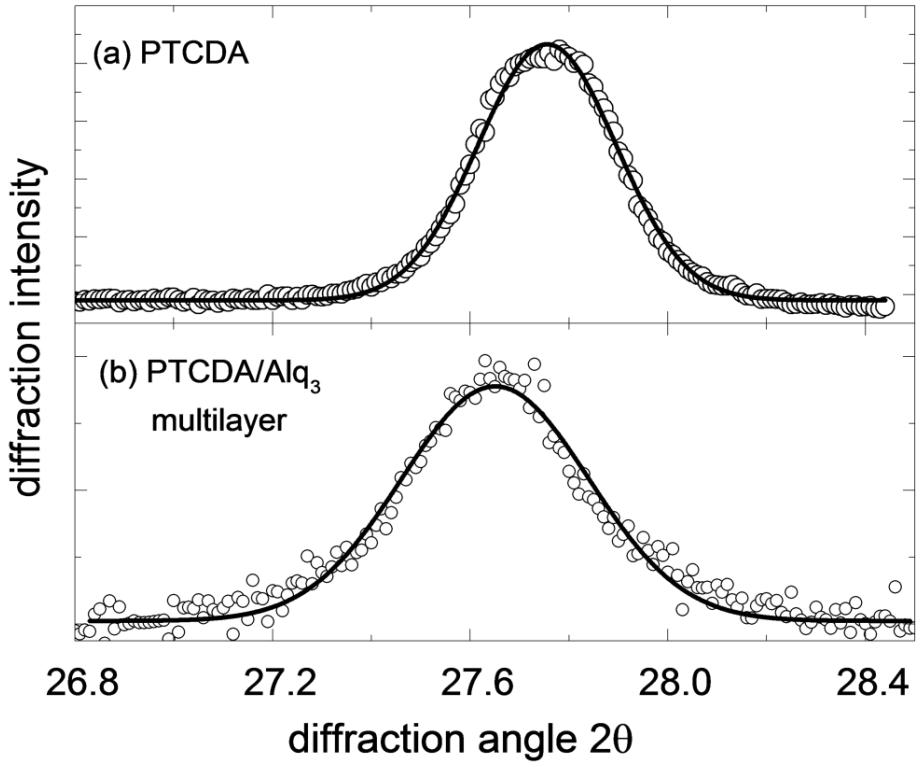

Figure 4.4: X ray diffraction spectra (a) on a 40 nm thick PTCA film and (b) on a 32×[6 nm PTCDA/22 nm Alq_3] multilayer film grown on Pyrex. The solid lines are the Gaussian fits.

4.5 Theoretical Modelling

4.5.1 Planar waveguide theory

The effective refractive index n_{eff} of the propagating mode in the waveguide is given by $n_{eff} = n_2 \sin\theta_m = n_p \sin\theta_p$. n_2 is the refractive index of the film, n_p is the refractive index of the coupling prism. θ_p is the angle of the beam with respect to the normal to the prism base (see Fig. 4.3) and θ_m is the synchronous angle of reflection at the air/film interface with respect to the x axis of the guided mode with mode index *m*. The $n_{eff}(\theta_m)$ value can be determined by measuring the angle $n_{eff}(\theta_i^{(m)})$ at each *m*-line with

$$n_{eff}(\theta_m) = n_p \sin\left[\alpha + \arcsin\left(\frac{\sin\theta_i^{(m)}}{n_p}\right)\right]. \tag{4.1}$$

α is the base angle of the prism (45^0). In Eq.(4.1), the extraordinary refractive index (n_p^e), or the ordinary refractive index (n_p^o) of Rutile[128] were used in the calculation for TE and TM modes, respectively.

The optical energy couples into a waveguide mode when the waveguide mode satisfies the relation[129]

$$2kn_2 t\cos\theta_m - 2\phi_{23} - 2\phi_{21} = 2m\pi \tag{4.2}$$

where m = 0, 1, 2,…. is the order of the waveguide mode, t is the thickness of the film and ϕ_{21} and ϕ_{23} are the phase changes due to the total internal reflection at the air/film and at the film/substrate interface, respectively[130]. From Eq. (4.2), the thickness of the waveguide t as a function of n_{eff} for an isotropic waveguide medium (like Alq_3) with $n_2 = n_{2x} = n_{2y} = n_{2z}$ (where x, y, z denotes the coordinate directions as introduced in Fig. 4.3) can be derived and is given by

$$t(n_{eff}) = \frac{\lambda\left[m\pi + \tan^{-1}\left[r_1\left(\frac{n_{eff}^2 - n_3^2}{n_2^2 - n_{eff}^2}\right)^{1/2}\right] + \tan^{-1}\left[r_2\left(\frac{n_{eff}^2 - n_1^2}{n_2^2 - n_{eff}^2}\right)^{1/2}\right]\right]}{2\pi\left(n_2^2 - n_{eff}^2\right)^{1/2}}. \tag{4.3}$$

The coefficients r_1 , r_2 are 1 for TE modes and $r_1 = n_2^2 / n_1^2$ and $r_2 = n_2^2 / n_3^2$ for TM modes. n_1, n_2 and n_3 are the indices of refraction of air, the film (waveguide) and of the Pyrex substrate, respectively. If a birefringent waveguide medium with $n_{2x} \neq n_{2y} = n_{2z}$ like PTCDA is used Eq. (4.3) is the same for TE modes but needs to be modified for TM modes [131] to

$$t_{TM}(n_{eff}) = \frac{\lambda\left[m\pi + \tan^{-1}\left[r_{1z}\left(\frac{n_{eff}^2 - n_3^2}{n_{2x}^2 - n_{eff}^2}\right)^{1/2}\frac{1}{\xi}\right]\tan^{-1}\left[r_{2z}\left(\frac{n_{eff}^2 - n_1^2}{n_{2x}^2 - n_{eff}^2}\right)^{1/2}\frac{1}{\xi}\right]\right]}{2\pi\left(n_{2x}^2 - n_{eff}^2\right)^{1/2}\xi}. \tag{4.4}$$

Where $r_{1z} = n_{2z}^2 / n_1^2$, $r_2 = n_{2z}^2 / n_3^2$ and $\xi = n_{2z} / n_{2x}$ is the anisotropy ratio of the birefringent material.

With the calculated effective refractive indices $n_{eff}(\theta_m)$ from Eq. (4.1), the bulk refractive index n_2 (or $n_{2x} \neq n_{2y} = n_{2z}$) and the thickness t of the film can be determined by a numerical fit to the experimental data with the calculated values of Eq. (4.3) (or Eq. (4.4)). The fitted bulk refractive

index $n_{2y=}\, n_{2z}$ for TE modes is equivalent to the bulk in-plane refractive index $n_{//}$ and for TM modes n_{2x} is equivalent to the normal refractive index $n_{\perp}$. To check the validity of the determined waveguide thickness it was compared with the thickness value measured with a profilometer close to the position of the coupling prism.

4.5.2 Effective medium approximation

If the repetition period of alternating PTCDA and Alq_3 layers in the multilayer waveguide is very small compared to the incident light wavelength, the multilayer stack can be treated as an effective medium. The effective in-plane and normal dielectric permittivity components of the layered structure is given by [132],

$$\varepsilon_{in\,plane} = \varepsilon_y = \varepsilon_z = f_1\varepsilon_{1,\parallel} + f_2\varepsilon_{2,\parallel} \tag{4.5}$$

$$\varepsilon_{normal} = \varepsilon_x = \frac{\varepsilon_{1,\perp}\varepsilon_{2,\perp}}{f_2\varepsilon_{1,\perp} + f_1\varepsilon_{2,\perp}} \tag{4.6}$$

where ε_1 and ε_2 refer to the permittivities of Alq_3 and PTCDA, f_1 and f_2 are the filling fraction factors of Alq_3 and PTCDA, respectively, with $f_2 = 1 - f_1$. Therefore Eq. (4.3) is also valid for an effective medium waveguide were n_2 represents the bulk in-plane refractive index $n_{//} = \sqrt{\varepsilon_{in\,plane}}$ for TE excitation and n_2 is equivalent to the normal refractive index $n_{\perp} = \sqrt{\varepsilon_{normal}}$ for TM excitation.

4.6 Experimental results and discussion

The incident angles $\theta_i^{(m)}$ for each corresponding mode of order *m* for both the TE and the TM modes for waveguides P_1, P_2, A_1 and M_1 were measured using the *m*-line technique as described in Section 4.3. The effective refractive indices n_{eff} (θ_m) as a function of the measured incident angle $\theta_i^{(m)}$ were determined using Eq.(4.1) for the experimentally observed guided modes. The error in $\theta_i^{(m)}$ was 0.5^0 resulting in an experimental error of $\Delta n_{eff} \approx 0.006$. The bulk refractive index n_2 and the film thickness *t* were fitted with Eq.(4.3) as described in Section 4.5. The bulk in-plane $n_{//}$ and normal refractive index $n_\perp$ was determined from the measured $\theta_i^{(m)}$ values of guided TE and TM modes respectively.

4.6.1 Pure PTCDA waveguide

The thicknesses of the pure PTCDA waveguides P_1 and P_2 were measured with a profilometer to be 1.00±0.05 μm and 0.45±0.02 μm, respectively, close to the area where the *m*-line measurements were performed. From the *m*-line measurements the effective refractive indices n_{eff} (θ_m) were retrieved with Eq. (4.1) and then inserted into Eq. (4.3), where the thickness and the bulk refractive index n_{2y}, n_{2x} ($n_{//}$ or $n_\perp$ for TE and TM polarized light, respectively) was varied until an optimum fit with the experimental data was achieved. In the calculations the refractive indices n_1 and n_3 were set to $n_1 = 1$ (for air) and $n_3 = 1.47$ (for the Pyrex® substrate). In Figure 4.5 the experimentally observed $n_{eff}(\theta_m)$ values for waveguide P_1 at an excitation wavelength of λ = 794 nm are represented by solid red circles for guided TE and solid blue

squares for TM modes, respectively. The solid and the dashed black curves show the calculated dispersion curves n_{eff} (t) versus thickness obtained from Eq. (4.3) (or Eq. (4.3)) for TE and TM modes, respectively, which optimally agree with the experimental data for the parallel index $n_{//}$ = 2.163 and the normal refractive index $n_{\perp}$ = 1.560. The fitted waveguide thickness in the area where the m-line measurements were carried out results in 1.02 μm, which agrees well with the measured value of ~1.0 μm. The experimental errors $\Delta n_{eff} \approx 0.006$ and of the fitted waveguide

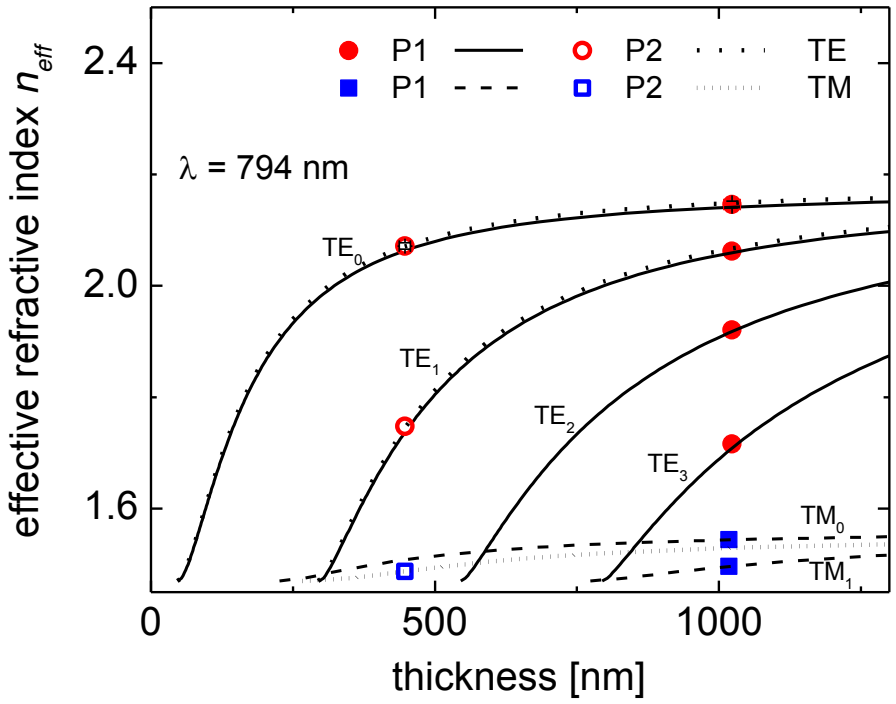

Figure 4.5: Observed effective refractive indices n_{eff} of TE modes in waveguide P_1 (solid red circles) and P_2 (open red circles) are shown at the wavelength 794 nm. Observed n_{eff} of TM modes in waveguide P_1 (solid blue squares) and P_2 (open blue squares) are also shown. Solid (TE modes) and dashed (TM modes) lines represent the calculated n_{eff} curves as a function of waveguide thickness using Eq. (4.3) for waveguide P_1. Dotted (TE modes) and short dotted curves (TM mode) represent the calculated n_{eff} curves as a function of waveguide thickness for P_2 waveguide.

thickness Δt ~15 nm are representatively given as error bars at the data points n_{eff} for TM_0 and TE_0 modes. The experimental data points $n_{eff}(\theta_m)$ of waveguide P_2 are represented by open red circles for TE and by open blue squares for TM modes, respectively. The bulk in-plane refractive index is found to be $n_{//} = 2.172$ and the thickness is found to be 0.447 μm which agrees with the measured thickness of 0.45 μm. Since only one TM mode was observed at the wavelength λ= 794 nm in the waveguide P_2, the $n_{\perp} = 1.542$ value was obtained with Eq. (4.4) by using the film thickness obtained from fits of the TE modes. Dotted black curves show the calculated dispersion curves $n_{eff}(t)$ versus thickness for TE modes using Eq. (4.3) which match with the experimental data for the bulk $n_{//}$ refractive indices. The curves $n_{eff}(t)$ of waveguide P_1 have slightly lower values compared to sample P_2.We attribute this difference to an increased density of crystal grains in the thicker waveguide P_1 (~1 μm thick) compared to waveguide P_2 (~ half the thickness of P_1). The higher density of crystal gains leads to a higher average PTCDA molecule distances in the area of grain contacts thus slightly lowering bulk $n_{//}$ refractive index in waveguide P_1. The calculated dispersion curve $n_{eff}(t)$ (using Eq. (4.4) versus thickness for TM modes is represented by a short dotted black line which matches with the experimental data for the $n_{\perp}$ refractive indices in waveguide P_2.

The bulk refractive indices $n_{//}$ and $n_{\perp}$ for the other wavelengths were determined in the same way. The measured in plane refractive indices $n_{//}$ are shown in Figure 4.6 as full red circles for waveguide P_1 and open black circles for waveguide P_2. The normal refractive indices $n_{\perp}$ are shown as solid blue (waveguide P_1) and open blue squares (waveguide P_2). The waveguide thicknesses which were obtained from fitting the experimental $n_{eff}(\theta_m)$ values with the $n_{eff}(t)$ curves for TE modes at different wavelengths were averaged for waveguides P_1 and P_2 separately

and found to be 1.02 ± 0.02 µm and 0.45 ± 0.02 µm, respectively. The good agreement of these values with the thickness values obtained with the profilometer in the area where the m-line measurements were performed substantiates the high accuracy of this technique. At wavelengths larger than 662 nm only one TM mode was observed in P_2 waveguide. In these cases, the $n_\perp$ values were calculated with Eq.(4.3) by setting the film thicknesses equal to the averaged values

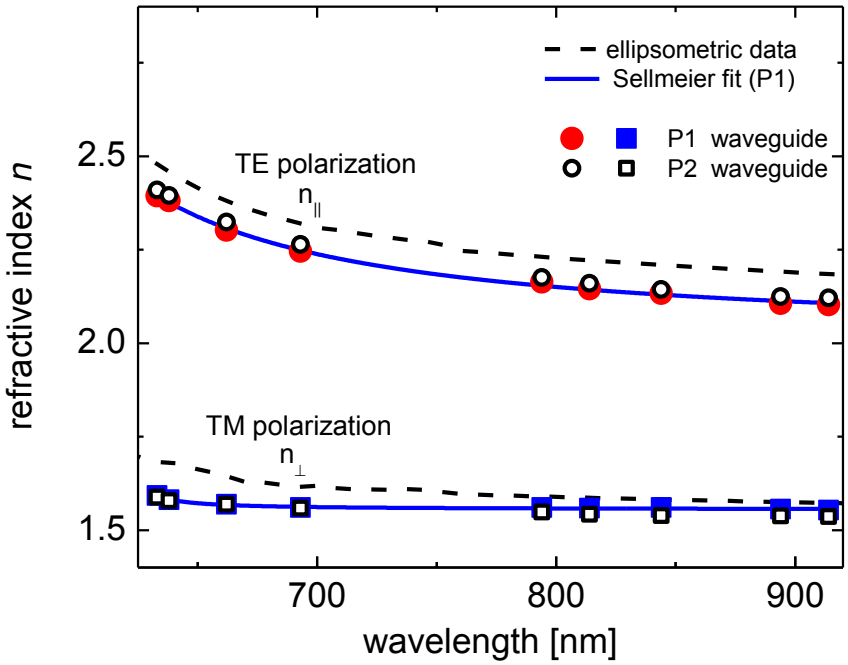

Figure 4.6: Measured bulk in-plane $n_{//}$ for pure PTCDA waveguides P_1 (solid red circles) and P_2 (open black circles) and normal refractive indices $n_\perp$ for P_1 (solid blue squares) and P_2 (open black squares). The solid blue lines represents the fitted curves with Eq. (4.7) and the black dash lines represent the measured refractive index dispersion by spectroscopic ellipsometry [98]

obtained from fits of TE (and TM modes at smaller wavelengths). The dispersion of the

measured $n_{//}$ and $n_{\perp}$ refractive indices was fitted by a Sellmeier equation with parameters A, B and C (λ in μm),

$$n^2 = A + B/(\lambda^2 - C)\,. \tag{4.7}$$

The solid blue lines in Figure 4.6 are the refractive index dispersion curves $n_{//}(\lambda)$ and $n_{\perp}(\lambda)$ for waveguide P_1 fitted with Eq. (4.7). The parameters A, B and C are summarized in Table 4.1.

Table 4.1: Parameters A, B and C obtained from fitting the Sellmeier equation (λ in μm) with the experimentally determined bulk in-plane $n_{\parallel}$ and normal $n_{\perp}$ refractive index values of the PTCDA waveguide film (P_1).

	A	B	C
$n_{\parallel}$	4.111	0.179	0.290
$n_{\perp}$	2.419	0.002	0.382

Similarly, the measured refractive indices $n_{//}$ and $n_{\perp}$ of waveguide P_2 were fitted with slightly different parameters A, B and C as shown in Table 4.2. The obtained parameters are in good agreement to earlier investigations using the *m*-line technique [107]. The measured refractive indices $n_{//}$ are ~3% lower compared to values obtained from a 25 nm thin PTCDA film on Si substrate by spectroscopic ellipsometry [98] (black dashed curves Figure 4.6). The lower $n_{//}$ values (red full circles) are attributed to a higher structural disorder and increased density of crystalline domains in the ~1 μm thick waveguide P_1 grown on Pyrex® substrate compared to the 25 nm thin PTCDA film deposited on Si. The higher density of grain boundaries leads to an increased average distance of PTCDA molecules and thus to a reduced refractive index in the PTCDA film. Waveguide P_2 with nearly half the thickness of waveguide P_1 shows slightly higher $n_{//}$

values (open black circles in Fig. 4.6) than in P_1. As mentioned earlier the slight increase of $n_{//}$ compared to P_1 might be attributed to the reduction of grain boundaries in this thinner waveguide.

Table 4.2: Parameters A, B and C obtained from fitting the Sellmeier equation (λ in μm) with the experimentally determined bulk in-plane $n_{\parallel}$ and normal $n_{\perp}$ refractive index values of the PTCDA waveguide film (P_2).

	A	B	C
$n_{\parallel}$	4.150	0.193	0.284
$n_{\perp}$	2.330	0.018	0.305

The obtained normal refractive index values $n_{\perp}$ agree reasonably with ellipsometric values obtained by Friedrich et al. [98] (dashed black line). Within the spectral range and particularly below $\lambda \approx 800$ nm our measured $n_{\perp}$ dispersion shows smaller values than in the dispersion found in spectrometric ellipsometry. This result again suggests an increasing average PTCDA molecule distance in the thick PTCDA films on Pyrex® compared to the 25 nm thin PTCDA film deposited on Si which was used in the ellipsometric investigations. The increasing deviation of the normal refractive index values $n_{\perp}$ with decreasing wavelength, which has also been observed for a 0.8 nm thick PTCDA sample in an earlier investigation [107], has been reproduced in this thesis again. The measured $n_{\perp}$ dispersion is therefore considered to be more reliable as the values obtained by ellipsometry.

4.6.2 Pure Alq_3 waveguide

The thickness of the pure Alq_3 waveguide A_1 was measured with the profilometer to be 2.20±0.10 μm. In Figure 4.7, the measured values $n_{eff}(\theta_m)$ of the experimentally observed TE and TM modes at the wavelength λ = 633 nm are represented by red solid circles and by blue solid squares, respectively. The dispersion curves $n_{eff}(t)$ versus waveguide thickness for various *m* modes were again obtained from Eq. (4.3) by fitting the bulk refractive index of Alq_3 to the data points $n_{eff}(\theta_m)$. The full and dashed black lines in Fig. 4.7 show the

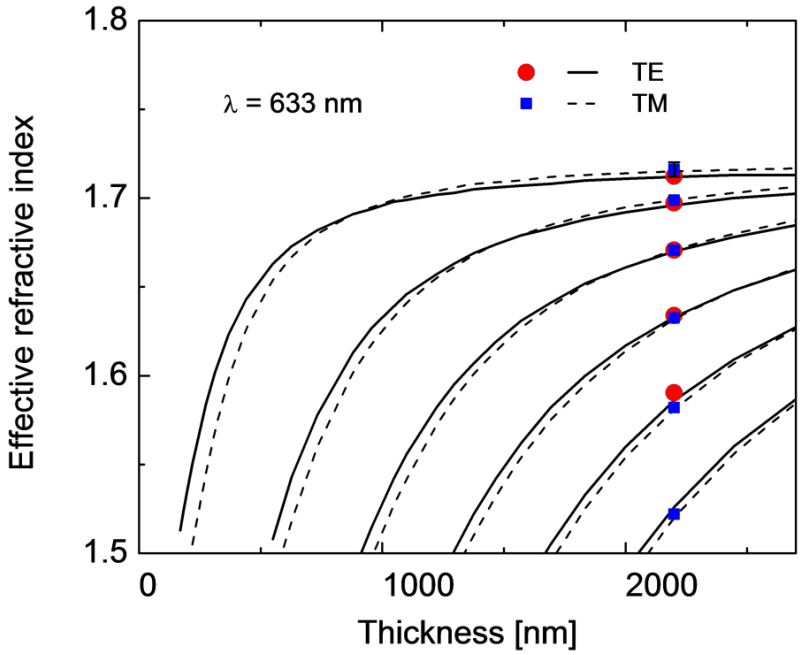

Figure 4.7: Observed effective refractive indices n_{eff} of TE modes (full red circles) and TM modes (full blue squares) in the Alq_3 waveguide A_1 are shown at the wavelength 633 nm. Solid (TE modes) and dashed (TM modes) lines represent the calculated n_{eff} curves as a function of waveguide thickness using Eq. (4.3)

calculated n_{eff} versus thickness curves.The experimental errors of n_{eff} and the fitted waveguide thickness are ~0.006 and ~15 nm, respectively, and indicated by error bars. Unexpectedly for an amorphously grown organic material we find a slight difference between the $n_{eff}(\theta_m)$ values of the TE and TM modes. This difference is smaller than the experimental error caused by the error in the measurement of the angles θ_m. In the case that the observed birefringence is not caused by the experimental uncertainty of the refractive index of the Rutile prism we propose that the observed weak birefringence of the bulk refractive index $n_{//}$ and $n_{\perp}$ might be caused by the polycrystalline (quasi-amorphous) island growth [95] with few nanometer sized Alq_3 crystal grains. As shown in AFM and SEM images (see Figure 2.4 and Figure 2.5 in Chapter 2) these islands have diameters of ~50 nm and heights of ~10 nm leading to a slightly different molecular order within the island plane area as along the vertically stacked island direction[133].

The wavelength dispersion curves of the bulk in-plane refractive index $n_{//}(\lambda)$ and normal refractive index $n_{\perp}(\lambda)$ were evaluated as described in Section 4.5. Measured values for $n_{//}$ and $n_{\perp}$ are presented in Figure 4.8 as full red circles and full blue squares, respectively. Open black triangles represent average refractive indices (n_{avg}) of $n_{//}$ and $n_{\perp}$. The wavelength dispersion of $n_{//}$ and $n_{\perp}$ as well as of the average refractive index $n_{ave} = (n_{||} + n_{\perp})/2$ (solid black line in Fig. 4.8) were fitted using Eq. (4.7) with the parameters A, B and C (λ in μm) listed in Table 4.3. Our evaluated data compare well with the values obtained with the spectroscopic ellipsometry (black dashed line[112]). The average thickness of the Alq_3

waveguide obtained by fitting the thicknesses in all the measurements is found to be 2.22 ±0.05 μm, which is in good agreement with the thickness measured with profilometer.

Table 4.3: Parameters A, B and C obtained from fitting the Sellmeier equation (λ in μm) with the experimentally determined bulk in-plane $n_{\parallel}$, bulk normal $n_{\perp}$ and the average of $n_{\parallel}$ and $n_{\perp}$ refractive index values of the Alq_3 waveguide film.

	A	B	C
$n_{\parallel}$	2.748	0.078	0.002
$n_{\perp}$	2.792	0.050	0.105
n_{avg}	2.773	0.061	0.063

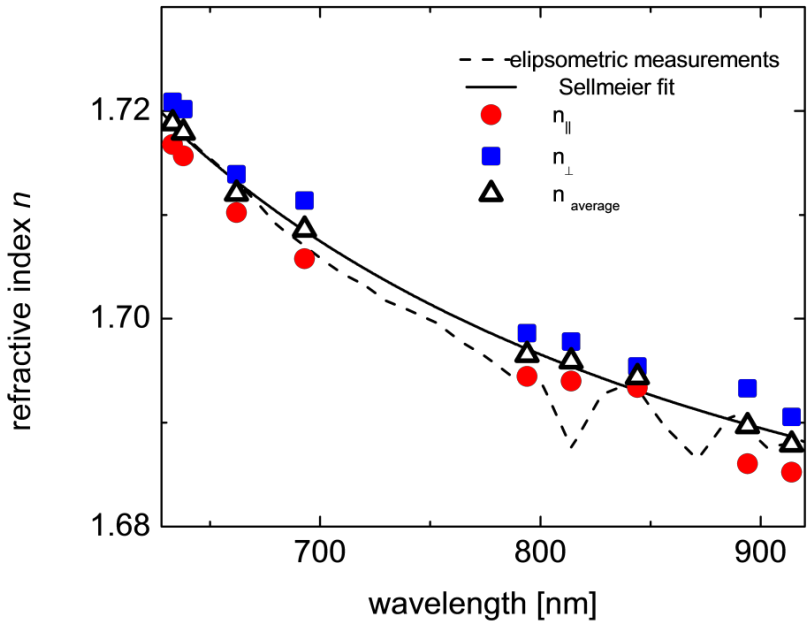

Figure 4.8: Measured bulk in-plane $n_{//}$ (full red circles) and normal refractive indices $n_{\perp}$ (full blue squares) for pure Alq_3 films A_1. The open triangles represent the average value of refractive indices $n_{//}$ and $n_{\perp}$. The solid black line represents the fitted curves using Eq. (4.7) and the black dash line[112] shows the measured refractive index dispersion with spectroscopic ellipsometry.

4.6.3 PTCDA/Alq_3 multilayer waveguide

We fabricated a waveguide M_1 composed of alternating PTCDA and Alq_3 multilayers in order to investigate the ability to control the dispersion and the birefringence of the composite materials. The sequence of the layers had a nominal period of 35 nm; it is thus much smaller than the wavelength of the incident light. With the profilometer a total thickness of waveguide M_1 was measured to be 0.90±0.05 μm at the area where the *m*-line measurements were carried out which is ~20 % less than expected from the growth rates. We attribute the smaller total thickness of the PTCDA/Alq_3 multilayer waveguide to a reduced sticking coefficient of the PTCDA molecules on the rough Alq_3 layer [133] during the OMBD growth. The bulk in-plane index $n_{//}$ and the normal refractive index $n_{\perp}$ of the M_1 waveguide and its thickness were obtained by fitting the $n_{eff}(\theta_m)$ values from the *m*-line measurements as described in Section 4.3. The experimentally obtained data points $n_{//}$ and $n_{\perp}$ for waveguide M_1 were plotted versus wavelength (see Figure 4.9) as black diamonds and green stars, respectively. The average thickness from all TE fits (with Eq.(4.3) is found to be 0.87±0.01 μm which agrees well with the measured thickness using the profilometer. With the measured values $n_{//}$ and $n_{\perp}$ the filling factors of Alq_3 (f_1) and PTCDA ($f_2 = 1 - f_1$) were determined for each wavelength used in the measurements (with eq. (4.5) and eq.(4.6)). We found that applying Eq. (4.5) to all data points for TE polarized excitation leads to an averaged value for the filling factor of f_1 = 0.766, whereas using Eq. (4.6) for TM polarized excitation leads to the higher filling factor of f_1 = 0.791. This difference can be attributed to a distortion in the

growth direction of the PTCDA molecular stacks (with respect to the waveguide x-axis) on the rough Alq_3 layers.

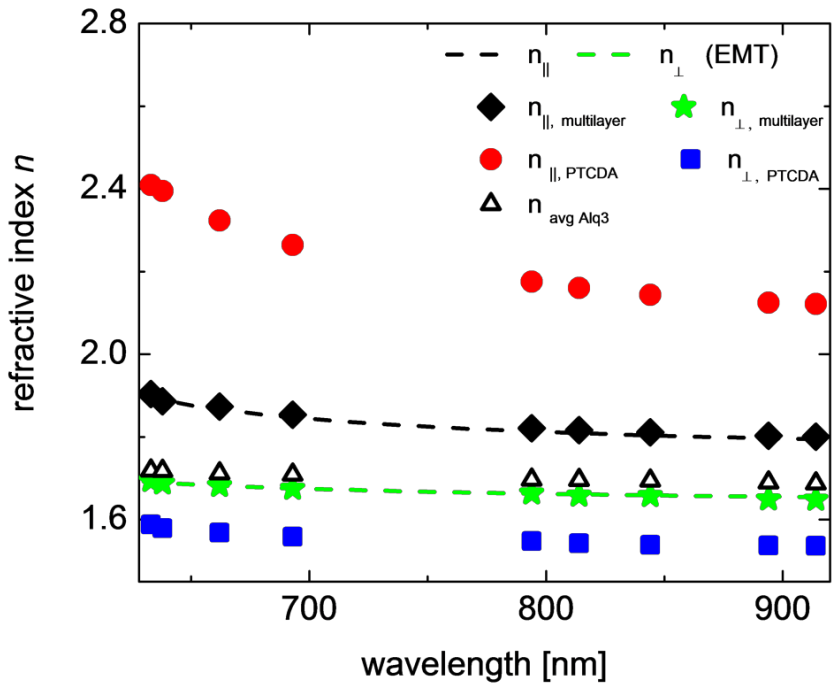

Figure 4.9: Measured bulk in-plane $n_{//}$ (black diamonds) and bulk normal refractive indices $n_{\perp}$ (green stars) for PTCDA/Alq_3 multilayer waveguide M_1. The dashed black and green lines represent the fitted curves with Eq. (4.7). For comparison $n_{//}$ and $n_{\perp}$ of pure PTCDA and $n_{ave,}$ of Alq_3 are shown as red circles, blue squares and with open black triangles, respectively.

Hence the PTCDA molecules are no longer perfectly parallel to the substrate, but slightly tilted at an average angle θ. We consider the average tilt angle by using the projections of the dielectric constants $\varepsilon_{2//}$ and $\varepsilon_{2,\perp}$ for PTCDA onto the TE and the TM polarization leading to

$$\varepsilon_{2,TE} = \frac{1}{2}\left(\varepsilon_{2,\|} + \left(\varepsilon_{2,\|}\cos(\theta) + \varepsilon_{2,\perp}\sin(\theta)\right)\right)$$

$$\varepsilon_{2,TM} = \varepsilon_{2,\|}\sin(\theta) + \varepsilon_{2,\perp}\cos(\theta) \tag{4.8}$$

Substituting these expressions in Eqs. (4.5) and (4.6) results in two equations with the two unknown values f_1 and θ. For the measured refractive indices $n_{//}$ and $n_\perp$ at nine different wavelengths, we found an average tilt angle of $\theta = 0.0085 \pm 0.0055$ in radians or $\theta = 0.5° \pm 0.3°$ and an average filling factor of $f_1 = 0.778 \pm 0.018$.

The wavelength dispersion curves $n_{//}$ (λ) and $n_\perp$ (λ) can now be projected with the Sellmeier equations for pure PTCDA and pure Alq_3 and the filling factor f_1:

$$n_\|^2 = f_1\,\varepsilon_1 + (1-f_1)\varepsilon_{2,TE}$$

$$n_\perp^2 = \frac{\varepsilon_{1\perp}\varepsilon_{2,TM}}{(1-f_1)\varepsilon_1 + f_1\varepsilon_{2,TM}} \tag{4.9}$$

with $\varepsilon_1 = \left(A^{Alq_3} + B^{Alq_3}/\left(\lambda^2 - C^{Alq_3}\right)\right)$.

$$\varepsilon_{2,TE} = \frac{1}{2}\left(A_\|^{\mathrm{PTCDA}} + B_\|^{\mathrm{PTCDA}}/\left(\lambda^2 - C_\|^{\mathrm{PTCDA}}\right)\right)(1+\cos(\theta)) + \frac{1}{2}\left(A_\perp^{PTCDA} + B_\perp^{PTCDA}/\left(\lambda^2 - C_\perp^{PTCDA}\right)\right)\sin(\theta)$$

$$\varepsilon_{2,TM} = \left(A_\perp^{PTCDA} + B_\perp^{PTCDA}/\left(\lambda^2 - C_\perp^{PTCDA}\right)\right)\cos(\theta) + \left(A_\|^{\mathrm{PTCDA}} + B_\|^{\mathrm{PTCDA}}/\left(\lambda^2 - C_\|^{\mathrm{PTCDA}}\right)\right)\sin(\theta)$$

The predicted dispersion curves agree with the experimental data without any additional parameter as demonstrated by the black and green dashed lines in Figure 4.9. The knowledge of the filling factor f_1 of Alq_3 allows to cross check the layer thicknesses of Alq_3 (t_1) and PTCDA (t_2) in the effective medium waveguide. It results in t_1 = 21.8 ± 0.5 nm using the relation $f_1 = N_1 t_1 / T$, where N_1 = 32 is the number of Alq_3 layers and where T is the total measured thickness of 0.90 μm. The layer thickness of PTCDA (t_2) was found to be 6.0 ± 0.5 nm using the relation $T = N_1 t_1 + N_2 t_2$, where N_2 = 33 is the number of PTCDA layers.

Chapter 5 Controlling guided modes in plasmonic metal/dielectric multilayer waveguides

5.1 Introduction

Coupling light into hybrid dielectric/metal nanostructures using the plasmon oscillations of a free-electron gas offers unprecedented control over light-matter interactions in deep sub-wavelength volumes. Possible applications of these plasmonic structures include long-range guiding of surface plasmon-polaritons (SPPs) below the diffraction limit [30–32] with bending of light around a corner [33] or beam splitting using T or Y shaped junctions [34,35]. Such novel plasmonic components could enable hybrid on-chip optical data communication between integrated electronic circuits.

To explore and improve the functionality of plasmonic systems, a wide variety of differently designed plasmonic heterostructures such as metal-air or metal-dielectric bilayers [31,36], dielectric-metal-dielectric (DMD) waveguides [30,37–39], metal-dielectric-metal (MDM) structures [40–44] as well as dual slab waveguide structures [32,45] have been (predominantly theoretically) investigated. Further studies also include waveguides containing discontinuous composite dielectric-metal island films [76–78] in which the transport of electromagnetic energy is based on near-field coupling between surface plasmon–polariton modes of adjacent metal

particles [134]. Such composite dielectric-metal island films allow to modify the complex dielectric constant as a function of the metal filling factor [135] and offer surface enhancement effects which can be used in various applications such as molecule or particle detection for biological sensor application [77,79,80].

Most of the above-mentioned investigations consider only one thin metal film or stripe which is deposited on or embedded between semi-infinite dielectric materials with same or different dielectric constant [136–138]. Several studies report on the insertion of additional dielectric nanolayers to achieve extended long-range plasmon waveguiding [139–143]. In this chapter, we experimentally study how guided transverse magnetic (TM) and electric (TE) modes are modified if few nanometer thin metallic films are embedded in finite size (~2 μm thick) organic aluminum-quinoline (Alq_3) waveguides. The hybrid plasmonic waveguides comprising nearly centered single composite Alq_3-$Mg_{0.9}$:$Ag_{0.1}$ metal-island layers or equally spaced metallic multilayers were fabricated by organic molecular beam deposition at ultralow vacuum (~10^{-8} mbar) on Pyrex® substrates. The plasmonic waveguide structures used for this study are illustarted in the Section 5.2. Aluminum-quinoline was selected since it is an appropriate material to fabricate high quality dielectric waveguides with low absorption losses at our investigation wavelength of 633 nm. In addition Alq_3/metal multilayers can be deposited with nanometer control without breaking the vacuum on many substrates, even on flexible ones like plastic films or on water soluble substrates. The alloy Mg:Ag was chosen since it has a low evaporation temperature reducing the penetration of the metal into the organic material during deposition. However, that the choice of Alq_3 and Mg:Ag has no significance on the generality of this investigations. Other organic or inorganic dielectric

cladding materials and metals could have been used to control the guiding properties of dielectric-plasmonic waves in a similar way.

In this chapter, the effective refractive indices n_{eff} of guided TM and TE modes were investigated as a function of the position(s) of the composite metal film(s) within the dielectric waveguide and of the thickness(es) [72,73]. The experimentally observed individually excited plasmonic, hybrid dielectric-plasmonic and dielectric waveguide modes which were measured using the *m*-line technique were presented in Section 5.5. The n_{eff} values of experimentally observed guided modes are compared with calculated values obtained from a multilayer waveguide model which is described in Section 5.4. The electric and magnetic field distributions of the guided modes, which were also calculated, are used to explain how the mode properties depend on the position of the composite metal film with respect to the field maxima (antinodes) or nodes. This investigation shows that metal films which are strategically placed in dielectric waveguides can be used to selectively excite and attenuate TM modes with plasmonic or dielectric character and to selectively suppress the coupling and guiding of specific dielectric TE modes.

5.2 Investigated waveguide structures

Pure Alq_3 and Alq_3/metal multilayer plasmonic films grown by OMBD [3,5,95,144] were used for this investigation. An alloy of 90% Mg and 10% Ag ($Mg_{0.9}$:$Ag_{0.1}$) was used for the metal layers. A 2.0±0.2 μm thick Alq_3 film with one centered Mg:Ag layer, nominal thickness of 8 nm (labeled as waveguide S_1) and two ~2.2±0.2 μm thick Alq_3 films each with one centered Mg:Ag layer of nominal thickness 10 nm and 15 nm (labelled as waveguides S_2 and S_3,

respectively) were used to study mode properties of plasmonic Alq_3 waveguides. In addition, a 2.0±0.2 µm thick stack of four Alq_3 layers, each having a thickness of 500 nm, and three embedded Mg:Ag layers with a nominal thickness of 10 nm each (labeled as waveguide T_1), was grown. A pure Alq_3 film of similar thickness (~2.2±0.2 µm) was used as the reference R. A schematic sketch of the pure as well as the designed waveguides with metal layers is shown in Figure 5.1. Deviations from the nominal total growth thicknesses of the deposited films were determined using a profilometer prior to the optical investigation and were considered in the data evaluation.

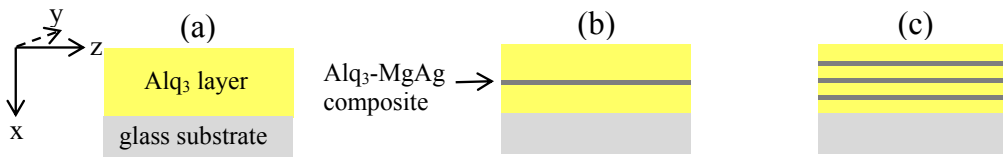

Figure 5.1: Schematic sketch of (a) the Alq_3 reference waveguide (R) (b) an Alq_3 waveguide with a single centered Alq_3-Mg:Ag composite metal layer (denoted as S_1, S_2, S_3 in the text) and (c) an Alq_3 waveguide with three equally spaced embedded Alq_3-Mg:Ag composite layers (denoted as waveguide T_1).

5.3 Existence of plasmonic modes in metal islandic films

Structural investigation on OMBD grown very thin Mg:Ag layers with nominal thicknesses of 5, 10 and 15 nm which were deposited on a 50 nm layer of Alq_3 reveals, Mg:Ag film deposits as an island structure with island diameters ranging from 40 to 90 nm as illustrated in Figure 2.6 in Chapter 2. The average height of the metal-islands in the three deposited films are found to be 4.8, 9.7 and 13.8 nm with a filling factor of 69±4%, 81±2%, 90±3%,

respectively. We assumed that the embeded Mg:Ag layers in investigated waveguides as illustarted in the above section which are nominally, 8, 10 and 15 nm in thickness have a similar filling factor corresponding to the metal thickness. Due to the high filling factor, most of the Mg:Ag islands are connected with adjacent islands. The link between adjacent metal islands constitutes a composite metallic Alq_3-Mg:Ag film in the waveguide. This suggests that coupled plasmonic modes predominantly propagate as a surface plasmon-polariton wave. Because of the relatively small amount of unconnected isolated metal islands, local plasmonic field effects are expected to play a subordinate role. Significant absorption loss enhancements or refractive index changes due to local plasmonic field effects would furthermore only be expected if the exciting He-Ne laser light energy is resonant with the surface plasmon energy of the metal islands. Recent electron energy loss spectroscopy (EELS) investigations on isolated $Mg_{0.9}$:$Ag_{0.1}$ clusters on Alq_3 coated InP nanowires [145] show a broad (~0.5 eV) surface plasmon resonance at ~3 eV thus only non-resonantly overlapping with the excitation energy of the He-Ne laser (~1.96 eV).

5.4 Theoretical Modelling

5.4.1 Multilayer model calculation

The effective refractive index n_{eff} for an experimentally observed guided modes using *m*-line technique, which is coupled at the synchronous angle θ_m, can be determined using Eq.(4.1) given in 4.5. In the calculations for the index of refraction of the prism n_p for TE and TM

modes, $n_p^e = 2.865$, the extraordinary refractive index, or $n_p^o = 2.584$, the ordinary refractive index of Rutile at 633 nm [146] was used, respectively.

An algorithm introduced by Schlereth et al. [147] describes in detail how the complex propagation constants $\tilde{\beta} = \beta_{re} + i\beta_{im}$ in z-direction (see Figure 4.3) and the electric field distributions of TE modes in a multilayer structure can be calculated from the known complex refractive indices $\tilde{n} = n_{re} + in_{im}$ of each layer. In the following we describe this method for TM modes: Assuming the layers are stacked downward in +x-direction (see Figure 4.3) and the general propagation direction of the wave is in z-direction, a TM polarised mode in the *jth* layer is described by

$$H_{y,j}(x) = \tilde{C}_j \exp(\tilde{K}_{x,j}(x - t_j)) + \tilde{D}_j \exp(-\tilde{K}_{x,j}(x - t_j)) \tag{5.1}$$

where $\tilde{C}_j$ and $\tilde{D}_j$ are the complex field amplitudes of $H_{y,j}(x) = \mu_j^{-1} B_{y,j}(x)$, $\tilde{K}_{x,j} = \sqrt{\tilde{\beta}^2 - k_0^2 \tilde{n}_j^2}$ is the complex propagation constant in - direction in the *jth* layer and k_0 is the wave number in vacuum. t_j is the location of the interface between layer *j* and *j+1*. At an interface the boundary conditions for the magnetic fields require

$$\begin{aligned} H_{y,j}(t_{j+1}) &= H_{y,j+1}(t_{j+1}) \\ \frac{\partial}{\partial x} H_{y,j}(t_{j+1}) &= \frac{n_j^2}{n_{j+1}^2} \frac{\partial}{\partial x} H_{y,j+1}(t_{j+1}) \end{aligned} \tag{5.2}$$

With $d_j = t_{j+1} - t_j$ as the thickness of the *jth* layer this leads to two equations for $\tilde{C}$ and $\tilde{D}$

$$\tilde{C}_j \exp(\tilde{K}_{x,j} d_j) + \tilde{D}_j \exp(-\tilde{K}_{x,j} d_j) = \tilde{C}_{j+1} + \tilde{D}_{j+1}$$
$$\tilde{C}_j \left(\frac{\tilde{K}_{x,j}}{\tilde{K}_{x,j+1}} \right) \left(\frac{\tilde{n}_{j+1}^2}{\tilde{n}_j^2} \right) \exp(\tilde{K}_{x,j} d_j) + \tilde{D}_j \left(\frac{\tilde{K}_{x,j}}{\tilde{K}_{x,j+1}} \right) \left(\frac{\tilde{n}_{j+1}^2}{\tilde{n}_j^2} \right) \exp(-\tilde{K}_{x,j} d_j) = \tilde{C}_{j+1} - \tilde{D}_{j+1} \quad (5.3)$$

which can be written in matrix notation as

$$\begin{bmatrix} \tilde{C} \\ \tilde{D} \end{bmatrix}_{j+1} = \tilde{\mathrm{T}}_j \cdot \begin{bmatrix} \tilde{C} \\ \tilde{D} \end{bmatrix}_j \quad (5.4)$$

Where $\tilde{\mathrm{T}}_j$ is a 2 x 2 matrix that depends on $\tilde{K}_{x,j}$ and $\tilde{K}_{x,j+1}$ and thus on the unknown $\tilde{\beta}$ and the known refractive indices $\tilde{n}_j$, $\tilde{\mathrm{T}}_j = \tilde{\mathrm{T}}_j(\tilde{\beta})$. Hence, the field amplitudes in the bottom layer *N* result from the ones in the top (first) layer *1* as follows:

$$\begin{bmatrix} \tilde{C} \\ \tilde{D} \end{bmatrix}_N = \tilde{\mathrm{T}}_{N-1} \cdot \tilde{\mathrm{T}}_{N-2} \cdot \ldots \cdot \tilde{\mathrm{T}}_1 \begin{bmatrix} \tilde{C} \\ \tilde{D} \end{bmatrix}_1 = \prod_{1}^{j=N-1} (\tilde{\mathrm{T}}_j) \begin{bmatrix} \tilde{C} \\ \tilde{D} \end{bmatrix}_1 = \tilde{\mathrm{T}}_{\mathrm{WG}} \begin{bmatrix} \tilde{C} \\ \tilde{D} \end{bmatrix}_1 \quad (5.5)$$

The field is evanescent in negative x-direction (upward) in layer 1 (air) and evanescent in positive x-direction (downward) in the bottom layer N (substrate), therefore Eq. (5.4) reduces to

$$\begin{bmatrix} 0 \\ \tilde{D} \end{bmatrix}_N = \tilde{\mathrm{T}}_{\mathrm{WG}} \begin{bmatrix} \tilde{C} \\ 0 \end{bmatrix}_1 = \begin{bmatrix} \tilde{t}_{11} & \tilde{t}_{12} \\ \tilde{t}_{21} & \tilde{t}_{22} \end{bmatrix} \begin{bmatrix} \tilde{C} \\ 0 \end{bmatrix}_1 \quad (5.6)$$

which leads to $\tilde{t}_{11}\tilde{C} = 0$ and –since $\tilde{C} \neq 0$– to $\tilde{t}_{11}(\tilde{\beta}) = 0$. The complex propagation constant $\tilde{\beta}$ that solves this equation can be found with a numerical method. The effective refractive indices n_{eff} of the propagating modes are given by $n_{eff} = \beta_{re} / k_0$ which can then be

compared to the experimentally measured refractive indices n_{eff} Eq.(4.1). In addition, the absorption coefficient $\alpha = 2\beta_{im}$ and the complex magnetic field distributions $H_y(x)$ can be calculated for the guided modes using Eq. (5.5) recursively. With Maxwell's equations the field distributions $E_z(x) = -\mathrm{i}\frac{1}{\omega\varepsilon\varepsilon_0}\frac{dH_y(x)}{dx}$ and $E_x(x) = -\frac{\beta}{\omega\varepsilon\varepsilon_0}H_y(x)$ [148] can also be derived. Similar equations analogous to (5.1) through (5.6) provide the dispersion curves and the complex field distributions $E_y(x)$, $H_z(x)$ and $H_x(x)$ for TE modes [147].

5.4.2 Effective medium theory (EMT) for composite films

The complex refractive index of the composite Alq_3-Mg:Ag island film was determined using effective medium theory (EMT). The effective dielectric permittivity (ε_e) of two dimensional composites is given by [135];

$$\varepsilon_e = \frac{1}{2}\{(2p-1)(\varepsilon_m - \varepsilon_d) \pm \sqrt{(2p-1)^2(\varepsilon_m - \varepsilon_d)^2 + 4\varepsilon_m\varepsilon_d}\} \tag{5.7}$$

where ε_m is the permittivity of the $Mg_{0.9}$:$Ag_{0.1}$ alloy, ε_d is the permittivity of the dielectric Alq_3 and p is the filling factor of the metal alloy. The sign in Eq. (5.7) needs to be chosen appropriately to result in a posive imaginary part of ε_e [135]. The complex permittivities of Mg and Ag (ε_{Mg} and ε_{Ag}) at 633 nm were calculated from their linear refractive indices $n_{Mg} = 0.48$ [149] and $n_{Ag} = 0.135$ [150] and their extinction coefficients $\kappa_{Mg} = 4.92$ [149] and

$\kappa_{Ag} = 3.99$ [150], respectively. The permittivity of the $Mg_{0.9}:Ag_{0.1}$ alloy was then determined according to $\varepsilon_m = 0.9\varepsilon_{Mg} + 0.1\varepsilon_{Ag} = -22.987 + i\,4341$. The permittivity of Alq_3, $\varepsilon_d = (n_{Alq_3})^2$ was calculated from its in-plane refractive index $n_{Alq_3} = 1.7168$ for TE polarization and from the out of-plane refractive index $n_{Alq_3} = 1.7208$ for TM polarization. The in-plane and out-of- plane refractive indices of Alq_3 were determined by *m*-line measurements on pure Alq_3 waveguides [6]. The slight birefringence of the Alq_3 film is attributed to polycrystalline (quasi-amorphous) layer growth [95] with few nanometer sized Alq_3 crystal grains. The complex refractive index of the composite Alq_3-$Mg_{0.9}:Ag_{0.1}$ island layer was finaly deduced from the real and imaginary part of the effective dielectric permittivity (ε_e) given in Eq. (5.7). The refractive indices of air and of the Pyrex substrate were taken as 1.00 and 1.47, respectively.

5.5 Experimental results and discussion

5.5.1 Guided modes in plasmonic Alq_3 waveguides with a single embedded metal layer

Guided TE and TM modes were studied in three Alq_3-Mg:Ag plasmonic waveguides labelled as S_1, S_2 and S_3, each with a single embedded Mg:Ag layer of a nominal thickness of 8, 10 or 15 nm near the center of the waveguide. The measured effective refractive indices n_{eff} of various TM modes for all three waveguides S_1, S_2 and S_3 are presented in Figure 5.2 as data points (red triangles, blue dots, orange squares). Vertical error bars representatively shown

for the TM_0 mode indicate an experimental error of n_{eff} of 0.35%. (Same errors are indicated

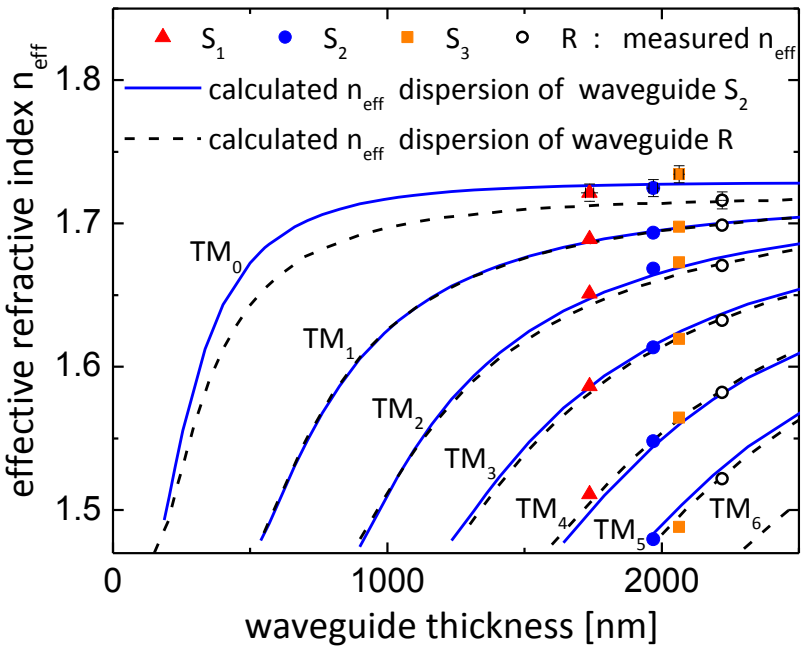

Figure 5.2: Experimentally observed effective refractive indices n_{eff} of guided TM modes in plasmonic Alq_3 waveguides S_1, S_2 and S_3 with a centered single Alq_3-Mg:Ag composite metal layer of 7, 9 and 13 nm thickness, respectively, and of the pure Alq_3 waveguide R. The solid and the dashed lines are the calculated n_{eff} dispersion curves of a plasmonic Alq_3 waveguide with a 9 nm thick centered single Alq_3-Mg:Ag composite metal layer and of reference waveguide R, respectively.

in Figure 5.6, Figure 5.6 and Figure 5.8). The total thicknesses of the waveguides S_1, S_2 and S_3 were measured to be 1.8, 2.0 and 2.0 µm, respectively, using a profilometer prior to the optical measurements which was ~10% less than nominally expected. The individual top and bottom Alq_3 layers as well as the effective thicknesses of the composite Alq_3-Mg:Ag metal layers were determined by fitting them to the measured effective refractive indices n_{eff} using the theoretical model as explained in Section 5.4. In this procedure, the individual layer

thicknesses were varied until optimum agreement between the experimentally observed and calculated effective refractive indices n_{eff} of all guided TM and TE modes was simultaneously reached. The obtained thicknesses of the bottom Alq_3 layers are in good agreement with the nominal values, while the fitted thicknesses of the top Alq_3 layers are ~15-20 % less than nominally expected. This is consistent with the lower values of the total thickness found by the profilometer measurements. We attribute the smaller thicknesses of the top Alq_3 layers to a reduced sticking coefficient of the Alq_3 molecules on the rough Mg:Ag islands film during the OMBD growth. The fitted effective thicknesses of the composite Alq_3-Mg:Ag island layers resulted in 7, 9 and 13 nm using filling factors of p = 0.7, 0.8 and 0.9 (as determined in section 2.4.2) for the waveguides S_1, S_2 and S_3, respectively. The individual Alq_3 layer and Alq_3-Mg:Ag film thicknesses of the waveguides S_1, S_2 and S_3, are summarized in Table 5.1.

Table 5.1: Fitted thicknesses of Alq_3-Mg:Ag composite metal layer, top and bottom layers of Alq_3 and total thickness compared with the measured total thicknesses of plasmonic waveguides S_1, S_2 and S_3 using a profilometer.

	S_1	**S_2**	**S_3**
Top Alq_3 layer (nm)	760	860	950
MgAg/ Alq_3 composite layer (nm)	7	9	13
Bottom Alq_3 layer (nm)	970	1100	1100
Total thickness from fitting (nm)	1737	1969	2063
Profilometer measured thickness (nm)	1800±90	2000 ±100	2000±100
Nominal total thickness (nm)	2008	2210	2215

Horizontal error bars in the data points in Figure 5.2 (as well as in Figure 5.4, Figure 5.6 and Figure 5.8) indicate an uncertainty of ~±15 nm in the waveguide thickness fit. The solid lines in Figure 5.2 show exemplarily the calculated n_{eff} dispersion (n_{eff} versus waveguide thickness) curves for different TM modes of the waveguide S_2 with a top–to-bottom Alq_3 cladding layer ratio of 0.781. This ratio was kept constant in the calculation while the total waveguide thickness (x-axis) was varied. The theoretical disperion cuves optimally match the experimentally observed effective refractive indices at a total thickness of 1969 nm. For clarity the n_{eff} versus thickness curves for waveguides S_1 and S_3 have been omitted in Figure 5.2, but the agreement is equally good using a top-to-bottom Alq_3 cladding layer ratio of 0.784 and 0.864 (see Table 5.1), respectively. (Calculated n_{eff} dispersion curves of waveguide S_3 can be found in ref. ([5])). The open circles and dashed lines in Figure 5.2 show the measured n_{eff} values and dispersion curves of the effective refractive indices for different TM modes of a pure Alq_3 waveguide R for comparison. The experimental and calculated results indicate a significantly increased effective refractive index n_{eff} for the TM_0 mode and a measurable increased n_{eff} for the TM_2 mode compared to the pure Alq_3 reference, S_2, which were not measurable effects within the experimental errors.

To explain the experimental results we calculated the magnetic field distributions $H_y(x)$ of the TM modes in the plasmonic Alq_3 waveguide as outlined in section 5.4. The squared magnetic field distributions $H_y(x)H_y^*(x)$ for waveguide S_2 are exemplarily displayed in Figure 5.3. For comparison, the calculated squared magnetic field distributions in the pure Alq_3 reference waveguide R are given as dashed lines. The graphs in Figure 5.3

demonstrate that the magnetic field distribution of the TM_0 mode has its antinode close to the position of the Alq_3-Mg:Ag composite layer, which leads to a symmetrically bound (s_b)

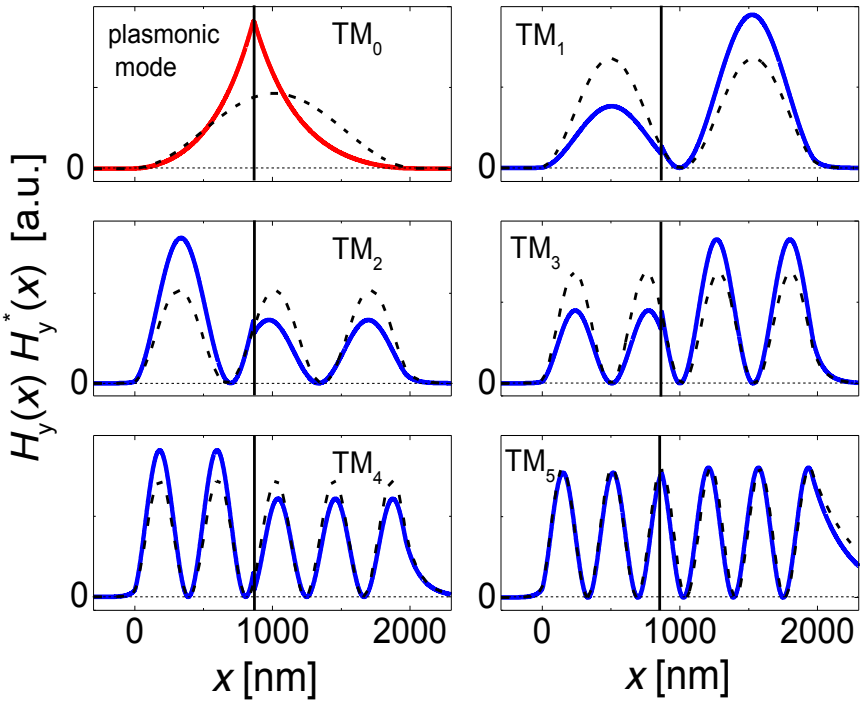

Figure 5.3: Calculated squared magnetic field distributions $H_y(x)H_y^*(x)$ of guided TM modes in the Alq_3 waveguide S_2 with a 9 nm thick single Alq_3-Mg:Ag composite metal layer. The vertical line indicates the position of the composite metal layer with respect to the air/Alq_3 interface at $x = 0$. Calculated squared field distributions of TM modes in a pure Alq_3 reference waveguide R are indicated as dashed lines.

plasmonic mode [137,138] and explains the increase of n_{eff} beyond the Alq_3 bulk refractive index. Theoretically[137,138] an anti-symmetrically bound TM_0 (a_b) plasmonic mode exists as well. It has a high refractive index of $n_{eff} = 6.17$ and an approximately three order of magnitude

stronger damping ($\alpha \approx 6\times10^5$ cm^{-1}) compared to the TM_0 s_b mode ($\alpha \approx 4\times10^2$ cm^{-1}).Since this antisymmetric high-index mode cannot be experimentally observed, the field distribution of this mode has not been included in Figure 5.3. The higher-order TM modes are hybrid dielectric-plasmonic modes with a varying degree of plasmonic characters. TM_2 and TM_3 modes possess an antinode close to the position of the composite metal layer which explains the observed increase of the effective refractive indices of these modes. In contrast, TM

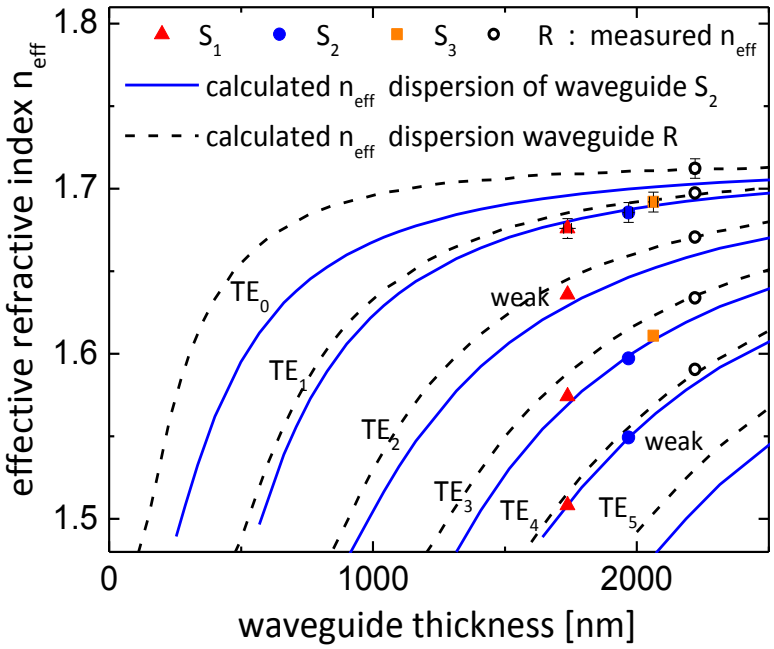

Figure 5.4: Experimentally observed effective refractive indices n_{eff} of guided TE modes in plasmonic Alq_3 waveguides S_1, S_2 and S_3 with a centered single Alq_3-Mg:Ag composite metal layer of 7, 9 and 13 nm thickness, respectively, and of the pure Alq_3 waveguide R. The solid and the dashed lines are the calculated n_{eff} dispersion curves of a plasmonic Alq_3 waveguide with a 9 nm thick centered single Alq_3-Mg:Ag composite metal layer and of reference waveguide R, respectively.

modes which have anti-nodes in the Alq_3 layers, like the TM_1 and TM_4 modes, show predominantly dielectric behaviour. The TM_5 mode has only one of its 6 antinodes at the Alq_3-Mg:Ag composite layer, which is not enough to acquire sufficient plasmonic character to shift the effective refractive index significantly.

The effect of the inserted Alq_3-Mg:Ag composite metal film on TE modes was investigated in a similar way. The measured refractive indices n_{eff} of the observed TE modes from all three single metal layer samples and of reference waveguide R can be seen in Figure 5.4 as data points. As before, the calculated dispersion curves of the refractive indices for the TE modes in a plasmonic Alq_3 waveguide with a single 9 nm metal layer (solid lines) and in a pure Alq_3 waveguide as reference R (dash lines) are shown for comparison. The calculations and the experiments show that -unlike the TM modes- the effective refractive indices of all modes, predominantly of even modes, are shifted to lower values by the embedded Alq_3-Mg:Ag composite layer compared to the reference sample. Experimentally, none of the three waveguides coupled to a TE_0 mode and the TE_2 and TE_4 modes were either weak or vanished with increasing thickness of the Alq_3-Mg:Ag composite layer.

These results can again be understood by analyzing the complex electric fields $E_y(x)$ which are plotted in Figure 5.5 as squared field distribution $E_y(x)E_y^*(x)$. The Alq_3-Mg:Ag composite layer suppresses the field distributions of all modes in either the top or the bottom layer due to partial reflection at the thin metallic film. The fields are pushed into the low index cladding layer, air or pyrex, which leads to a general shift to lower effective refractive indices n_{eff} for all modes. The TE_0, TE_2 and TE_4 modes have their “center of mass” in the

bottom Alq_3 layer which partially explains the experimentally observed weak coupling into the waveguide through the Alq_3-Mg:Ag composite layer. As will be discussed in section 5 the even modes TE_0, TE_2 and TE_4, which possess a high electric field near the location of the composite metallic film, are also strongly damped due to high resistivity losses. This explains the weak or missing coupling to these modes in our experiments. The modes which are coupled well, like the TE_1 and TE_3 modes, have field distributions which are centered in the

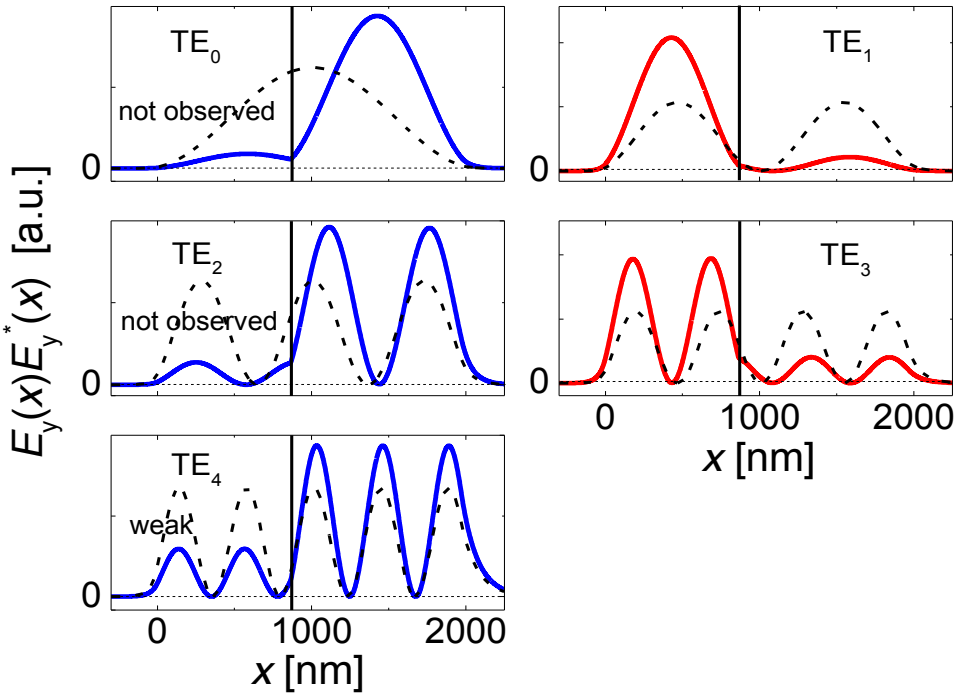

Figure 5.5: Calculated squared electric field distribution $E_y(x)E_y^*(x)$ of guided TE modes in the plasmonic Alq_3 waveguide S_2 with a 9 nm thick single Alq_3-Mg:Ag composite metal layer. The vertical line indicates the position of the composite metal layer with respect to the air/Alq_3 interface at $x = 0$. Calculated field distributions of TE modes in a pure Alq_3 reference waveguide R are indicated as dashed lines.

top Alq_3 layer and possess a node close to the position of the composite metallic film leading to reduced losses for these modes.

5.5.2 Guided modes in plasmonic Alq_3 waveguides with three embedded metal layers

To increase the plasmonic effects on guided TM and TE field distributions we fabricated a plasmonic Alq_3 waveguide with three equally spaced, 9 nm thick, embedded composite metal layers (sample T_1) which has a structure as sketched in Figure 5.1 (c). The measured refractive indices n_{eff} for TM modes are presented in Figure 5.6 as blue full circles, the fitted individual Alq_3 layer thicknesses are given in Table 5.2. For comparison the measured n_{eff} values of the reference waveguide R are given as open circles. As in the single composite metal layer waveguides (S_1 to S_3) the thicknesses of the Alq_3 films that were grown on the rough metal-island layer are reduced by ~17% compared to the bottom layer which was deposited on the glass substrate. The calculated refractive index dispersion curves for the plasmonic waveguide T_1 and of reference R are shown in Figure 5.6 as solid and dashed lines, respectively. Both the measurements and the calculations clearly indicate a significantly increased refractive index n_{eff} for the TM_0, TM_1 and TM_2 modes. Composite metal layer waveguides (S_1 to S_3) the thicknesses of the Alq_3 films that were grown on the rough metal-island layer are reduced by ~17% compared to the bottom layer which was deposited on the glass substrate. The calculated refractive index dispersion curves for the plasmonic waveguide T_1 and of reference R are shown in Figure 5.6 as solid and dashed lines, respectively. Both the measurements and the calculations clearly indicate a

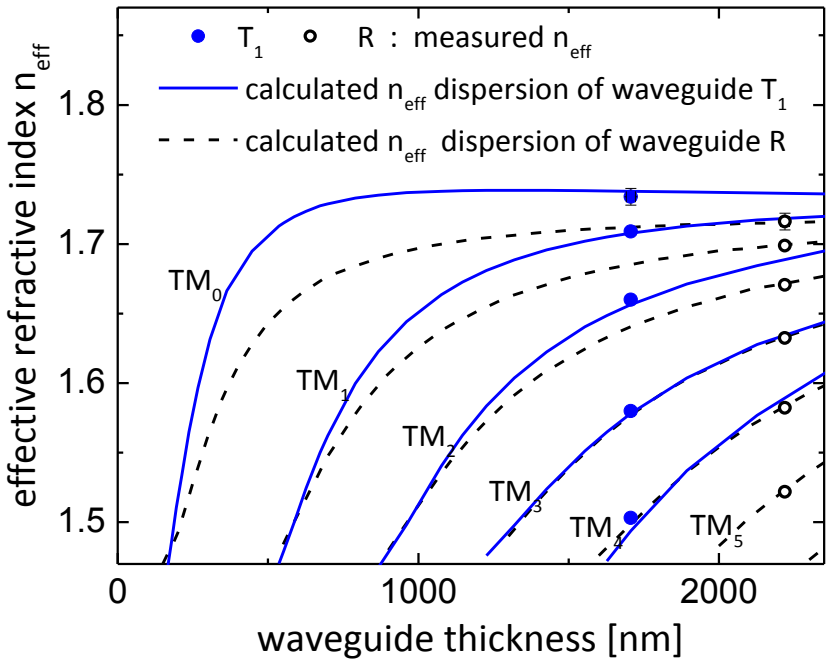

Figure 5.6: Experimentally observed effective refractive indices n_{eff} of guided TM modes in plasmonic Alq_3 waveguide T_1 with three equally spaced Alq_3-Mg:Ag composite metal layers of 9 nm thickness and of the pure Alq_3 waveguide R. The solid and the dashed lines are calculated n_{eff} dispersion curves of a plasmonic Alq_3 waveguide with three composite metal layers and of reference waveguide R, respectively.

significantly increased refractive index n_{eff} for the TM_0, TM_1 and TM_2 modes. The squared magnetic field distributions $H_y(x)H_y^*(x)$ shown in Figure 5.6 reveal that these modes have antinodes close to the locations of the Alq_3-Mg:Ag composite layers. They possess predominantly symmetrically bound (s_b) plasmonic character. As in the waveguides with a single metal layer (waveguides S_1 to S_3) this leads to higher refractive indices n_{eff}. Numerically we obtain for each of the symmetric TM_0, TM_1 and TM_2 s_b modes antisymetrically bound (a_b) plasmonic modes as well. They were not included in Figure 5.6.

Table 5.2: Fitted thicknesses of individual layers of individual Alq_3 and Alq_3-Mg:Ag composite metal layers and total thickness compared with the measured total thickness of plasmonic waveguide T_1 using a profilometer.

	Fitted layer thickness (nm)
1st Alq_3 layer	400
2nd Alq_3 layer	400
3rd Alq_3 layer	400
4th Alq_3 layer (bottom layer on glass substrate)	480
Each MgAg/ Alq_3 composite layer	9
Total thickness from fitting	1707
Measured thickness from profilometer	1700±85
Nominal total thickness	2030

The squared magnetic field distributions $H_y(x)H_y^*(x)$ shown in Figure 5.7 reveal that these modes have antinodes close to the locations of the Alq_3-Mg:Ag composite layers. They possess predominantly symmetrically bound (s_b) plasmonic character. As in the waveguides with a single metal layer (waveguides S_1 to S_3) this leads to higher refractive indices n_{eff}. Numerically I obtain for each of the symmetric TM_0, TM_1 and TM_2 s_b modes antisymetrically bound (a_b) plasmonic modes as well. They were not included in Figure 5.7 because these a_b modes have effective refractive indices of about $n_{eff} \approx 6.17$ and three orders of magnitude higher absorption coefficients ($\alpha \approx 6\times10^5$ cm^{-1}) than the symmetric plasmonic TM modes

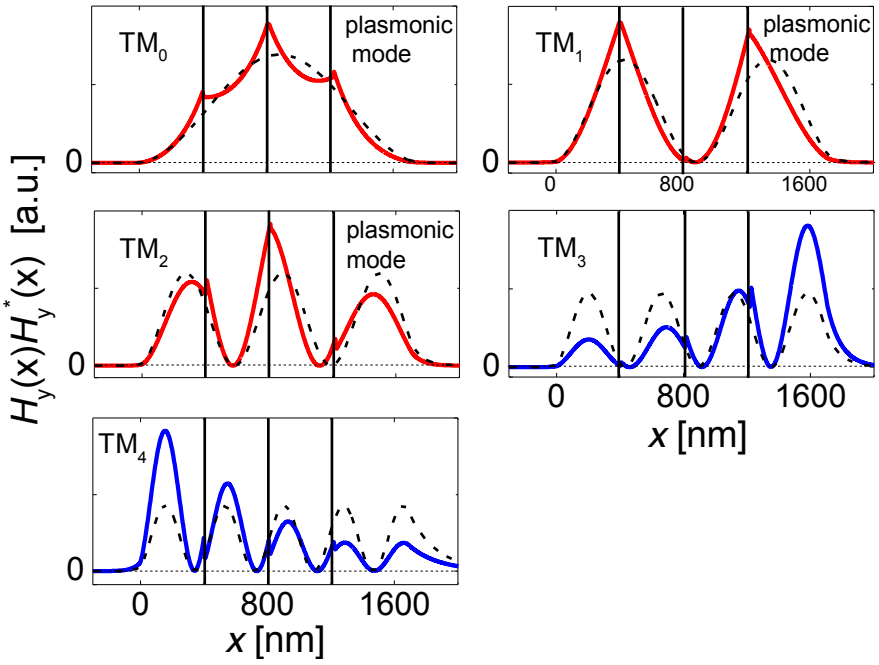

Figure 5.7: Calculated squared magnetic field distribution $H_y(x)H_y^*(x)$ of guided TM modes in plasmonic Alq_3 waveguide T_1 with equally spaced 9 nm thick Alq_3-Mg:Ag composite metal layers. The vertical lines indicate the positions of the composite metal layers with respect to the air/Alq_3 interface at $x = 0$. Calculated field distributions of TM modes in a pure Alq_3 reference waveguide R are indicated as dashed lines.

and thus were experimentally not observable. The TM_3 and TM_4 modes whose antinodes are mainly in the Alq_3 layers do not change their effective refractive indices compared to the reference waveguide R and possess a predominantly dielectric characters.

The TE modes are strongly affected by the insertion of the three Alq_3-Mg:Ag composite metallic layers. The calculated refractive index dispersion curves of the TE modes of sample T_1 are shown as solid curves in Figure 5.8 together with measured (open black circles) and calculated curves of the Alq_3 reference R (dashed curves) for comparison. Experimentally, we observed mode coupling only for the TE_3 mode (full blue circle).

Furthermore, the calculated effective refractive indices n_{eff} of all modes are significantly lower than in the reference waveguide.

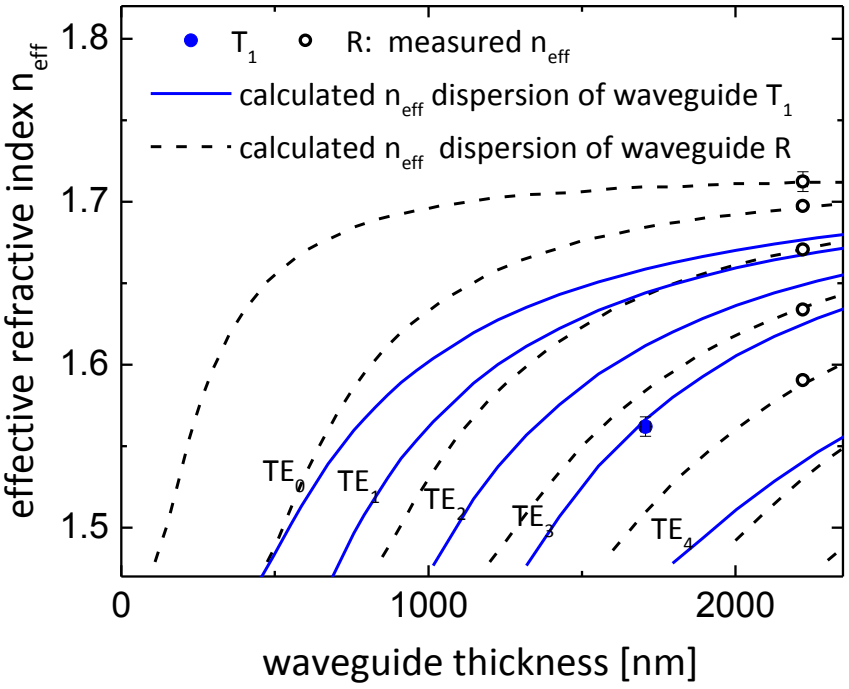

Figure 5.8: Experimentally observed effective refractive index n_{eff} of the guided TE_3 mode in plasmonic Alq_3 waveguide T_1 with three equally spaced Alq_3-Mg:Ag composite metal layers of 9 nm thickness and of the pure Alq_3 waveguide R. The solid and the dashed lines are calculated n_{eff} dispersion curves of a plasmonic Alq_3 waveguide with three composite metal layers and of reference waveguide R, respectively.

These findings can again be explained by the squared electric field distributions $E_y(x)E_y^*(x)$ for the TE modes which are depicted in Figure 5.9. Dashed lines represent squared field distributions of the pure Alq_3 reference R. The graphs demonstrate that the field distributions of TE_0, TE_1 and the TE_2 modes are strongly dampened by resistivity losses in

the composite metal preventing the coupling into these modes. In contrast, the TE_3 mode possesses nodes which are close to the location of the Alq_3-Mg:Ag composite layers, thus

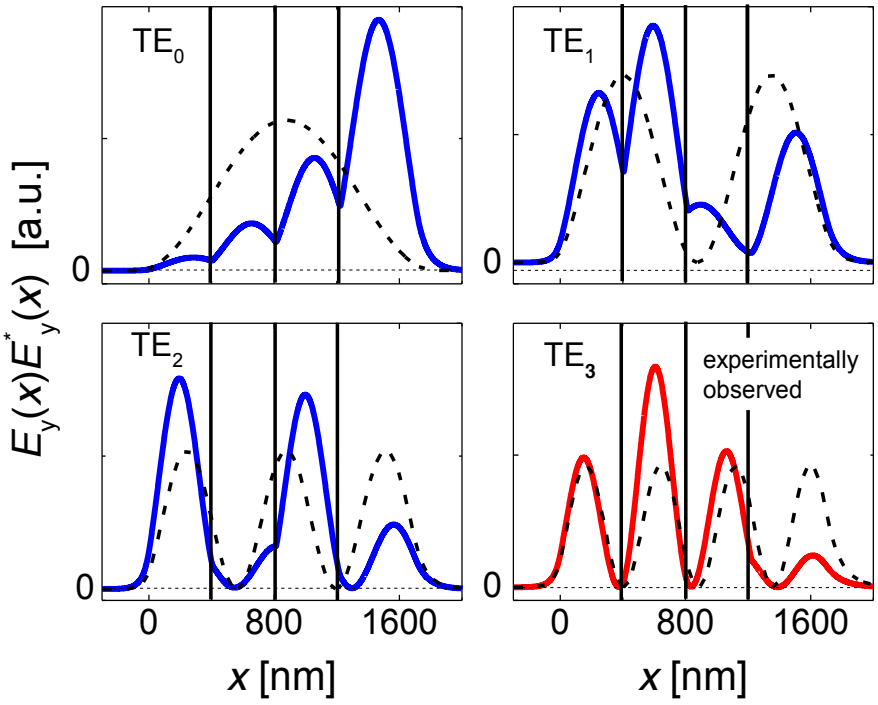

Figure 5.9: Calculated squared electric field distribution $E_y(x)E_y^*(x)$ of guided TE modes in plasmonic Alq_3 waveguide T_1 with equally spaced 9 nm thick Alq_3-Mg:Ag composite metal layers. The vertical lines indicate the positions of the composite metal layers with respect to the air/Alq_3 interface at $x = 0$. Calculated field distributions of TE modes in a pure Alq_3 reference waveguide R are indicated as dashed lines.

reducing absorption losses and enabling the coupling into this mode.

5.6 Properties of guided modes in a symmetric waveguide

The influence of the composite metal films as a function of its position is somewhat obscured in the investigated waveguides due to the fact that the top layer grew less thick than nominally expected. To make the effect of the inserted metal film more transparent we additionally present calculated effective refractive indices n_{eff} and absorption coefficients α of TM and TE modes for a more symmetric waveguide containing two 1100 nm Alq_3 cladding layers and one centered 13 nm thick composite metal film (p = 0.9, symmetric S_3). The dependence of n_{eff} for TM and TE modes as a function of their mode number is given in Figure 5.10 (a). For better comparison, the n_{eff} values of the plasmonic waveguide are divided

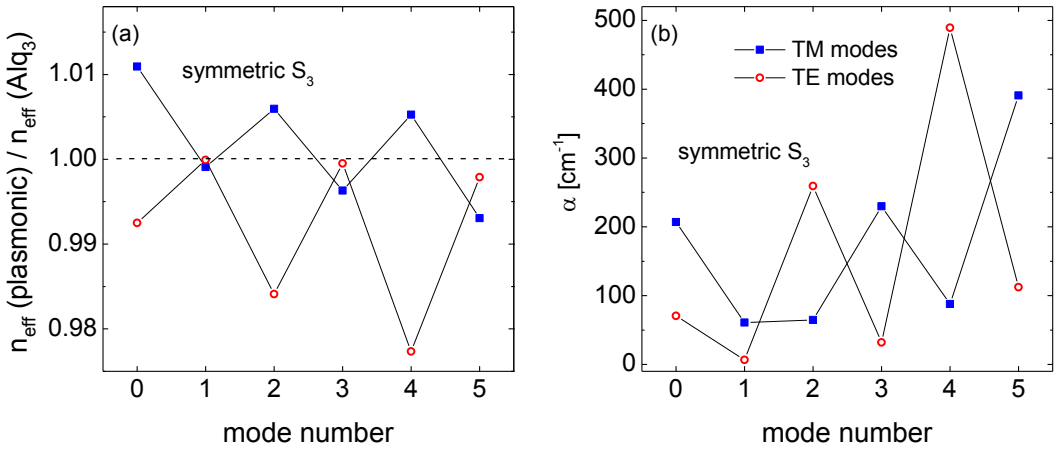

Figure 5.10: (a) Ratio of the calculated effective refractive indices of a symmetric waveguide S_3 with two 1100 nm Alq_3 cladding layers and a pure Alq_3 reference layer with 2.213 µm total thickness as a function of the mode numbers. (b) The calculated absorption constants of a symmetric waveguide S_3 with two 1100 nm Alq_3 cladding layers as a function of the mode numbers.

by the calculated values of the corresponding modes in a pure 2.213 μm thick Alq_3 reference waveguide. As described earlier, the n_{eff} values increase for even hybrid dielectric-plasmonic TM modes (antinode at the metal layer) while they remain nearly unchanged for odd TM modes (node at metal layer). For the TE polarization the insertion of a metallic layer leads to a local minimum in the electric field distribution at the position of the metallic film. The resulting field distribution of even TE modes thus becomes similar to the field distribution of the adjacent next higher odd TE mode explaining the reduction of the n_{eff} values for even TE modes. Odd TE modes, which have a node at the location of the inserted metal film, show nearly unchanged n_{eff} values. Figure 5.10 (b) shows the dependence of the absorption α for TM and TE modes as a function of the mode number. As mentioned before, even TE modes show a maximum of the electric field distribution at the position of the composite metal layer. Accordingly, the absorption losses are highest for these modes, while the losses are less for odd TE modes. Similar to surface scattering losses [129], the increase of the absorption for higher-order modes can be explained in a ray-optical picture by the increasing number of penetrations through the metal film per unit length traveled. With the exception of the plasmonic TM_0 s_b mode the calculations further predict reduced absorption losses for even dielectric-plasmonic TM modes while the absorption is high for odd TM modes. This result can be explained by analysing the z- component of the squared electric field distribution $E_z(x)E_z^*(x)$ which is responsible for resitivity losses of the propagating mode. As described in section 3, the electric field $E_z(x)$ is proportional to $dH_y(x)/d\,\mathrm{x}$ and is therefore out-of-phase with $H_y(x)$. Accordingly, the losses of odd hybrid dielectric-plasmonic TM modes,

which possess an antinode in the electric field distribution at the location of the composite metal film, are higher than for even TM modes. The pattern of effective refractive indices n_{eff} and of absorption coefficients α shown in Figure 5.10 can be modified in a controlled manner by shifting the position of the metallic film to an antinode of higher order TM modes or by inserting two or more metal films at specific locations in the waveguide as demonstrated in waveguide T_1. This way waveguides with desired hybrid dielectric-plasmonic mode properties can be designed.

Chapter 6 Eliminating thermal effects in z-scan measurements and nonlinear optical properties of organic materials

6.1 Introduction

The z-scan technique is a highly sensitive optical method that allows measuring both the two photon absorption (TPA) coefficient and the nonlinear refractive index [57,58]. Due to this advantage the z-scan technique has been widely used to study the nonlinear optical properties of semiconductors [59,60], nanoparticles [61,62], hybrid structures [55,63,64] and organic materials [46–49,65]. Depending on the damage threshold of the material and on the size of the investigated samples different lasers are applied. For large crystal lengths (1 mm or more) [151,152] or molecules in solution in a cuvette [48,61,65] low-repetition, high pulse fluence lasers with focus diameters of several 100 micrometers are used. In order to avoid structural changes of materials with low damage threshold high repetition 100 fs pulses with low energy fluence per pulse are applied [60]. The small fluence also allows for tighter focusing of the incident beam without damaging the material enabling the z-scan technique for thin solid films [153,154]. However, due to the high pulse repetition rate the nonlinear signal is often modified by

accumulated thermal effects [64,66–69] since the sample has not reached the ambient temperature before the next pulse arrives [70,107]. Various approaches have been reported to manage accumulated heating [66–68,70] considering that thermal effects can be reduced if the pulse repetition time exceeds the heat diffusion time from the optically excited sample area [70]. In most of these investigations, a mechanical chopper has been used to control the exposure time of the sample by setting a chopping frequency and a chopper opening rise time [66–68]. Since the sample is excited by a train of pulses during the chopper opening time, this technique has limitations for materials with fast thermal build-up time [66–70]. As an alternative approach to eliminate heat accumulation in thin, dielectric films I propose the application of low fluence 100 fs laser pulses at reduced repetition rates using an acousto-optic modulator (AOM) as pulse selector. In addition, the pulses are tightly focused to reduce the thermal diffusion time from the area of the laser excitation into the unexcited film area.

Many of organic materials show high nonlinearities [46–49]. They are promising materials for nonlinear optical applications including optical power limiting [49–52] and two-photon 3D data storage [53,54]. Together with the large nonlinearities and the ability to form composite and hybrid nanostructures with semiconductors or metals, organic materials show a broad potential to increase the nonlinear response of photonic structures [55,56]. In general, many perylene derivatives have shown TPA cross sections up to 8000 GM at nearly resonant excitation [48,49]. Using the proposed modified z-scan technique I was able to determine the nonlinear optical constants of OMBD grown PTCDA. The two-photon-absorption cross-section of a PTCDA colloidal solution at 820 nm [65] and the third order susceptibility $\chi^{(3)}$ of a vacuum deposited PTCDA film using degenerate four wave mixing experiments at 602 nm

[155] have been previously reported. These values serve as reference to test our modified tightly focused z-scan technique using 100 fs pulses at reduced pulse repetition rate.and of an aluminum-quinoline (Alq_3) films which have been grown by organic molecular beam deposition (OMBD) on a Pyrex® substrate.

Since Alq_3 has attracted a significant attention for its use as both an electron transporting layer (ETL) and an emissive layer in Alq_3 based organic light-emitting diodes (OLEDs) [11,84–87] many researchers focus on enhancing the quantum efficiency, luminescence efficiency and life time of Alq_3 based OLED devices. Therefore reliable investigation of nonlinear optical properties of Alq_3thin films does not exist. The proposed "modified tightly focus z-scan technique" was used and all the third order nonlinear parameters of an Alq_3 thin film were measured. In addition in this Chapter, the accumulated thermal effect in the focus area, which erroneously modifies the z-scan measurements, is systematically investigated using the open aperture z-scan technique with high repetition rate femtosecond laser pulses on thin PTCDA and Alq_3 films in Sections 6.3 and 6.4.

6.2 z-scan set up and experimental details

The z-scan set up [57] is shown in Figure 6.1. The transmittance of the film was measured as a function of sample position (z-axis) with respect to the focal plane (at z = 0). A Ti:Sapphire laser tuned to 820 nm was the excitation source providing ultrashort pulses of ~100 fs temporal width at a pulse repetition rate of 80 MHz (corresponding to a pulse repetition time of 12.5 ns). In order to avoid heat accumulation or even structural damage in the organic film, the pulse repetition rate is reduced by diffracting the pulses with an acousto-optic pulse

selector at a variable division ratio (DR) ranging from 60 to 1600. Accordingly, the first-order diffracted pulses, which are used for the z-scan measurements, have a pulse repetition time ranging from 0.75 to 20 µs. The first- to (not diffracted) zero-order pulse intensity ratio

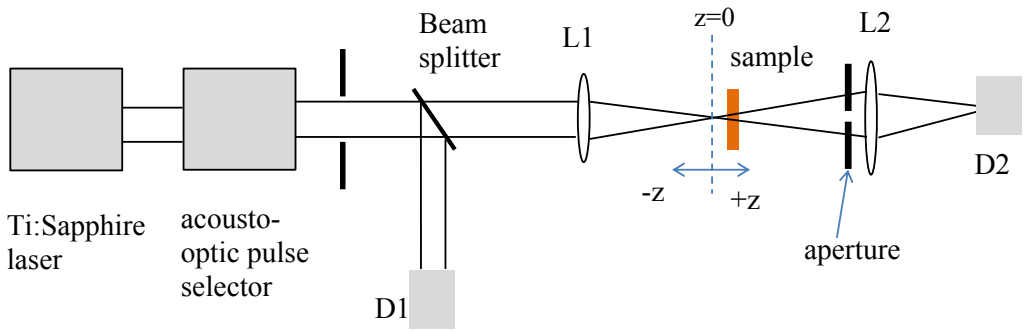

Figure 6.1: Schematic sketch of experimental setup of the z-scan experiments

was monitored with an oscilloscope using a fast photodiode. The ratio had a value of more than 1000 independent of the used DR. This zero-order background was further reduced by inserting a diaphragm in front of the z-scan setup. The remaining zero-order pulse intensity contributes to a constant transmission background.

While this contribution is negligible at low DR it becomes important for long repetition times (> 1.25 µs) where several hundreds of weak zero-order pulses pass the sample between each of the strong first-order diffracted pulses. To correct for this background, the average power of the laser beam was measured after the diaphragm with the AOM being switched on or off at each DR prior to each z-scan measurement, revealing the constant zero-order pulse power. The resulting zero-order background was subtracted from the experimentally obtained z-scan transmission signal. Likewise, the peak power P_0 of the

exciting pulses was determined resulting in nearly constant peak intensity I_0 independent of the DR.

After the diaphragm the first-order diffracted laser beam was divided by a beam splitter (with 90% transmssion) directing the reflected beam onto a fast Si photodiode for reference. The transmitted beam (~2mm diameter) was directed towards a microscope objective which focussed the laser pulses tightly onto the film. Measurements were made with a high-aperture 10x long working distance microscope objective (focal length ~20 mm) and then repeated with a high-aperture 20x microscope objective (focal length ~10 mm). The temporal width of the 100 fs pulses broadens when they pass the glass elements of the microscope objective lenses due to group-velocity-dispersion which affects the peak intensity I_0. The pulse widths after the 10x or the 20x microscope objective were measured to be 175 fs and 180 fs, respectively, by second-harmonic-generation autocorrelation in a BBO crystal. The organic film on the Pyrex substrate was mounted on a piezo-translational stage, which was moved in step sizes ranging from 20 to 40 μm. The transmitted light (the z-scan signal) was collected by a fast Si photodiode. In addition, an optical long pass filter was placed in front of the photodiode to block any photoluminescence when the PTCDA film is excited. The reference and z-scan signals were recorded simultaneously by two identical Agilent digital multimeters while moving the film from its negative to its positive z position (with respect to the focal plane, z = 0). Subsequently, the z-scan transmittance was divided by the reference signal to eliminate laser intensity fluctuations or changes of the spatial laser profile during the data acquisition.

The change in transmittance due to two photon absorption (TPA) and nonlinear refraction is very small in a ~1μm thick PTCDA film (in the 0.6% range) and in a 3μm thick Alq_3 film (in the range of 0.15%) when using low energy fluence pulses. Therefore, multiple z-scans were recorded and averaged at both high and very low (attenuated by a factor of ~100) pulse intensity to improve the signal-to-noise ratio in these experiments. The transmittance at very low excitation intensity which does not lead to a z-scan signal serves as a reference of the linear transmittance during the movement of the sample along the z-axis. It allows to eliminate changes in transmittance with z due to surface imperfections of the sample [57].

6.3 z-scan measurements on PTCDA

6.3.1 Open aperture z-scan on PTCDA

An approximately 0.9 μm thick PTCDA film was used in our modified z-scan measurements. Thickness variations of ~ ±0.2 μm due to oblique growth across the sample area were determined with a profilometer and have been considered in the evaluations of the z-scandata. In order to study the accumulation of heat in the PTCDA film and its influence on the z-scan measurements we used a 10x microscope objective lens and varied the laser repetition time of incident laser pulses from 1.25 to 20 μs at a beam irradiance of 37 GW/cm^2. The background subtracted normalized transmittance for various pulse repetition times (as labelled) is shown in Figure 6.2. In these measurements the aperture after the sample was completely open resulting in a transmittance dip in the vicinity of z = 0 due to TPA. While the transmittance

dip is constant for repetition times ranging from 5 to 20 μs the dip steadily decreases for repetition time smaller than 5 μs.

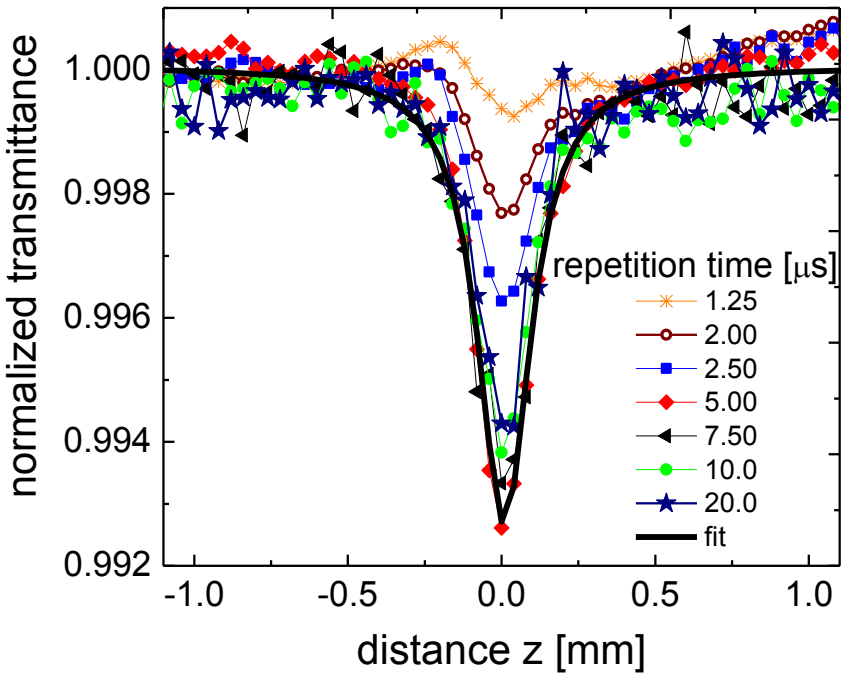

Figure 6.2: Normalized open aperture transmittance of a PTCDA film as a function of z-axis displacement using a 10x microscope objective lens at different repetition times as labelled. The incident laser intensity was 37 GW/cm^2. The solid line represents the theoretical fit using Eq.(6.1) as described in the text.

The corresponding two-photon-absorption coefficient β of the PTCDA film is determined by fitting the experimental data according to

$$T(z) = \sum_{0}^{\infty} \frac{\left[-q_0(z,0)\right]^m}{(m+1)^{3/2}} \tag{6.1}$$

where $q_0(z,t) = \frac{\beta I_0(t) L_{eff}}{\left(1 + z^2/z_0^2\right)}$ and $I_0(t) = \frac{P_{av}}{\pi\left(\omega_0^2/2\right)\gamma_{rep}\Delta t}$ [57].

Here $I_0(t)$ is the pulse irradiance at the focal plane, γ_{rep} is the pulse repetition rate (80 MHz/), $z_0 = \pi\omega_0^2/\lambda$ is the Rayleigh length of the beam, z is the sample position and ω_0 is the radius of the focused Gaussian (electric-field) beam waist which was determined by fitting the transmittance dips with Eq. (6.1). The average value of all beam waists ω_0 at different DRs was found to be 5.2±0.3 and 2.6±0.3 μm for the 10x or 20x lens, respectively. The effective film thickness L_{eff} is given by $L_{eff} = \left(1 - e^{-\alpha L}\right)/\alpha$ with L being the sample thickness and $\alpha = 1.5 \times 10^4\ \text{m}^{-1}$ being the linear absorption coefficient of PTCDA at 820 nm [156]. The thick solid line in Figure 6.2 exemplarily represents the theoretical fit of the transmittance for a repetition time of 5.0 μs resulting in a TPA coefficient of 6.0 ± 0.6 cm/GW.

The extracted TPA coefficients for all repetition times are shown in Figure 6.3 as red squares. The vertical error bar in Figure 6.3 represents the ~10% experimental error of these values. The noise is attributed laser intensity instabilities and to long-term temperature fluctuations which cause slight changes in the laser pulse energy and in the pulse width. As mentioned before, we attribute the reduction of the TPA coefficients for repetition times shorter than 5 μs to the accumulation of heat in the PTCDA film which is predominantly caused by the non-radiative recombination of Frenkel excitons, excimers and charge transfer excitons [3,4,97,157,158]. Our interpretation is supported by comparing the onset of the heating effect for repetition times smaller than 5 μs with the thermal diffusion time t_d of the

accumulated heat within the laser focus area into the adjacent unexcited sample region in the PTCDA film. The thermal diffusion time t_d is given by the relation [67,70]

$$t_d = \frac{\omega_0^2}{4D} \tag{6.2}$$

Here, D = 0.05 cm^2 s^{-1} is the heat diffusion constant for PTCDA [159]. The derived thermal diffusion time using the 10x microscope lens amounts to 1.35 µs. This time is close to the

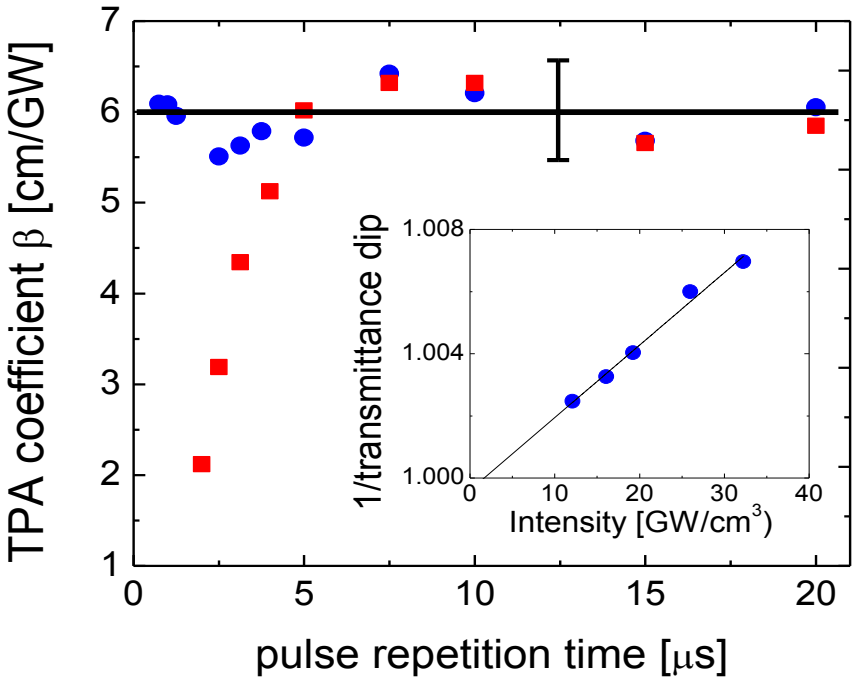

Figure 6.3: Experimentally determined TPA coefficient β for a PTCDA film using a 10x (red squares) and 20x (blue circles) microscope objective lens as a function of different repetition times as labelled. Inset: Invers of the transmittance dip as a function of incident intensity using a 20x objective lens at a pulse repetition time of 3.125 µs.

repetition time of 1.25 μs, where heat accumulation drastically affects the z scan measurement (see Fig 6.2) resulting in a very low TPA coefficient due to filling of excited states and the formation of a thermal lens as discussed in Section 6.2. For repetition times between 1.35 and 5.0 μs, the nonlinear transmission is gradually less affected by accumulated thermal effects.

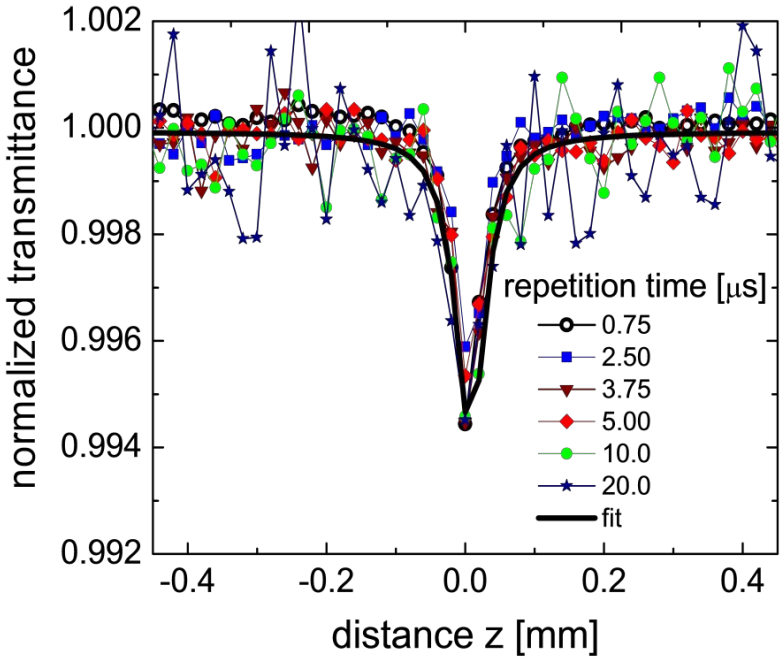

Figure 6.4: Normalized open aperture transmittance of a PTCDA film as a function of the z-axis displacement using a 20x microscope objective lens at different repetition times as labelled. The incident laser intensity was 26 GW/cm^2. The solid line represents the theoretical fit using Eq.(6.1) as described in the text.

To further support this interpretation we repeated the z-scan measurements with a 20x microscope objective lens resulting in a tighter focus. For better comparison, we excited the

PTCDA film with a similar energy flux as in the measurements with the 10x microscope objective lens by introducing attenuators into the beam path. Using Eq. (6.2) and a focus radius of ω_0 = 2.6 μm we obtain a heat-diffusion time of t_d = 0.34 μs. Accordingly, we expect a faster heat diffusion from the heated focus area into the unexcited film area and hence no or a less significant reduction of the TPA coefficient at laser repetition times below 5.0 μs. Figure 6.4 shows the normalized transmittance with the background subtracted as a function of the laser repetition time using the 20x lens at a beam irradiance of 26 GW/cm^2 for various repetition times as labelled. As before, the solid line represents the theoretical fit using Eq. (6.1) at a repetition time of 10.0 μs which results in a TPA coefficient of 6.2 ± 0.6 cm/GW. The extracted TPA coefficients are plotted in Figure 6.3 as blue circles as a function of the pulse repetition time. For repetition times longer than 0.75 μs no reduction of the transmission dip or of the value of the TPA coefficient due to accumulated heating was observed. The inset of Figure 6.3 shows the linear increase of the inverse of the transmission dip as a function of the pulse intensity at a repetition time of 3.125 μs using the 20x lens, confirming that the observed nonlinear process is due to TPA. confirming that the observed nonlinear process is due to TPA Within the experimental error the measured TPA value of β = 6.0 ± 0.6 cm/GW is the same for both the 10x and 20x microscope objective lens. When considering the reflection loss of the incident laser beam at the entrance surface of the PTCDA film (refractive index of 2.22 at 820 nm [98]), the TPA coefficient increases by ~16% resulting in a value of β = 7.0 ± 0.7 cm/GW. This value is higher than the TPA coefficient of β = 4.3 ± 0.5 cm/GW for colloidal PTCDA nanocrystals in solution at 820 nm [65]. The TPA coefficient has been calculated from the two-photon-absorption-cross-section σ = 40 GM

using the expression $\sigma = h\nu\beta/N$ [48], where N is the number of molecules (2) per unit volume of 766.5×10^{-24} cm^{-3} for α-PTCDA [96], $h\nu$ is the photon energy. Due to its crystalline structure, PTCDA nanocrystals and films show a strong optical anisotropy for electric fields polarized within the molecular plane or along the molecular stacking direction (which is nearly normal to the molecular plane). Due to the higher electron density within the molecular plane, PTCDA films exhibit significantly higher in-plane linear absorption values and refractive index values as compared to out-of-plane values [160,161]. We therefore expect higher TPA values for in-plane polarized electric fields in α-PTCDA films than from randomly orientated PTCDA nanocrystals in colloidal solution which may explain the discrepancy between our TPA coefficient and the reported TPA from PTCDA nanocrystals. Z-scan experiments on α-PTCDA crystals [97] by rotating the light polarization with respect to the molecular plane or the molecular stacking direction similar as in[162] ,would provide additional information to clarify the anisotropy of the nonlinear response.

With the nonlinear absorption coefficient β the imaginary part of the third order nonlinear susceptibilty $\chi_I^{(3)}(\mathrm{SI})$ for PTCDA can be calculated according to the relation [63],

$$\chi_I^{(3)}(\mathrm{SI}) = n_0^2\varepsilon_0 c\lambda\beta/3\pi = 2n_0^2\varepsilon_0 c^2\beta/3\omega \tag{6.3}$$

which leads to $\chi_I^{(3)}(\mathrm{SI}) = 6.8\times10^{-20}\ \mathrm{m^2/V^2}$ using the linear refractive index $n_0 = 2.22$ at the wavelength of 820 nm [98]. The $\chi_I^{(3)}(\mathrm{SI})$ value is equivalent to $\chi_I^{(3)}(\mathrm{cgs}) = 4.8\times10^{-11}\ esu$ in cgs units using the conversion [162],

$$\chi^{(n)}(\mathrm{SI})/\chi^{(n)}(\mathrm{cgs}) = 4\pi/\left(3\times10^4\right)^{n-1} \tag{6.4}$$

6.3.2 Closed aperture z-scan on PTCDA

Closed aperture z-scan measurements, which are sensitive to both nonlinear refraction and nonlinear absorption, were performed at a repetition time of 0.75 μs with the 20x lens. The small (closed) aperture transmits 10% of the light of the open aperture z-scan measurements. Dividing the normalized closed aperture transmittance by the normalized open aperture transmittance extracts the contribution of the nonlinear refraction. Figure 6.5 shows the normalized closed/open z-scan signals for the PTCDA film at an intensity I_0 = 22 GW/cm^2. The valley-to peak profile of the closed aperture z-scan trace indicates that the nonlinear refractive index for the PTCDA thin film is positive (self-focusing). The phase shift $\Delta\phi_0$ of the transmitted light due to the nonlinear refractive index can be deduced by fitting the normalized closed/open transmittance with the following equation [57];

$$T\left(z,\Delta\varphi_0\right)=1+\frac{4\Delta\phi_0 x}{\left(x^2+9\right)\left(x^2+1\right)} \tag{6.5}$$

where $x=z/z_0$. Hence the nonlinear refractive index n_2 can be calculated using the relation:

$$\Delta\phi_0 = kI_0 n_2 L_{eff}. \tag{6.6}$$

The solid line in Figure 6.5 shows the theoretical fit using Eq. (6.5) with ω_0 = 2.6 μm providing a nonlinear phase shift of $\Delta\phi_0$ = 0.022. The resulting nonlinear refractive index n_2 amounts to (1.2± 0.3)×10^{-13} cm^2/W using Eq. (6.6), which is equivalent to 6.4×10^{-11} *esu* using

using the relation $n_2(esu) = cn_0n_2\left(\mathrm{m}^2/\mathrm{V}^2\right)/40\pi$ [57]. Considering the reflection losses at the entrance surface of the PTCDA further enhances the nonlinear refractive index value by ~16% to $(1.4\pm 0.3)\times10^{-13}$ cm^2/W. The experimental error in this measurement is mainly attributed to dark current noise of the photodiodes. The signal-to-noise ratio could be improved by longer time-integration at each sampling step or by averaging more z-scans.

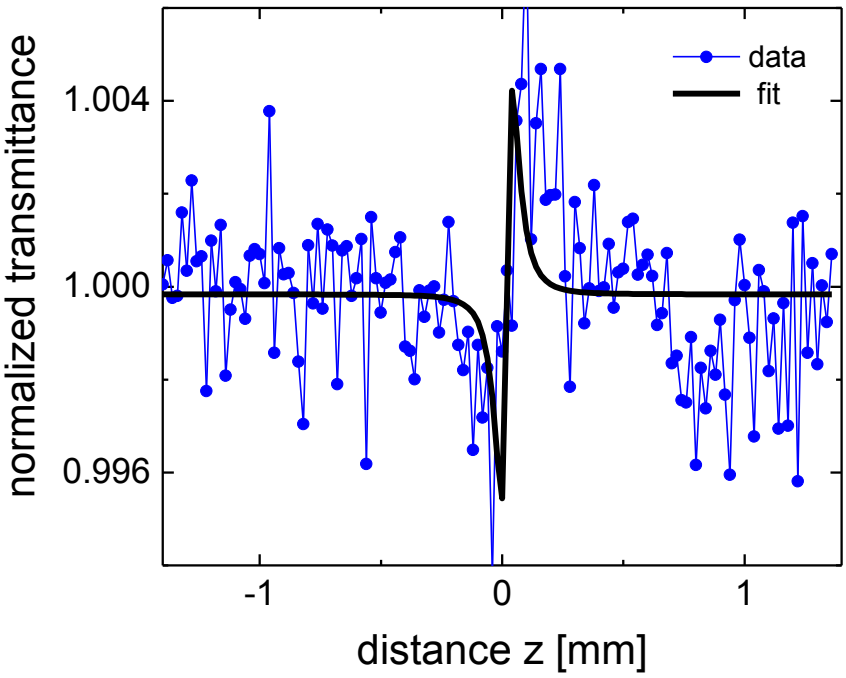

Figure 6.5: Normalized closed/open z-scans at the repetition time of 0.75 μs using a 20x microscope objective lens. The incident laser intensity was 22 $\mathrm{GW/cm}^2$. The solid line represents the theoretical fit using Eq. (6.5) as described in the text.

We also performed closed aperture z-scan measurements with the 10x lens at the repetition time 2.5 μs, where slight heat accumulation has been observed in open aperture z-scan measurements as described earlier. Figure 6.6 shows the normalized closed/open z-scan at an

intensity of I_0 = 37 GW/cm^2. The solid line represents the theoretical fit according to Eq. (6.5) (using a beam waist of ω_0 = 5.2 µm), which renders a nonlinear phase shift of $\Delta\phi_0$ = 0.028 and results in a nonlinear refraction coefficient of (9.5± 0.3)×10^{-14} cm^2/W. This value is by ~25% lower compared to the n_2 coefficient measured with the 20x microscope objective lens.

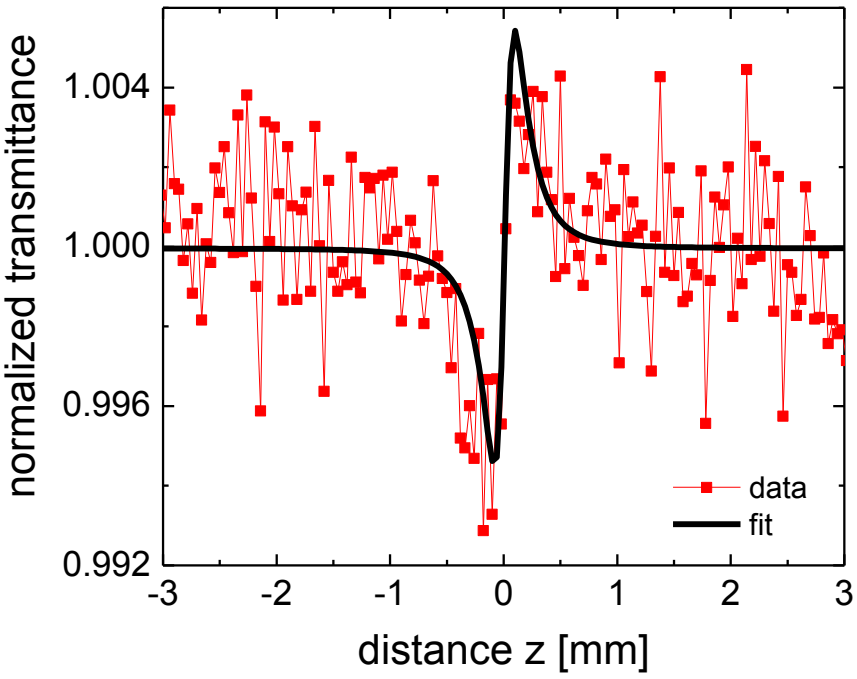

Figure 6.6: Normalized closed/open z-scans at the repetition time of 2.5 µs with 10x microscope objective lens. The incident laser intensity was 37 GW/cm^2. The solid line represents the theoretical fit using Eq. (6.5).

We attribute this reduction to the formation of a thermal lens which causes a counteracting negative refraction [66–70]. From the nonlinear refractive index value n_2 for the 20x lens the real part of the third order nonlinear susceptibilty $\chi_R^{(3)}$ for PTCDA is found to be

$\chi_R^{(3)}(\mathrm{SI}) = 2.1\times10^{-19}\ \mathrm{m}^2/\mathrm{V}^2$ using the relationship $\chi_R^{(3)}(\mathrm{SI}) = 4n_0^2\varepsilon_0 c\gamma/3$ [63]. This value leads to $\chi_R^{(3)}(\mathrm{cgs}) = 1.5\times10^{-10}\ esu$ using Eq. (6.4). This value is in good agreement with the reported value of $\chi_R^{(3)}(\mathrm{cgs}) = 2.0\times10^{-10}\ esu$ which was measured with degenerate four wave mixing at an excitation wavelength of 602 nm.

6.4 z-scan measurements on Alq_3

6.4.1 Open aperture z-scan on Alq_3

A 3.0±0.1 μm thick OMBD grown Alq_3 film was used for the z-scan investigation at an excitation wavelength of 820 nm. The thickness of the film was measured with a profilometer to confirm any growth thickness variation of the film and it was determined that the film thickness was equally thick across the sample. Similar to our z-scan investigation on PTCDA film as described in Section 6.3 the nature of heat accumulation in the Alq_3 film and its influence on the z-scan measurement was studied. A similar procedure was followed as described in Section 6.2 to minimize the background due to the not diffracted zero order pulse from the acousto-optic pulse selector. We first used a 10x microscope objective lens and varied the repetition time of the incident laser pulses from 1.25 to 5.0 μs at a beam irradiance of 48.7 GW/cm^2. The background subtracted normalized open aperture transmittance for various pulse repetition times is shown in Fig. 6.7 as labelled. Unlike the investigations on the PTCDA film (see Figure 6.3), the transmittance dip in z-scan measurements on Alq_3 within the measurement uncertainty of 1x10^{-4} is constant for repetition

times ranging from 1.25 to 5 μs. The solid line in Fig. 6.7 represents the theoretical of Eq. (6.1) at the repetition time 2.5 μs which produce a TPA coefficient of 1.1± 0.2×10^{-1} cm/GW. The average value of all beam waists ω_0 at different DRs was found to be 4.6±0.3 μm. The

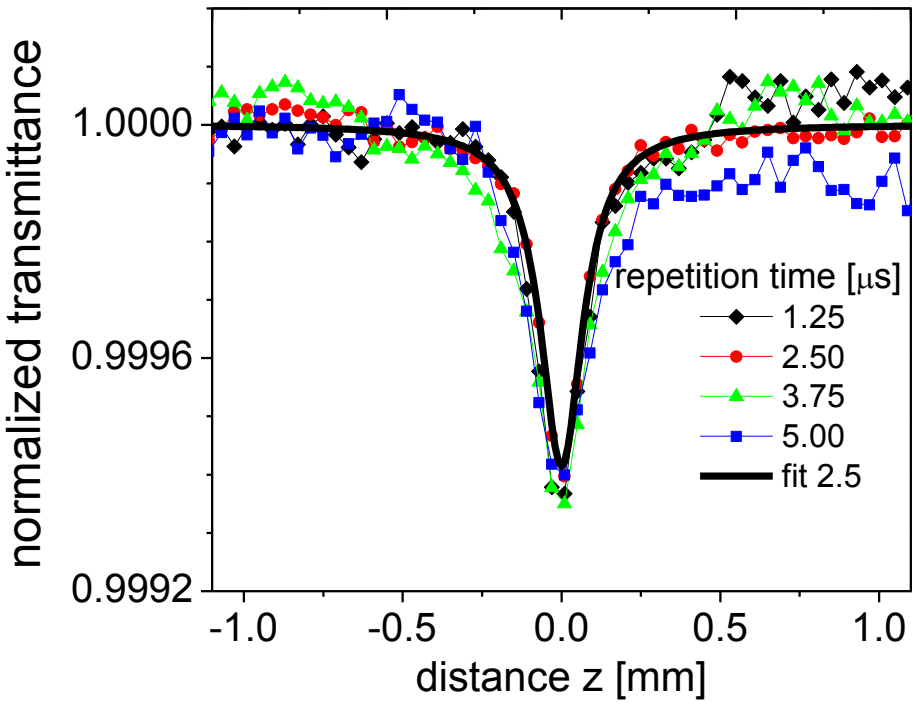

Figure 6.7: Normalized open aperture transmittance of an Alq_3 film as a function of z-axis displacement using a 10x microscope objective lens at different repetition times as labelled. The incident laser intensity was 48.7 GW/cm^2. The solid line represents the theoretical fit using Eq. (6.1) as described in the text.

linear absorption coefficient [111,112,163] $\alpha = 3.6\times10^4$ m^{-1} of Alq_3 at the wavelength 820 nm was used in the calculation. The extracted TPA coefficients at different pulse repetition time are plotted in Figure 6.8 with red squares. As given in Figure 6.8 the vertical error bar represents

~25% experimental error of these values. Reduction of the transmission dip or of the value of the TPA coefficient was not observed for repetition times longer than 1.25 μs with the 10x microscope objective lens indicating that there is no noticeable heat accumulation in the film which is different to observations in earlier z-scan measurements on a PTCDA film. This difference cannot be explained by the heat diffusion constant [164] D = 0.0034 cm^2 $s^{-1}$of Alq_3 which is in the order of 10 times smaller as compared to the value of PTCDA [159]. The reduced thermal effect might be explained with a lower linear absorption at 820 nm in the Alq_3 film as compared to PTCDA where the HOMO-LUMO gap is closer to the exciting laser energy. The reduced linear absorption in Alq_3 films leads to a lower heat production due to non-radiative relaxation processes of singlet-excitons. Furthermore the TPA coefficient of Alq_3 is by a factor of ~60 smaller than in PTCDA [165] leading to a minor generation of two-photon generated excitons in Alq_3 while TPA excitons cannot be neglected in PTCDA at higher excitation intensities. In addition Alq_3 films shows a strong photoluminescence (PL) emission band with an emission yield of ~25% [89,90,92] centred at ~540 nm at room temperature [89,90,95,166] while the radiative recombination in PTCDA is strongly quenched at room temperature. Accordingly, a significant portion of excitons generated from linear and two photon absorption in Alq_3 quickly recombines (within ~20 ns) which further reduces the heat generation in the Alq_3 film. The linear increase of the inverse of the transmission dip as a function of the pulse intensity at a repetition time of 2.5 μs using the 10x lens is shown in the inset of Figure 6.8 confirming that the observed nonlinear process is due to TPA. The deduced TPA coefficients as a function of the incident laser intensity are plotted in Figure 11 with red squares.

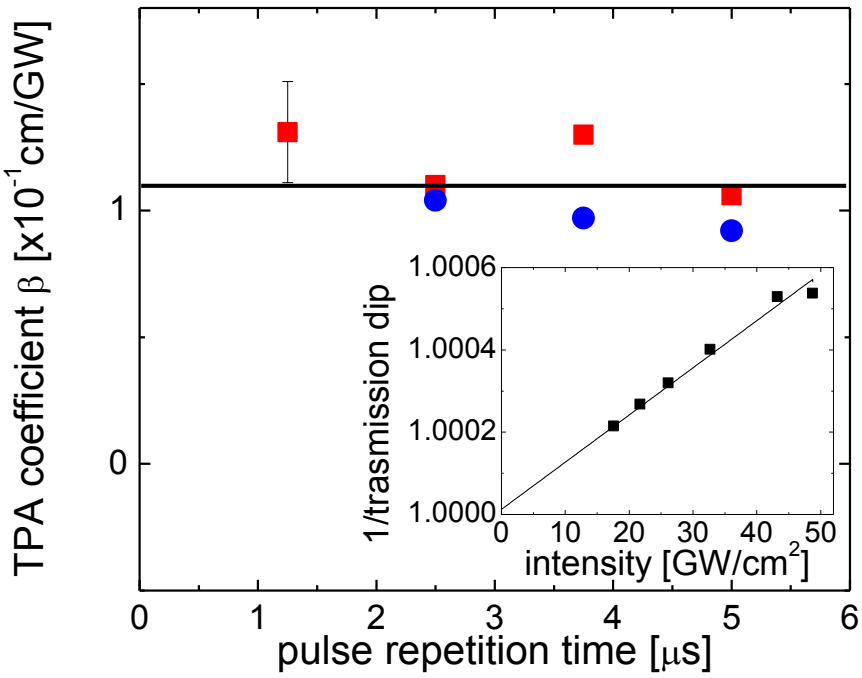

Figure 6.8: Experimentally determined TPA coefficient β for an Alq_3 film using a 10x (red squares) and 20x (blue circles) microscope objective lens as a function of different repetition times as labelled. Inset: Invers of the transmittance dip as a function of incident intensity using a 10x objective lens at a pulse repetition time of 2.5 μs.

The z-scan measurements were repeated with a 20x microscope objective lens resulting in a tighter focus. We excited the Alq_3 film at the same incident power as in the measurements with the 10x microscope objective lens. Figure 6.9 shows the background subtracted normalized transmittance as a function of the laser repetition time using the 20x lens at a beam irradiance of 174 GW/cm^2. The solid line represents the theoretical fit using Eq. (6.1) providing a TPA coefficient of 1.0± 0.2×10^{-1} cm/GW with a focus beam waist of 2.4±0.3 μm at a repetition time of 2.5 μs. The extracted TPA coefficients are plotted in Figure 6.8 as a

function of the pulse repetition time with blue circles. As with 10x microscope objective lens, a reduction of the transmission dip or of the value of the TPA coefficient due to accumulated heating was not observed.

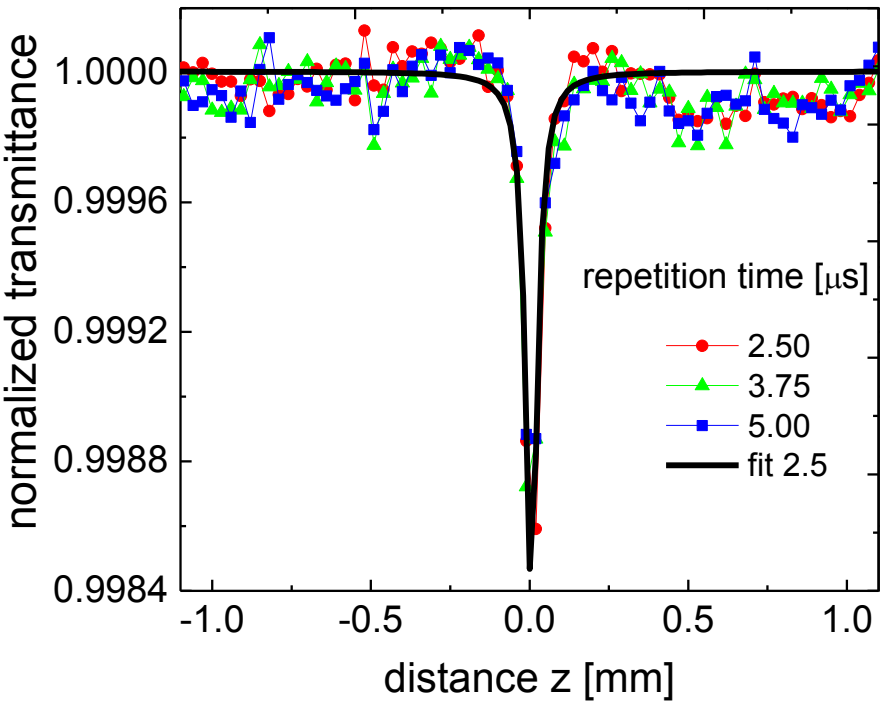

Figure 6.9: Normalized open aperture transmittance of an Alq_3 film as a function of z-axis displacement using a 20x microscope objective lens at different repetition times as labelled. The incident laser intensity was 174 GW/cm^2. The solid line represents the theoretical fit using Eq. (6.1) as described in the text.

The background subtracted normalized transmittance as a function of the incident laser intensity ranging from 64 -174 GW/cm^2 is shown in the Figure 6.10 at the laser repetition time 2.5 μs for the 20x lens. The obtained TPA coefficients as a function of the incident laser

intensity are plotted in Figure 6.11 with blue circles. The inset of Figure 6.11 shows the linear increase of the inverse of the transmission dip as a function of the pulse intensity.

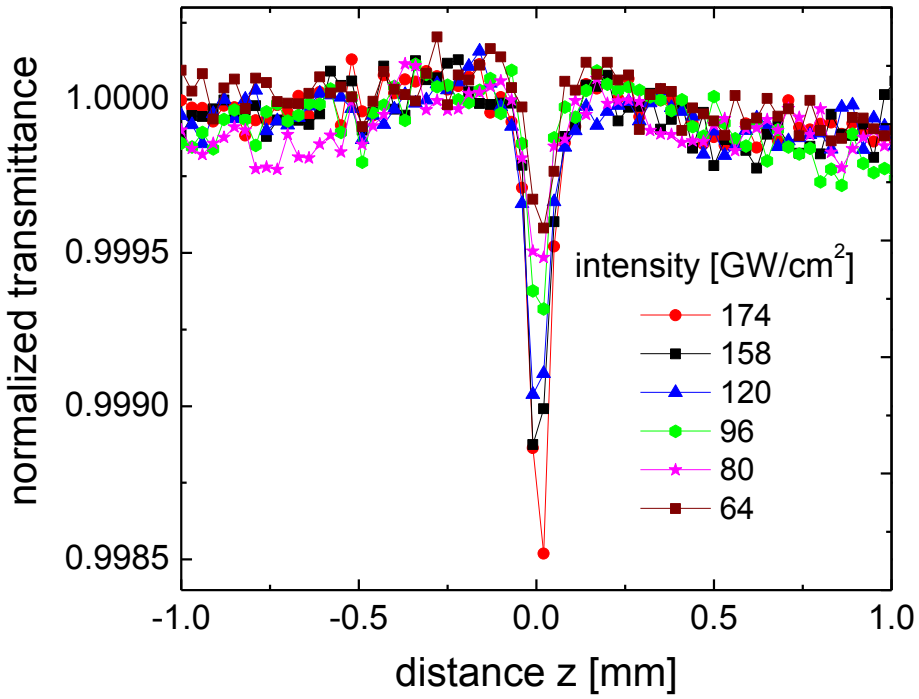

Figure 6.10: Normalized open aperture transmittance of an Alq_3 film as a function of intensity using a 20x microscope objective lens at the repetition time 2.5 μs.

Within the experimental error the average of the measured TPA value is $\beta = (1.0 \pm 0.2)\times10^{-1}$ cm/GW using all the measured TPA values which are plotted in Figure 6.8 and in Figure 6.10 for both the 10x and 20x microscope objective lens . By considering the reflection loss of the incident laser beam at the entrance surface of the Alq_3 film (refractive

index of 1.695 at 820 nm [6]), the TPA coefficient increases by ~6% resulting in a value of β = (1.06 ± 0.2)×10^{-1} cm/GW. The imaginary part of the third order nonlinear susceptibilty $\chi_I^{(3)}(\mathrm{SI})$ for Alq_3 was found as $\chi_I^{(3)}(\mathrm{SI}) = 6.6\times10^{-22}\ \mathrm{m^2/V^2}$ by (6.3) using the determined nonlinear absorption coefficient β and the linear refractive index $n_0 = 1.695$ at the wavelength of 820 nm [6]. The $\chi_I^{(3)}(\mathrm{SI})$ is equivalent to $\chi_I^{(3)}(\mathrm{cgs}) = 4.7\times10^{-13}$ *esu* using the Eq.(6.4).

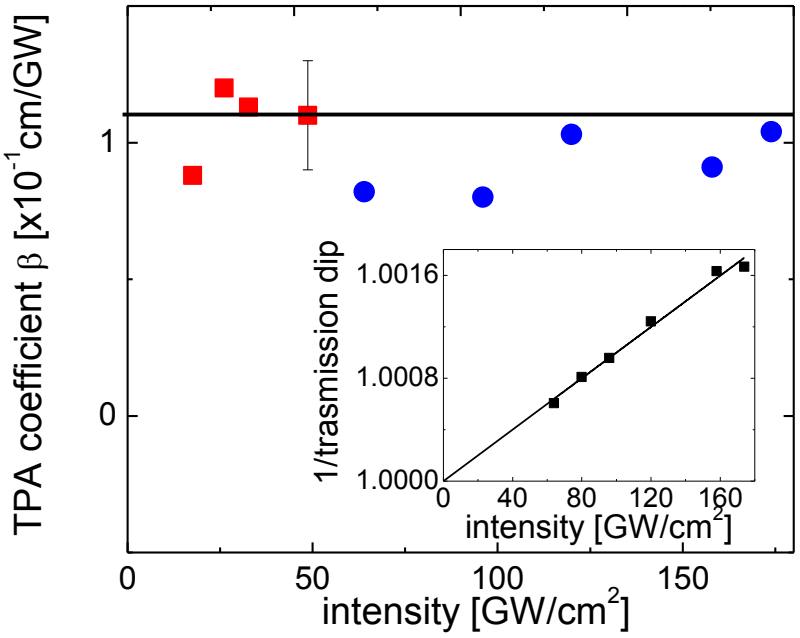

Figure 6.11: Experimentally determined TPA coefficient β for an Alq_3 film using a 10x (red squares) and 20x (blue circles) microscope objective lens as a function of incident laser intensity as labelled. Inset: Invers of the transmittance dip as a function of incident intensity

6.4.2 Closed aperture z-scan on Alq_3

We performed the closed aperture z-scan measurements at the repetition time 2.5 μswith the 10x lens. The small aperture transmits 5% of the light compare to the open aperture z-scan measurements. The normalized closed/open z-scan signals for the Alq_3 film is shown in

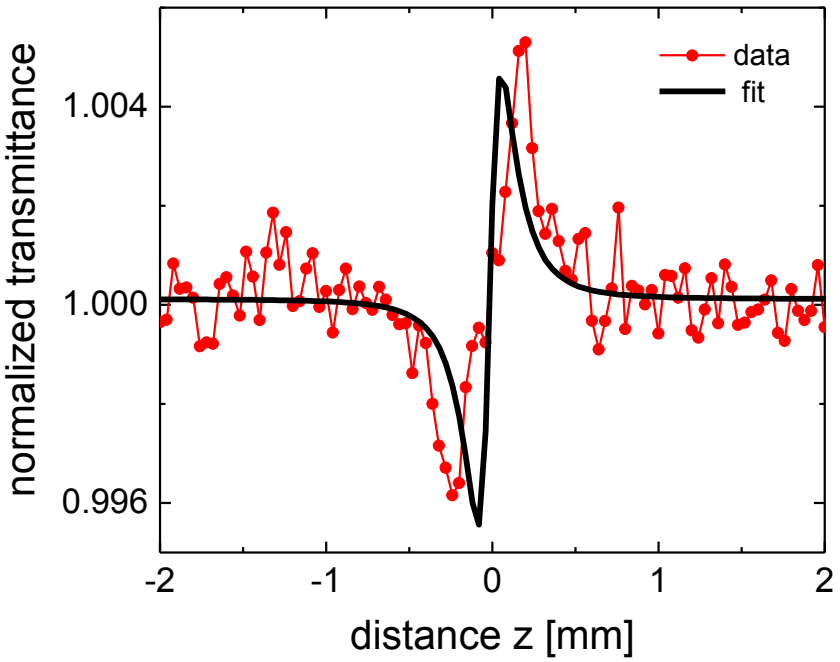

Figure 6.12: Normalized closed/open z-scans at the repetition time of 2.5 μs using a 10x microscope objective lens. The incident laser intensity was 48.7 GW/cm^2. The solid line represents the theoretical fit using Eq. (6.5) as described in the text.

Figure 6.12 at an intensity I_0 = 48.7 GW/cm^2. The valley-to peak profile of the closed aperture z-scan trace indicates that the nonlinear refractive index for the Alq_3 film is positive (self-focusing). Here, the closed aperture z-scan signal is very weak in the 0.4% range but the

valley-to-peak profile is clearly visible within the experimental error of ~12%. The solid line in Figure 6.12 shows the theoretical fit of Eq. (6.5) with the nonlinear phase shift of $\Delta\phi_0$ = 0.023 and the beam waist of ω_0 = 4.6 μm. The nonlinear refractive index n_2 is found to be $(2.1\pm 0.3)\times10^{-14}$ cm^2/W using the Eq. (6.6), resulting 8.5×10^{-12} *esu*. The real part of the third order nonlinear susceptibilty $\chi_R^{(3)}$ for Alq_3 is found to be $\chi_R^{(3)}(\mathrm{SI}) = 2.1\times10^{-20}\ m^2/V^2$ using the nonlinear refractive index n_2 which leads to $\chi_R^{(3)}(\mathrm{cgs}) = 1.5\times10^{-11}$ *esu*.

Chapter 7 Summary

This thesis presents the investigation of optical properties of organic films and plasmonic metal-organic waveguides fabricated by organic molecular beam deposition. The thesis contains the linear optical properties on Alq_3 films which were performed by spectrally and time-integrated photoluminescence (PL) using a photodiode and time-resolved PL using the time-correlated single photon counting (TCSPC) technique. The intensity and temperature dependence saturation of the quenching of light emission in Alq_3 films due to exciton-exciton annihilation is investigated. In addition, the possibility of controlling the refractive index dispersion in organic/organic multilayer waveguides is presented. Particularly, the properties of guided modes in plasmonic Alq_3 waveguides with embedded thin metal layer/s were investigated. Moreover, this thesis presents the nonlinear optical properties PTCDA and Alq_3 thin films which were investigated by z-scan technique.

7.1 Intensity and temperature dependent bimolecular quenching of light emission in Alq_3 films

Spectrally integrated TI and TR PL measurements of a 120 nm thin OMBD grown Alq_3 film show a strong reduction of the PL yield with increasing cw excitation intensity or pulse fluence at 15 K. The reduction of the PL efficiency is attributed to effective singlet-singlet

annihilation processes between interacting excitons which are localized in the energy minima at the grain boundaries of the polycrystalline Alq_3 film. The localization of excitons at these trapping sites leads to very high local (*microscopic*) exciton densities even at low excitation levels. AFM and SEM studies of ultrathin (5 – 15 nm) Alq_3 films support the existence of ordered molecular aggregates and polycrystalline growth with grain sizes in the order of 50 nm. Due to the finite density of quenchable trapping sites the extracted quenching coefficients show a pronounced saturation behavior ranging from $\gamma_{bq} = 110 \times 10^{-9}$ to 1.2×10^{-9} $cm^3 s^{-1}$ at lowest and highest optical excitation levels, respectively. The observed low intensity value is by more than four orders of magnitudes larger than values reported at room temperature assuming charge carrier hopping [103–105] in a positionaly random and completely disordered system of localized states.

The temperature dependent quenching behavior was studied by spectrally integrated TI PL using a photodiode as a detector. The observed reduction of singlet-singlet annihilation between trapped excitons at temperatures ranging from 30 to 150 K is attributed to a thermally activated occupation of non-quenchable states in the vicinity of grain boundary traps. Above 170 K the PL efficiency decreases which is attributed to a release of the trapped excitons and the subsequent filling of non-radiative traps. The observed behavior has been calculated using a coupled rate equation model for steady state excitation. The model includes bimolecular quenching, thermally activated occupation of non-quenchable states and thermally activated de-trapping and mobilization of excitons at higher temperatures. The calculations are in good agreement with the experimental findings. The bimolecular quenching is significantly reduced at higher temperature but bimolecular quenching due to

grain boundary trapped n_2 excitons is active even up to room temperature. We expect that the contribution of singlet-singlet annihilation by trapped n_2 excitons decreases when the size of molecularly ordered (nano-crystalline) areas in Alq_3 films decreases which is equivalent to an increase of the molecular disorder within the Alq_3 film. This could for instance be facilitated by changing the evaporation or the substrate temperature [106,167] or by using a higher growth rate leaving the system less time to form nanocrystals of several 10 nm size. Also, doping the Alq_3 films at high doping levels [168] or the co-deposition with e.g. TPD can [169] significantly increase the molecular disorder within the film. In this case charge carrier hopping becomes an appropriate model to describe exciton quenching [100–102]. Studying bimolecular quenching of Alq_3 films grown at those conditions will be subject of further investigations.

7.2 Refractive index dispersion in single and multi-layered waveguides of Alq_3 and PTCDA

We performed *m*-line measurements on OMBD grown pure PTCDA waveguides (P_1 and P_2), on an Alq_3 waveguide (A_1) and on a PTCDA/Alq_3 effective medium multilayer waveguide (M_1) at excitation wavelengths ranging from the visible to the infrared region. From these measurements the wavelength dispersions $n(\lambda)$ of the in-plane and normal refractive indices were derived using Sellmeier equations. The corresponding fit parameters are summarized in Table 4.1 to Table 4.3. The dispersion curves for pure PTCDA and Alq_3 waveguides are in good agreement with the dispersions curves derived from spectroscopic ellipsometry. Experimentally obtained values for $n_{//}$ and $n_{\perp}$ in waveguide M_1 taken at different wavelengths allowed to determine the filling factors of the components Alq_3 and PTCDA in the multilayer

waveguide taking into account a small tilt of 0.5º of the PTCDA molecular stacks in the PTCDA films. The wavelength dispersion and the birefringence of the fabricated effective medium were subsequently projected with the Sellmeier fits of the pure component materials. Based on the filling factors of the component materials the individual thicknesses of Alq_3 and PTCDA layers within the waveguide could also be determined.

The resulting dispersion curves $n(\lambda)$ of the effective medium waveguide M_1 demonstrate that we successfully tuned the dispersion $n(\lambda)$ and the birefringence $n_{//}$ and $n_{\perp}$ compared to the pure organic component waveguides. Intelligent combinations of birefringent and non-birefringent materials in multilayer structures can thus be used to moderate or enhance the anisotropy of the component material to desired parameters. On the other hand, strategically placed metal layers can be used to increase the effective refractive indices $n_{\text{eff}\perp}$ of plasmonic TM modes and to reduce the effective refractive indices $n_{eff\,//}$ of dielectric TE modes[170]. These two options to tune the dispersion allow to tailor waveguides with a perfect phase match between TE and TM modes, which can then be utilized in polarization sensitive propagation, and mode filtering[120]. We propose to use appropriately designed effective medium Alq_3/PTCDA multilayers with opposite birefringence as waveguides in order to compensate the induced birefringence of the embedded metal layers and to achieve perfect phase matching between a plasmonic TM_0 and a dielectric TE_0 mode. Such a tailored plasmonic effective medium waveguide opens new design opportunities for plasmonic integrated optics in information technologies.

7.3 Controlling guided modes in plasmonic metal/dielectric multilayer waveguides

We experimentally studied guided modes in OMBD grown plasmonic Alq_3 waveguides, which contain one single Alq_3-Mg:Ag composite metal layer or three equally spaced layers close to the center of the waveguide. The metallic layers had thicknesses of 7, 9 and 13 nm, respectively. We used the *m*-line technique at a wavelength of 633 nm to investigate the effect of the inserted composite metal layer(s) on the effective refractive indices n_{eff} of TM and TE modes and compared the results to a pure Alq_3 waveguide as reference. TM modes that possess an antinode at the position of the composite metallic layer(s) show high effective refractive indices which indicate the plasmonic character of the modes. Other TM modes have hybrid dielectric-plasmonic characters, showing a high effective refractive index when one electric field antinode is close to a metallic layer. TM modes which possess all their antinode(s) in the dielectric layers propagate essentially like dielectric modes. Transverse electric (TE) modes with antinode(s) at the position of the metal layer(s) are strongly damped, while the losses are low for TE modes comprising a node at the position of the composite metal film(s). Our experiments and calculations demonstrate that strategically placed composite dielectric-metal or continous metal layers can be used to increase and to reduce the effective refractive indices of specific TM and TE modes, respectively. In addition, it is also possible to selectively excite and/or attenuate various TM or TE modes in a controlled way. Mode selective attenuaters could for instance be realized by inserting metal stripes into an dielectric waveguide during growth or by blocking the pump-beam of a loss compensated plasmonic waveguide [171] with an opaque few 10 μm wide mask. Shifting the effective refractive indices of TM and TE modes to

higher or lower values, respectively, further enables new design opportunities for mode coupling between orthogonal TM and TE modes. The combination of selective attenuation and mode coupling could further allow the design of TM/TE stop polarizers [172].

7.4 Eliminating thermal effects in z-scan measurements and nonlinear properties of organic materials

7.4.1 Two photon absorption and nonlinear refraction on PTCDA thin films

We performed z-scan measurements on an OMBD grown PTCDA thin film with tightly focused100 fs laser pulses at a wavelength of 820 nm. Cumulative thermal effects due to sample heating in the focus area were investigated by varying the laser repetition time using an acousto-optic pulse selector and by applying different focus diameters on the sample. Our results show that z-scan measurements using a 10x microscope objective lens at repetition times shorter than 5.0 μs are modified by the accumulating heat within the optically excited area. For repetition times longer than 5.0 μs we observe a constant transmittance dip indicating that thermal effects can be neglected. Thermal effects at higher repetition times are diminished by a smaller focus area created by a 20x microscope objective lens. The larger gradient of the smaller focus area leads to a faster heat diffusion from the excited focus into the unexcited film. The measured TPA coefficient β, the nonlinear refractive index n_2 and the third-order susceptibilities $\chi^{(3)} = \chi_R^{(3)} + i\chi_I^{(3)}$ of the PTCDA films at a wavelength 820 nm are

summarized in Table 7.1. (Reflection losses at the entrance surface of the films have not been considered.)

Our experiments demonstrate that a modified z-scan technique which uses tightly focused 100 fs pulses at reduced repetition rates opens new prospects to measure the nonlinear optical properties of soft organic films. These soft films usually suffer from thermal effects or from structural damage in the standard z-scan setup. The modified z-scan technique can also be applied to plasmonic organic/metal films and nanostructures where thermal accumulation effects are severe limiting factors.

Table 7.1: Measured two-photon absorption coefficient β, nonlinear refractive index n_2 and third order susceptibility values $\chi_I^{(3)}$ and $\chi_R^{(3)}$ of the PTCDA film at a wavelength of 820 nm.

β	n_2	n_2	$\chi_I^{(3)}$	$\chi_I^{(3)}$	$\chi_R^{(3)}$	$\chi_R^{(3)}$
cm/GW	**cm^2/W**	**esu**	**m^2/V^2**	**esu**	**m^2/V^2**	**esu**
6.0	1.2×10^{-13}	6.4×10^{-11}	6.8×10^{-20}	4.8×10^{-11}	2.1×10^{-19}	1.5×10^{-10}

7.4.2 Two photon absorption and nonlinear refraction on Alq_3 thin films

The z-scan measurements on an OMBD grown Alq_3 thin film were performed with tightly focused100 fs laser pulses at an excitation wavelength of 820 nm. We investigated the accumulative thermal effects due to sample heating in the focus area by varying the laser repetition time using an acousto-optic pulse selector and by using different

focus diameters on the sample. We observe a constant transmittance dip in the z-scan measurements on Alq_3 thin film using a 10x microscope objective lens. This means that thermal effects are not relevant even at shorter repetition times from 1.25 - 5.0 μs. We repeated the measurements with a 20x microscope objective lens which again did not show thermal effects at these repetition times. The measured TPA coefficient β, the nonlinear refractive index n_2 and the third-order susceptibilities $\chi^{(3)} = \chi_R^{(3)} + i\chi_I^{(3)}$ of the Alq_3 films at a wavelength of 820 nm are summarized in Table 7.2.

Table 7.2: Measured two-photon absorption coefficient β, nonlinear refractive index n_2 and third order susceptibility values $\chi_I^{(3)}$ and $\chi_R^{(3)}$ of the Alq_3 film at a wavelength of 820 nm.

β	n_2	n_2	$\chi_I^{(3)}$	$\chi_I^{(3)}$	$\chi_R^{(3)}$	$\chi_R^{(3)}$
cm/GW	**cm^2/W**	**esu**	**m^2/V^2**	**esu**	**m^2/V^2**	**esu**
1.0×10^{-1}	2.1×10^{-14}	8.5×10^{-12}	6.6×10^{-22}	4.7×10^{-13}	2.1×10^{-20}	1.5×10^{-11}

Bibliography:

[1] F. F. So, S. R. Forrest, Y. Q. Shi, and W. H. Steier, Appl. Phys. Lett. **56**, 674 (1990).

[2] Z. Wang, H. Chang, T. Wang, H. Wang, and D. Yan, J. Phys. Chem. B **118**, 4212 (2014).

[3] H. P. Wagner, A. DeSilva, and T. Kampen, Phys. Rev. B **70**, 235201 (2004).

[4] H. P. Wagner, A. DeSilva, V. R. Gangilenka, and T. U. Kampen, J. Appl. Phys. **99**, 024501 (2006).

[5] H. P. Wagner, N. Wickremasinghe, M. Kaveh, M. Ajward, X. Wang, H. Schmitzer, Q. Gao, and C. Jagadish,Proc. *SPIE* **91810**, 91810P-1 (2014).

[6] N. Wickremasinghe, J. Thompson, X. Wang, H. Schmitzer, and H. P. Wagner, *Refractive Index Dispersion and Waveguiding in Single and Multilayer Organic Films* (to be published).

[7] F.G. Celii and S. J. Jacobs (United States Patent, 2001).

[8] A. Dodabalapur, Solid State Commun. **102**, 259 (1997).

[9] J. E. Knox, M. D. Halls, H. P. Hratchian, and H. B. Schlegel, Phys. Chem. Chem. Phys. **8**, 1371 (2006).

[10] B. W. D'Andrade and S. R. Forrest, Adv. Mater. **16**, 1585 (2004).

[11] Z. Shen, P. E. Burrows, V. Bulovic, S. R. Forrest, and M. E. Thompson, Sc **276**, 2009 (2009).

[12] S. Mukherjee and P. Thilagar, Dye. Pigment. **110**, 2 (2014).

[13] W. C. H. Choy, *Organic Solar Cells: Materials and Device Physics* (Springer, 2012).

[14] W. Cao and J. Xue, Energy Environ. Sci. **7**, 2123 (2014).

[15] P. Peumans, V. Bulović, and S. R. Forrest, Appl. Phys. Lett. **76**, 3855 (2000).

[16] Z. H. Xiong, D. Wu, Z. V. Vardeny, and J. Shi, Nature **427**, 821 (2004).

[17] H. T. Zhang, S. Han, P. Desai, Y. Q. Zhan, W. Li, W. Si, K. Scott, A. J. Drew, W. P. Gillin, S. J. Zhang, Appl. Phys. Lett. **105**, 203301 (2014).

[18] A. Droghetti, S. Steil, N. Großmann, N. Haag, H. Zhang, M. Willis, W. P. Gillin, A. J. Drew, M. Aeschlimann, S. Sanvito, and M. Cinchetti, Phys. Rev. B **89**, 94412 (2014).

[19] Z. Li, Z. Li, and H. Meng, *Organic Light-Emitting Materials and Devices (optical Science and Engineering)* (Taylor & Francis, 2006).

[20] T. Tsujimura, *OLED Display Fundamentals and Applications* (Wiley-VCH, 2012).

[21] W. Li, R. A. Jones, S. C. Allen, J. C. Heikenfeld, and A. J. Steckl, J. Disp. Technol. **2**, 143 (2006).

[22] L. S. Hung, C. W. Tang, M. G. Mason, P. Raychaudhuri, and J. Madathil, Appl. Phys. Lett. **78**, 544 (2001).

[23] S. Wang, Y. Q. Liu, X. B. Huang, S. L. Xu, J.R. Gong, X. H. Chen, L. Yi, Y. Xu, G. Yu, L. J. Wan, Appl. Phys. A-Materials Sci. Process. **78**, 553 (2004).

[24] D. U. Lee, Y. B. Yoon, S. H. Baek, T. W. Kim, J. H. Seo, and Y. K. Kim, Thin Solid Films **516**, 3627 (2008).

[25] M. Cuba and G. Muralidharan, J. Lumin. **156**, 1 (2014).

[26] G. Baldacchini, P. Chiacchiaretta, R. B. Pode, M. A. Vincenti, and Q. M. Wang, Low Temp. Phys. **38**, 786 (2012).

[27] G. Baldacchini, T. Baldacchini, P. Chiacchiaretta, A. Pace, and R. B. Pode, J. Electrochem. Soc. **154**, 217 (2007).

[28] S. R. Forrest, Chem. Rev. **97**, 1793 (1997).

[29] M. K. Tilsch, K. Hendrix, K. Tan, D. Shemo, R. Bradley, R. Erz, and J. Buth, Thin Solid Films **516**, 107 (2007).

[30] J. Chen, Z. Li, S. Yue, and Q. Gong, Opt. Express **17**, 23603 (2009).

[31] A. Karalis, E. Lidorikis, M. Ibanescu, J. Joannopoulos, and M. Soljačić, Phys. Rev. Lett. **95**, 063901 (2005).

[32] J. T. Kim, J. J. Ju, S. Park, M. Kim, S. K. Park, and S. -Y. Shin, Opt. Express **18**, 2808 (2010).

[33] J. C. Weeber, M. U. Gonzalez, A. L. Baudrion, and A. Dereux, Appl. Phys. Lett. **87**, 221101 (2005).

[34] J. Tian, R. Yang, L. Song, and W. Xue, IEEE J. Quantum Electron. **50**, 898 (2014).

[35] T. Holmgaard, Z. Chen, S. I. Bozhevolnyi, A. Dereux, A. V. Krasavin, A. V. Zayats, and N. B. All, Opt. Express **16**, 13585 (2008).

[36] P.-J. Chiang, Y. -C. Chiang, N. -H. Sun, and S. -X. Hong, Opt. Express **19**, 4324 (2011).

[37] H. Ditlbacher, N. Galler, and D. Koller, Opt. Expressptics Express **16**, 10455 (2008).

[38] A. Kumar, S. F. Yu, X. F. Li, and S. P. Lau, Opt. Express **16**, 16113 (2008).

[39] A. Sellai and M. Elzain, Phys. E **41**, 106 (2008).

[40] G. Veronis and S. Fan, Appl. Phys. Lett. **87**, 131102 (2005).

[41] G. Veronis and S. Fan, Opt. Express **15**, 1211 (2007).

[42] A. Davoyan, I. Shadrivov, S. I. Bozhevolnyi, and Y. Kivshar, J. Nanophotonics **4**, 043509 (2010).

[43] J. A. Dionne, L. A. Sweatlock, H. A. Atwater, and A. Polman, Phys. Rev. B **72**, 075405 (2005).

[44] J. A. Dionne, L. A. Sweatlock, H. A. Atwater, and A. Polman, Phys. Rev. B **73**, 035407 (2006).

[45] J. T. Kim, Opt. Commun. **284**, 4171 (2011).

[46] M. R. Ferdinandus, M. Reichert, T. R. Ensley, H. Hu, D. A. Fishman, S. Webster, D. J. Hagan, and E. W. Van Stryland, Opt. Mater. Express **2**, 1776 (2012).

[47] A. Said, C. Wamsley, and D. Hagan, Chem. Phys. Lett. **228**, 646 (1994).

[48] L. De Boni, C. J. L. Constantino, L. Misoguti, R. F. Aroca, S. C. Zilio, and C. R. Mendonça, Chem. Phys. Lett. **371**, 744 (2003).

[49] S. L. Oliveira, D. S. Corrêa, L. Misoguti, C. J. L. Constantino, R. F. Aroca, S. C. Zilio, and C. R. Mendonça, Adv. Mater. **17**, 1890 (2005).

[50] J. E. Ehrlich, X. L. Wu, I. Y. Lee, Z. Y. Hu, H. Röckel, S. R. Marder, and J. W. Perry, Opt. Lett. **22**, 1843 (1997).

[51] J. W. Perry, K. Mansour, I.-Y.S. Lee, X.-L. Wu, P. V. Bedworth, C. -T. Chen, D. Ng, S. R. Marder, P. Miles, T. Wada, M. Tian, and H. Sasabe, Science **273**, 1533 (1996).

[52] G. S. He, C. Xu, P. N. Prasad, B. A. Reinhardt, J. C. Bhatt, and A. G. Dillard, Opt. Lett. **20**, 435 (1995).

[53] B. H. Cumpston, S. P. Ananthavel, S. Barlow, D. L. Dyer, J. E. Ehrlich, , L. L. Erskine, A. A. Heikal, S. M. Kuebler, I. Y. S. Lee, D. M. Maughon, J. Qin, H. Rockel, M. Rumi, X. -L. Wu, S. R. Marder, and J. W. Perry, Nature **398**, 51 (1999).

[54] J. H. Strickler and W. W. Webb, Opt. Lett. **16**, 1780 (1991).

[55] C. Fuentes-Hernandez, L. A. Padilha, D. Owens, S. -Y. Tseng, S. Webster, J. -Y. Cho, D. J. Hagan, E. W. Van Stryland, S. R. Marder, and B. Kippelen, Proc. SPIE **7049**, 70490O-1 (2008).

[56] P. Innocenzi and B. Lebeau, J. Mater. Chem. **15**, 3821 (2005).

[57] M. Sheik-Bahae, A. A. Said, T. -H. Wei, D. J. Hagan, and E .W. Van Stryland, IEEE J. Quantum Electron. **26**, 760 (1990).

[58] M. Sheik-Bahae, A. A Said, and E. W. Van Stryland, Opt. Lett. **14**, 955 (1989).

[59] W. F. Zhang, Y. B. Huang, M. S. Zhang, and Z. G. Liu, Appl. Phys. Lett. **76**, 1003 (2000).

[60] C. -K. Sun, J. -C. Liang, J. -C. Wang, F. -J. Kao, S. Keller, M. P. Mack, U. Mishra, and S. P. DenBaars, Appl. Phys. Lett. **76**, 439 (2000).

[61] H. P. Li, B. Liu, C. H. Kam, Y. L. Lam, W. X. Que, L. M. Gan, C. H. Chew, and G. Q. Xu, Opt. Mater. **14**, 321 (2000).

[62] B. Yu, C. Zhu, and F. Gan, J. Appl. Phys. **82**, 4532 (1997).

[63] R. del Coso and J. Solis, J. Opt. Soc. Am. B **21**, 640 (2004).

[64] R. De Nalda, R. Del Coso, J. Requejo-Isidro, J. Olivares, A. Suarez-Garcia, J. Solis, and C. N. Afonso, J. Opt. Soc. Am. B **19**, 289 (2002).

[65] Y. Sasaki, H. Takamo, and K. Kasatani, **6839**, 683920 (2007).

[66] M. Falconieri and G. Salvetti, Appl. Phys. B **69**, 133 (1999).

[67] A. Gnoli, L. Razzari, and M. Righini, Opt. Express **13**, 7976 (2005).

[68] K. Kamada, K. Matsunaga, A. Yoshino, and K. Ohta, J. Opt. Soc. Am. B **20**, 529 (2003).

[69] S. Mian, S. McGee, and N. Melikechi, Opt. Commun. **207**, 339 (2002).

[70] M. Falconieri, J. Opt. A Pure Appl. Opt. **1**, 662 (1999).

[71] P. K. Tien, R. Ulrich, and R. J. Martin, Appl. Phys. Lett. **14**, 291 (1969).

[72] R. Ulrich and R. Torge, Appl. Opt. **12**, 2901 (1973).

[73] S. Monneret, P. Huguet-Chantome, and F. Flory, J. Opt. A Pure Appl. Opt. **2**, 188 (2000).

[74] S. Gopalakrishnan and S. Narendar, *Wave Propagation in Nanostructures*. (Springer, 2013).

[75] W. Wang, Q. Yang, F. Fan, H. Xu, and Z. L. Wang, Nano Lett. **11**, 1603 (2011).

[76] A. Leitner, Z. Zhao, H. Brunner, F. R. Aussenegg, and A. Wokaun, Appl. Opt. **32**, 102 (1993).

[77] J. R. Lakowicz, Y. Shen, S. D'Auria, J. Malicka, J. Fang, Z. Gryczynski, and I. Gryczynski, Anal. Biochem. **301**, 261 (2002).

[78] G. J. Lee, Y. Lee, B. Y. Jung, S. G. Jung, C. K. Hwangbo, J. H. Kim, and C. S. Yoon, J. Korean Phys. Soc. **51**, 1555 (2007).

[79] H. Yu, K. Kim, K. Ma, W. Lee, J.-W. Choi, C.-O. Yun, and D. Kim, Biosens. Bioelectron. **41**, 249 (2013).

[80] K. Sokolov, G. Chumanov, and T. M. Cotton, Anal. Chem. **70**, 3898 (1998).

[81] M. Thoreson, Z. Liu, U. Chettiar, and P. Nyga, *Studies on Metal-Dielectric Plasmonic Structures* (California, 2010).

[82] R. Gupta, M. J. Dyer, and W. A. Weimer, J. Appl. Phys. **92**, 5264 (2002).

[83] E. Thouti, N. Chander, V. Dutta, and V. K. Komarala, J. Opt. **15**, 035005 (2013).

[84] P. E. Burrows and S. R. Forrest, Appl. Phys. Lett. **64**, 2285 (1994).

[85] G. Gu, V. Bulović, P. E. Burrows, S. R. Forrest, and M. E. Thompson, Appl. Phys. Lett. **68**, 2606 (1996).

[86] S. K. Saha, Y. K. Su, and F. S. Juang, IEEE J. Quantum Electron. Quantum Electron. **37**, 807 (2001).

[87] D. Ammermann and A. Böhler, *Device Structures and Materials for Organic Light Emitting Diodes* (1997).

[88] M. Cölle, R. E. Dinnebier, and W. Brütting, Chem. Commun. (Camb). **49**, 2908 (2002).

[89] M. Brinkmann, G. Gadret, M. Muccini, and C. Taliani, J. Am. Chem. Soc. **122**, 5147 (2000).

[90] M. Muccini, M. Brinkmann, G. Gadret, C. Taliani, N. Masciocchi, and A. Sironi, Synth. Met. **122**, 31 (2001).

[91] R. Katakura and Y. Koide, **45**, 5730 (2006).

[92] C. Ghica, M. N. Grecu, J. Gmeiner, and V. V Grecu, J. Optoelectron. Adv. Mater. **7**, 2997 (2005).

[93] W. Xie, Z. Pang, Y. Zhao, F. Jiang, H. Yuan, H. Song, and S. Han, J. Cryst. Growth **404**, 164 (2014).

[94] S. -Y. Hung, R. -L. Kao, K. -Y. Lin, C. -C. Yang, K. -S. Lin, Y. -C. Chao, J. -S. Wang, J. -L. Shen, and K. -C. Chiu, Mater. Chem. Phys. **154**, 100 (2015).

[95] A. M. Ajward, X. Wang, N. Wickremasinghe, L. A. A. Desilva, and H. P. Wagner, Phys. Rev. B **88**, 045205 (2013).

[96] M. Möbus, N. Karl, and T. Kobayashi, J. Cryst. Growth **116**, 495 (1992).

[97] V. R. Gangilenka, L. V. Titova, L. M. Smith, H. P. Wagner, L. A. A. DeSilva, L. Gisslén, and R. Scholz, Phys. Rev. B **81**, 155208 (2010).

[98] M. Friedrich, T. Wagner, G. Salvan, S. Park, T. U. Kampen, and D. R. T. Zahn, Appl. Phys. A **75**, 501 (2002).

[99] Y. -H. Ho, K. -Y. Chen, K. -Y. Peng, M. -C. Tsai, W. -C. Tian, and P. -K. Wei, Opt. Express **21**, 8535 (2013).

[100] H. Bässler, Phys. Status Solidi **175**, 15 (1993).

[101] V. I. Arkhipov, E. V Emelianova, and H. Baessler, Phys. Rev. B **70**, 205205 (2004).

[102] V. I. Arkhipov, P. Heremans, E. V Emelianova, and H. Baessler, Phys. Rev. B **71**, 45214 (2005).

[103] I. Sokolik, A. D. Walser, R. Priestley, C. W. Tang, and R. Dorsinville, Synth. Met. **84**, 921 (1997).

[104] R. Priestley, A. D. Walser, and R. Dorsinville, Opt. Commun. **158**, 93 (1998).

[105] J. Męzyk, J. Kalinowski, F. Meinardi, and R. Tubino, Chem. Phys. Lett. **395**, 321 (2004).

[106] D. S. Qin, D. C. Li, Y. Wang, J. D. Zhang, Z. Y. Xie, G. Wang, L. X. Wang, and D. H. Yan, Appl. Phys. Lett. **78**, 437 (2001).

[107] A.M. Ajward, *Linear and Non-Linear Optical Properties of OMBD Grown PTCDA and Alq3 Films*, PhD thesis, University of Cincinnati, Cincinnati, 2012.

[108] M. Braun, J. Gmeiner, M. Tzolov, M. Coelle, F. D. Meyer, W. Milius, H. Hillebrecht, O. Wendland, J. U. Von Schütz, and W. Brütting, J. Chem. Phys. **114**, 9625 (2001).

[109] M. Rajeswaran and T. N. Blanton, J. Chem. Crystallogr. **35**, 71 (2005).

[110] G. Y. Zhong, X. M. Ding, J. Zhou, N. Jiang, W. Huang, and X. Y. Hou, Chem. Phys. Lett. **420**, 347 (2006).

[111] D. Z. Garbuzov, S. R. Forrest, A.G. Tsekoun, P. E. Burrows, V. Bulović, and M. E. Thompson, J. Appl. Phys. **80**, 4644 (1996).

[112] C. Himcinschi, N. Meyer, S. Hartmann, M. Gersdorff, M. Friedrich, H. -H. Johannes, W. Kowalsky, M. Schwambera, G. Strauch, M. Heuken, and D. R. T. Zahn, Appl. Phys. A **80**, 551 (2005).

[113] Y. Kawamura, H. Sasabe, and C. Adachi, Japanese J. Appl. Physics, Part 1 Regul. Pap. Short Notes Rev. Pap. **43**, 7729 (2004).

[114] H. Mattoussi, H. Murata, C. D. Merritt, Y. Iizumi, J. Kido, and Z. H. Kafafi, J. Appl. Phys. **86**, 2642 (1999).

[115] A. B. Djurišić, T. W. Lau, L. S. M. Lam, and W. K. Chan, Appl. Phys. A **78**, 375 (2002).

[116] H. Figi, M. Jazbinsek, C. Hunziker, M. Koechlin, and P. Gunter, Opt. Express **16**, 11310 (2008).

[117] C. J. Brabec, Sol. Energy Mater. Sol. Cells **83**, 273 (2004).

[118] H. An, B. Chen, J. Hou, J. Shen, and S. Liu, J. Phys. D. Appl. Phys. **31**, 1144 (1998).

[119] J. Huang, Z. Xie, K. Yang, H. Jiang, and S. Liu, J. Phys. D. Appl. Phys. **32**, 2841 (1999).

[120] D. M. Shyroki and A. V. Lavrinenko, J. Opt. A Pure Appl. Opt. **5**, 192 (2003).

[121] S. Heutz and T. S. Jones, J. Appl. Phys. **92**, 3039 (2002).

[122] S. Tokito, Appl. Phys. Lett. **64**, 1353 (1999).

[123] M. I. Alonso, M. Garriga, N. Karl, J. O. Ossó, and F. Schreiber, Org. Electron. **3**, 23 (2002).

[124] A. B. Djurisic, T. Fritz, and K. Leo, Opt. Commun. **183**, 123 (2000).

[125] S. Hermann, O. D. Gordan, M. Friedrich, and D. R. T. Zahn, Phys. Status Solidi C Conf. **2**, 4037 (2005).

[126] V. R. Gangilenka, *Optical Properties of Organic Thin Films and Waveguides Fabricated by OMBD: Importance of Intermolecular Interactions*, PhD thesis, University of Cincinnati, Cincinnati, (2008).

[127] S. R. Forrest, M. L. Kaplan, and P. H. Schmidt, Annu. Rev. Matterials 189 (1987).

[128] J. Rams, A. Tejeda, and J. M. Cabrera, J. Appl. Phys. **82**, 994 (1997).

[129] P. K. Tien, Appl. Opt. **10**, 2395 (1971).

[130] M. Born and E. Wolf, *Principles of Optics*, 3 rd ed (Pergamon Press, 1970).

[131] V. Ramaswamy, Appl. Opt. **13**, 1363 (1974).

[132] M. Yan, L. Thylen, and M. Qiu, Opt. Express **19**, 3818 (2011).

[133] N. Wickremasinghe, X. Wang, M. Kaveh, A. Dongol, and H. P. Wagner, *Intensity and Temperature Dependent Bimolecular Quenching of Light Emission in Alq3 Films* (to be published).

[134] S. A. Maier, P. G. Kik, H. A. Atwater, S. Meltzer, E. Harel, B. E. Koel, and A. A. G. Requicha, Nat. Mater. **2**, 229 (2003).

[135] W. Cai, D. Genov, and V. Shalaev, Phys. Rev. B **72**, 193101 (2005).

[136] E. N. Economou, Phys. Rev. **182**, 539 (1969).

[137] P. Berini, Phys. Rev. B **61**, 10484 (2000).

[138] P. Berini, Phys. Rev. B **63**, 125417 (2001).

[139] J. Guo and R. Adato, Opt. Express **14**, 12409 (2006).

[140] J. Guo and R. Adato, Opt. Express **16**, 1232 (2008).

[141] Y. Bian, Z. Zheng, X. Zhao, J. Zhu, and T. Zhou, Opt. Express **17**, 21320 (2009).

[142] Y. Bian and Q. Gong, Appl. Phys. Lett. **104**, 251115 (2014).

[143] Y. Bian and Q. Gong, J. Opt. **16**, 015001 (2014).

[144] H. P. Wagner, V. Gangilenka, A. DeSilva, H. Schmitzer, R. Scholz, and T. Kampen, Phys. Rev. B **73**, 125323 (2006).

[145] M. Kaveh, O. Dyck, G. Duscher, Q. Gao, C. Jagadish, and H. P. Wagner, Mater. Res. Express **2**, 045001 (2015).

[146] W. L. Bond, J. Appl. Phys. **36**, 1674 (1965).

[147] K. -H. Schlereth and M. Tacke, IEEE J. Quantum Electron. **26**, 627 (1990).

[148] S. A. Maier, *Plamonics-Fundamentals and Applications* (Springer, 2007).

[149] R. Bock, Phys. Rev. **68**, 210 (1945).

[150] E. D. Palik, *Handbook of Optical Constants of Solids*, 3rd ed. (Elsevier Science & Tech, 1985).

[151] R. A. Ganeev, I. A. Kulagin, A. I. Ryasnyansky, R. I. Tugushev, and T. Usmanov, Opt. Commun. **229**, 403 (2004).

[152] H. P. Li, C. H. Kam, Y. L. Lam, and W. Ji, Opt. Mater. **15**, 237 (2001).

[153] G. Battaglin, P. Calvelli, E. Cattaruzza, F. Gonella, R. Polloni, G. Mattei, and P. Mazzoldi, Appl. Phys. Lett. **78**, 3953 (2001).

[154] H. P. Li, C. H. Kam, Y. L. Lam, Y. X. Jie, W. Ji, A. T. S. Wee, and C. H. A. Huan, Appl. Phys. B **72**, 611 (2001).

[155] M. Samoc and P. N. Prasad, J. Chem. Phys. **91**, 6643 (1989).

[156] M. Stella, C. Voz, J. Puigdollers, F. Rojas, M. Fonrodona, J. Escarré, J. M. Asensi, J. Bertomeu, and J. Andreu, J. Non. Cryst. Solids **352**, 1663 (2006).

[157] A. Kobitski, R. Scholz, I. Vragović, H. Wagner, and D. Zahn, Phys. Rev. B **66**, 153204 (2002).

[158] A. Kobitski, R. Scholz, D. Zahn, and H. Wagner, Phys. Rev. B **68**, 155201 (2003).

[159] M. Ziari, S. Kalluri, and W. H. Steier, Proc. SPIE **2285**, 84 (1994).

[160] V. Gangilenka, A. DeSilva, H. P. Wagner, R. Tallman, B. Weinstein, and R. Scholz, Phys. Rev. B **77**, 115206 (2008).

[161] I. Vragović and R. Scholz, Phys. Rev. B **68**, 155202 (2003).

[162] P. N. Butcher and D.Cotter, *The Element of Nonlinear Optics* (Cambridge University Press, 1990).

[163] Y. A. Bykovskii, A. V. Makovkin and V. L. Smirnov., J. Quantum Electron **4**, 1050 (1975).

[164] N. Kim, B. Domercq, S. Yoo, A. Christensen, B. Kippelen, and S. Graham, Appl. Phys. Lett. **87**, 1 (2005).

[165] N. Wickremasinghe, X. Wang, H. Schmitzer, and H. P. Wagner, Opt. Express **22**, 23955 (2014).

[166] A. B. Djurisic, C. Y. Kwong, W. L. Guo, T. W. Laua, E. H. Li, Z. T. Liu, H. S. Kwok, L. S. M. Lam, W. K. Chan, Thin Solid Films **416**, 233 (2002).

[167] F. Zhang, Z. Xu, D. Zhao, S. Zhao, W. Jiang, G. Yuan, D. Song, Y. Wang, and X. Xu, J. Phys. D. Appl. Phys. **40**, 4485 (2007).

[168] S.-W. Feng, Opt. Mater. Express **4**, 798 (2014).

[169] E.-M. Han, L.-M. Do, N. Yamamoto, and M. Fujihira, Thin Solid Films **273**, 202 (1996).

[170] N. Wickremasinghe, J. Thompson, X. Wang, H. Schmitzer, and H. P. Wagner, J. Appl. Phys. **117**, 213102 (2015).

[171] M. A. Noginov, V. A. Podolskiy, G. Zhu, M. Mayy, M. Bahoura, J. A. Adegoke, B. A. Ritzo, and K. Reynolds, Opt. Express **16**, 1385 (2008).

[172] Y. Wakabayashi, J. Yamauchi, and H. Nakano, Adv. Optoelectron. **2010**, 1 (2011).